FACULTY
OF MATHEMATICS
AND PHYSICS
Charles University

DOCTORAL THESIS

Mgr. Martin Golan

Influence of freezing and thawing process on cryopreserved cells nuclei and surfaces. Functions and physico-chemical properties of cryoprotectants.

Institute of Physics of the Czech Academy of Sciences

Department of Analysis of Functional Materials

Supervisor: Assoc. prof. Ing. Irena Kratochvílová, Ph.D.

Study programme: Physics

Specialization: Biophysics, Chemical and Macromolecular Physics

Prague 2018

I declare that I carried out this doctoral thesis independently, and only with the cited sources, literature and other professional sources.

I understand that my work relates to the rights and obligations under the Act No. 121/2000 Coll., the Copyright Act, as amended, in particular the fact that the Charles University has the right to conclude a license agreement on the use of this work as a school work pursuant to Section 60 paragraph 1 of the Copyright Act.

In Prague, May 18, 2018

Given the broad scope of this work, its completion wouldn't be possible without the generous help, cooperation and support of a number of people. First and foremost, I would like to thank my thesis advisor, Assoc. prof. Ing. Irena Kratochvílová, Ph.D., whose guidance and keen involvement in the research of cryopreservation were essential for achieving the results presented here.

Furthermore, I would like to express deep gratitude to Dr. Martin Falk and his team (Dr. Iva Falková et al.) at the Institute of Biophysics CAS, whose expertise, cooperation and facilities were crucial for the part of this work that deals with post-thaw damage of cell nuclei. I would also like to thank Professor Bořivoj Klejdus for helping our team understand the cell-permeative properties of trehalose.

Likewise, I would like to thank Dr. Jan Přibyl and his colleagues (Dr. Vladimír Rotrekl, Mgr. Šárka Jelínková et al.) at CEITEC for their help and fruitful collaboration on the research of post-thaw cell properties and regeneration.

I also gratefully acknowledge the work of Dr. David Řeha from The Center for Nanobiology and Structural Biology, and Dr. Jakub Šebera (Institute of Physics CAS), whose theoretical modelling of cryoprotectant molecules helped elucidate some of the physical properties of cryoprotectant solutions, and Dr. Luděk Šefc from the First Faculty of Medicine, Charles University, for his advice and help.

My sincere thanks also go to Dr. Daniel Šimek (Institute of Physics CAS) who dedicated his time, expertise and XRD instrumentation to help us study the crystalline properties of frozen cryoprotectants.

Our work on the antifreeze protein ApAFP752 wouldn't be possible without As. Prof. Krisztina Varga and her team, who provided us with its samples.

I would also like to express my thanks to all other colleagues who provided their help and advice – among them namely Dr. Jan Richter, Ing. Silvia Sedláková and Dr. Karel Pomeisl.

Importantly, this work was financially supported by the projects of the Ministry of Education, Youth and Sports: CZ.02.1.01/0.0/0.0/16_013/0001406, LM2015088.

Finally, my deep thanks go to my family and loved ones for their patience and unwavering support throughout my doctorate.

Název: Účinky procesu kryoprezervace na jádro a povrch buňky. Funkce a fyzikálně-chemické vlastnosti kryoprotektantů.

Autor: Mgr. Martin Golan

Oddělení/Ústav: Oddělení analýzy funkčních materiálů, Fyzikální ústav Akademie věd České Republiky

Vedoucí doktorské práce: doc. Ing. Irena Kratochvílová, Ph.D.

Abstrakt: Kryoprezervace buněk je komplexní proces nalézající uplatnění v základním biologickém výzkumu, lékařství i zemědělství. Tato práce prohlubuje současné chápání kryoprezervace buněk a jejích důsledků, a to na biologické i fyzikální úrovni. Výsledky obsahují charakteristiku chování vybraných kryoprotektantů (především DMSO, trehalóza, antifreeze protein ApAFP752) v kapalné fázi, v pevné fázi i během tuhnutí. Pozornost je rovněž věnována charakteru a míře poškození rozmrazených buněk, u nichž byla sledována jejich viabilita a vývoj stavu jejich povrchu a jádra (integrita jaderné membrány, úroveň kondenzace chromatinu, přitomnost dvojných zlomů DNA). Důležitým výsledkem je, že S-fázní buňky (NHDF a MCF7 linie) během kryoprezervace utrpí rozsáhlý kolaps replikačních vidliček, což představuje závažné poškození. Je tedy vhodnější mrazit buňky v jiných fázích buněčného cyklu. Ke sledování stavu rozmrazených buněk byla použita především mikroskopie atomárních sil (AFM), konfokální fluorescenční mikroskopie a průtoková cytometrie. Získané poznatky mohou být použity k optimalizaci používaných kryoprezervačních protokolů a k lepšímu hodnocení účinnosti a šetrnosti nově vyvinutých kryoprotektantů.

Klíčová slova: kryoprezervace, kryoprotektant, mechanické vlastnosti buněk, dvojné zlomy DNA, kondenzace chromatinu

Title: Influence of freezing and thawing process on cryopreserved cells nuclei and surfaces. Functions and physico-chemical properties of cryoprotectants.

Author: Mgr. Martin Golan

Department/Institute: Department of Analysis of Functional Materials, Institute of Physics of the Czech Academy of Sciences

Supervisor of the doctoral thesis: As. Prof. Ing. Irena Kratochvílová, Ph.D.

Abstract: Cryopreservation of cells is a complex process with many useful applications in basic biological research, medicine and agriculture. In this work we deepened the current understanding of the cryopreservation process both at physical and biological level. Results include characteristics of selected cryoprotectants (primarily DMSO, trehalose, antifreeze protein ApAFP752) in liquid phase, during phase transition and in solid phase, as well as their impact on cryopreserved cells states. Specifically, the level of cell viability, state of cell membrane and condition of cell nucleus (nuclear membrane, chromatin condensation, DNA strand breaks) are monitored over several time points after thawing. It is shown that S-phase cells (NHDF and MCF7 lines) suffer massive collapse of replication forks during cryopreservation which makes them much less suitable for cryopreservation than cells in other phases of the cell cycle. Several methods (most importantly Atomic Force Microscopy, Confocal Fluorescence Microscopy and Flow Cytometry) were used to examine the post-thaw state of cryopreserved cells. The acquired insights into cryodamage of cells can lead to optimization of current cryopreservation protocols and to more thorough evaluation of efficacy of future novel cryoprotectants.

Keywords: cryopreservation, cryoprotectant, cell mechanical properties, DSB breaks of DNA, chromatin condensation

Contents

1 Introduction

Effective cryopreservation is an important process in basic biological research, medicine, pharmaceutical industry, biotechnology, and agriculture. It enables an almost infinite storage of cell cultures, which is often crucial for performing experiments on cells. In medicine, cryopreservation is indispensable for areas such as autologous stem cell transplantation and assisted reproduction.

However, although cryopreservation of cells is in widespread use, it affects the cells in many negative ways (e.g. structural damage, changed gene expression (Kopeika et al. 2015; Monzo et al. 2012)), therefore its further optimization is desirable. Such negative effects are usually overlooked when freezing common somatic cell cultures, but in the case of gamete and embryo cryopreservation, any interference with the cell state should be avoided. The increasing use of assisted reproduction makes the optimization of gamete and embryo cryopreservation rather pressing, especially because there is evidence that increased incidence of defects in live births resulting from *in vitro* fertilization has been observed (Kelley-Quon et al. 2013; Olson et al. 2005).

A multitude of factors influence the success of cell cryopreservation. The most important parameters that can be tuned in a cryopreservation protocol is the chemical composition of the freezing medium (i.e. choice of cryoprotectants and their concentrations (Elliott et al. 2017)), and the speed of cooling and warming. Inconveniently, the optimal setting of these parameters strongly depends on the cell line since different cell types have a large variability in membrane permeability, internal structure and overall cell size. Oocytes happen to be among the cell types most difficult to freeze successfully due to their large volume, thick membrane and delicate structure (Coticchio et al. 2007).

Also, the ability of cells to survive cryopreservation is affected by their specific condition at the moment of freezing. That is affected both by physiological (e.g. cell cycle related) and pathological (e.g. cancerous) processes.

From the parameters that play a role in the process of cell cryopreservation, we focus on the effects of cryoprotectants. Throughout this work, slow freezing (cooling rate 1°C/min) is used (as opposed to vitrification) since it remains the most commonly used approach, especially for samples of nonmicroscopic volumes. The cryoprotectants probed here differed crucially in their ability to penetrate the cytoplasmatic and nuclear membrane, and in the way they modify the freezing process of water.

Based on the extent to which the cryoprotectant is able to enter into the cell, three categories can be distinguished:

(1) cryoprotectants penetrating both cell and nuclear membrane (e.g. dimethyl sulfoxide - DMSO, glycerol)

(2) cryoprotectants penetrating cell membrane but not nuclear membrane (e.g. some saccharides, aminoacids)

(3) cryoprotectants not penetrating even the cell membrane (proteins, polysaccharides, PEG-1500)

Regarding the way cryoprotectants affect the freezing of water, two groups can be distinguished.

The first group comprises cryoprotectants which favorably affect the thermodynamic and chemical properties (phase transition temperature, hydrogen bonding) of the cryoprotective solution (e.g. glycerol, glucose, trehalose).

The second group comprises substances that affect the kinetics of the ice crystals formation, growth and recrystallization (e.g. antifreeze proteins, small or polymeric ice recrystallization inhibitors). A characteristic feature of these materials is that unlike the first group of cryoprotectants, they cause thermal hysteresis – they decrease the freezing point of the system while not affecting or even elevating its melting point.

In this work, we combined two major objectives: to find out how selected cryoprotectant aqueous solutions modify freezing process of water (physical point

of view) and how the cryopreservation in these solutions affects the post-thaw state of cryopreserved cells. We correlated the physico-chemical properties of the selected cryoprotectants, their influence on the constitution of ice and their effects on frozen/thawed cell viability and cell surface stiffness and nucleus integrity after being frozen/thawed. Thus, we linked the physical and biological aspects of cryopreservation.

The cryoprotectants studied in this work were chosen to cover all cryoprotectant classes with regard to their ability to penetrate cells. DMSO penetrates easily both cytoplasmatic and nuclear membrane, trehalose permeates the cytoplasmatic membrane after prolonged incubation, antifreeze protein ApAFP752 and polyethylene glycol PEG-1500 remain in the extracellular space. The protein ApAFP752 also differs from the other materials in that it affects the freezing kinetics and causes thermal hysteresis.

First, we described the freezing process and properties of aqueous solutions of studied cryoprotectants using computer simulations (molecular dynamics and ab-initio modelling), Raman spectroscopy, Differential Scanning Calorimetry and X-Ray Diffraction. These results were correlated with the viability of cells frozen/thawed in the respective cryoprotective solutions, with the impact of cryopreservation on the stiffness of thawed cells (measured by AFM) and with the post-thaw state of cell nuclei studied by fluorescence microscopy (higher-order chromatin structure, formation of DNA double-strand breaks, nuclear envelope integrity) (Falk et al. 2018; Golan et al. 2018a; Golan et al. 2018b; Kratochvilova et al. 2017).

The presented work takes a comprehensive approach to cryopreservation comprising both physico-chemical and biological point of view, allowing us to study processes ranging from the extracellular space through cell surface down to cell nucleus and its DNA content (**Scheme 1.1**).

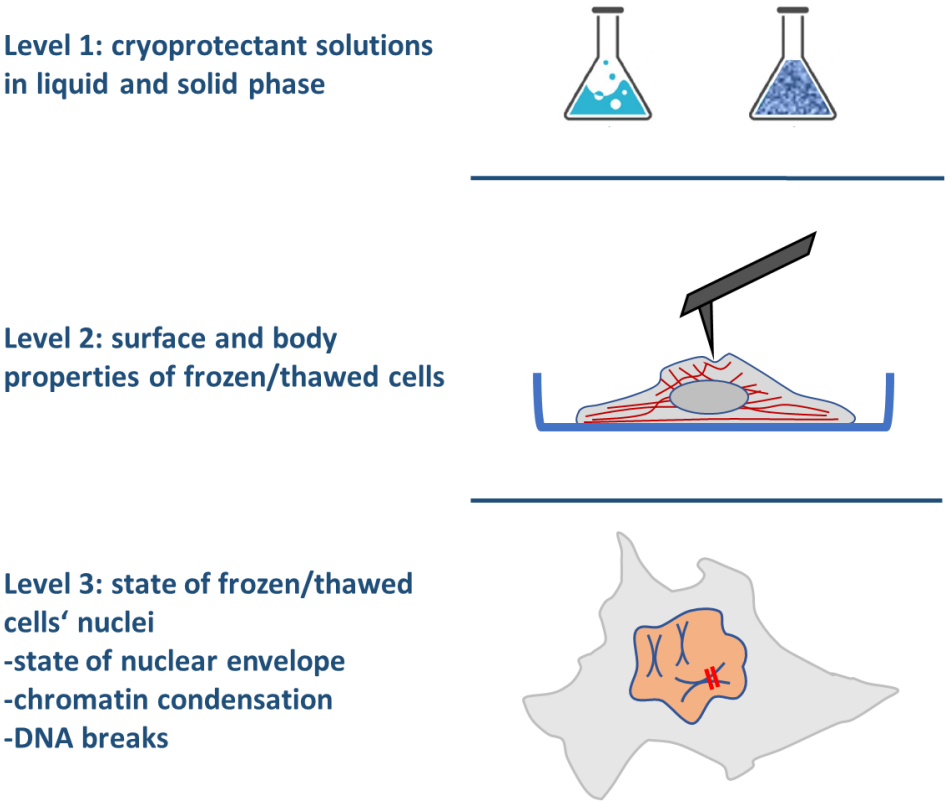

Scheme 1.1: Aspects of cryopreservation covered in this work.

The scope of the employed methods is broad, and their use is often novel (e.g. XRD used to describe the solutions‘ crystallinity and recrystallization, AFM used to track the post-thaw development of cell stiffness, confocal microscopy of thawed cells‘ nuclei). Correspondingly, our work is the first to report several phenomena and relationships related to cell cryopreservation (e.g. crystallite size in frozen cryoprotective solutions, differences in post-thaw cell stiffness depending on used cryoprotectant, relationship between post-thaw cell viability and chromatin condensation, sensitivity of S-phase cells towards cryopreservation due to novel mechanism of DNA damage).

The set of methods employed here can be used for complex evaluation of newly developed cryoprotectants, and provide feedback for refinement of their design (**Scheme 1.2**).

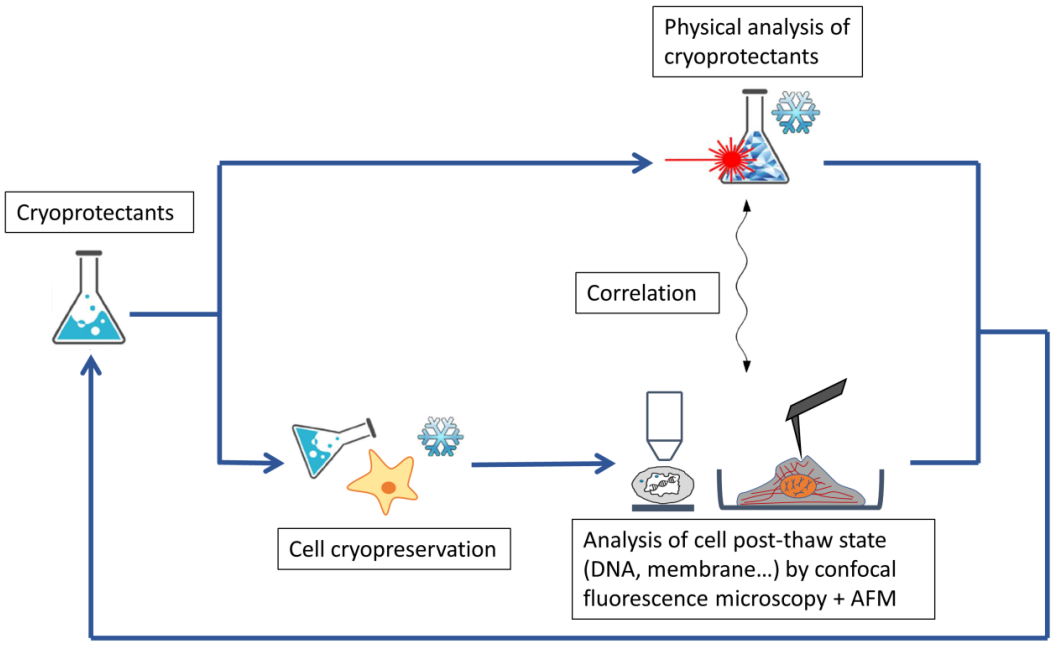

Scheme 1.2 Scheme of the experimental workflow in this work. We combined two major objectives: to find out how selected cryoprotectant aqueous solutions modify freezing process of water (physical point of view) and how the cryopreservation in these solutions affects the post-thaw state of cryopreserved cells. We correlated the physico-chemical properties of the selected cryoprotectants, their influence on the constitution of ice and their effects on frozen/thawed cell viability and cell surface stiffness and nucleus integrity after being frozen/thawed. Thus, we linked the physical and biological aspects of cryopreservation.

The driving motivation of our work was an effort to decrease the risk of cell damage associated with cryopreservation, which is especially important for regenerative medicine and assisted reproduction. We anticipate that better understanding of cryopreservation on all levels will help optimize current cryopreservation protocols as well as design novel cryoprotectants. For reproductive medicine, the most important goal is to cryopreserve gametes or embryos so that their DNA remains completely intact.

1.1 A brief history of cryobiology

The founding of cryobiology as a discipline is generally atributed to the Swiss scientist B. J. Luyet who summed up existing knowledge on the topic in his work Life and Death at Low Temperatures (Luyet and Gehenio 1940). The role of parameters like cooling rate, temperature and length of storage etc. became the focal point of a more systematic research and more effort was invested in the research of various additives – named cryoprotectants (Easley 1942). In the center of interest lay various saccharides and egg yolk (Paul H. Phillips 1940). A successful cryopreservation of red blood cells was announced a mere year later (Smith 1950). Cryopreservation of sperms was improved so much that in 1953, the first fertilization of a women with cryopreserved sperms took place (Bunge and Sherman 1953). Since the research up to that point had been largely empirical, based on intuition or just trial and error, there was an effort to put the accumulated results within some theoretical framework. At the beginning of the 1960s, Peter Mazur formulated the first mathematical model of the phenomena unfolding in cells during freezing (Mazur 1963). This period also saw the discovery of dimethyl sulfoxide as a cryoprotectant (Lovelock and Bishop 1959), which to this day remains the most universal and widely used cryoprotective agent. By 1964, successful cryopreservation of a large number of animal cell lines was announced (Coriell et al. 1964). Cryoprotective properties of the first polymer, polyvinylpyrrolidon, were published in 1966 (Doebbler et al. 1966). Progress was also being made with the optimalization of the cooling rate. B. J. Luyet proposed already in 1937 that cryodamage (i.e. damage resulting from freezing) could be prevented by flash freezing (Luyet 1937). The idea was that by cooling quickly, the formation of ice crystals could be avoided. Instead, amorphous, glass-like solid would form where the arrangement of water molecules would remain practically the same as in the liquid phase.

Vitrification then improved due to its potential as a method for preservation of tissues and organs as slow freezing was failing to make a significant progress in that area (Armitage and Rich 1990). In 1969, a new kind of material relevant for cryopreservation was discovered. DeVries et al reported a glycoprotein with

thermal hysteresis, isolated from the serum of arctic fish (Devries and Wohlschlag 1969).

In 1972, Peter Mazur et al formulated his „two-factor hypothesis“ about the origins of cryodamage. The two factors proposed to lead to this behaviour is osmotic stress (when cooling is too slow) and intracellular ice crystallization (when cooling is too fast).

In the same period came a successful birth of a healthy mouse after its mother had been fertilized by a cryopreserved embryo (Whittingham et al. 1972). Soon after that, the same was achieved with a cryopreserved mouse oocyte (Parkening et al. 1976). In the 1980s, successful pregnancy was also achieved in humans - first using slow freezing (Chen 1986) and soon afterwards also using vitrification (Trounson et al. 1987). A groundbreaking success was achieved by Greg Fahy et al. who cryopreserved a rabbit kidney well enough for it to be reimplanted to a living rabbit. It then managed to support the rabbit's life functions even though its other kidney was surgically removed (Fahy et al. 2009).

1.2 The process of freezing and thawing

1.2.1 Slow freezing

When the ambient temperature starts to decrease below 37°C, the kinetics of chemical reactions in cell slows down. The rate at which chemical reactions slow down generally vary; if these reactions are interdependent, a metabolic imbalance may ensue, leading to cell damage (Baust and Baust 2007). Furthermore, low temperature may lead to protein denaturation (Privalov 1990) and to structural changes or even phase transitions in cell membranes (Sieme et al. 2015). However, if the temperature approaches 0°C, such damage proceeds slowly and the cells are able to survive many hours under such conditions. Thanks to that, it is possible to routinely store cells on ice during lab experiments.

That situation changes if the temperature keeps dropping below 0°C, e.g. at a rate around 1°C/min typical for slow freezing.

Ice crystallization doesn't start immediately since the solvents present in cultivation media reduce the freezing temperature of these media, and more importantly, aqueous solutions in general have a propensity for supercooling. However, by ca -20°C, ice nucleation will typically already have started (Morris and Acton 2013).

The occurring ice nucleation is heterogenous, meaning that it starts on the surface of various impurities (Karlsson et al. 1993a). Crystallization is typically started in the extracellular space since it contains more potential crystallization nuclei, and also because the concentration of macromolecules and solvents there is lower than inside the cells (Rasmussen et al. 1975). Freezing of part of the extracellular solution effectively leads to an increase in concentration of solvents in the part that remains liquid. That brings about an osmotic imbalance, that results in a net flow of water from the inside of cells out. Moreover, the water in the supercooled protoplasm has higher chemical potential than the ice outside the cell. This causes the cells to dehydrate and the concentration of ions and other solvents to increases beyond physiological concentrations, which is a source of chemical stress (e.g. changing the solvation layer around biomacromolecules may lead to their denaturation (Gao and Critser 2000).

If the cooling proceeds very slowly, most extracellular water undergoes crystallization. Between crystals remain constricted pockets of concentrated solvents and strongly dehydrated cells, whose membranes dehydrate and undergo a phase transition from liquid crystalline to gel phase (typically at slightly subzero temperatures, e.g. -3 to -10°C (Wolkers et al. 2007)). Faced with strong hyperosmotic stress, the weakened membrane starts leaking ions to the intracellular space (which, rather ironically, later on during thawing leads to hypotonic stress and often also to cell bursting). The remaining liquid eventually creates a eutectic mixture of ice and various salt hydrates, or vitrifies into an amorphous glass.

In all, although cells may avoid the formation of fatal intracellular ice in this scenario, the amount of chemical and mechanical stress is such that the probability of survival in good condition is very low.

The level of chemical stress decreases when the cooling rate is higher. However, when cells are cooled too fast, their intracellular water doesn't have enough time to drain from them. Thus, the cells become exposed to very low temperatures in a state in which they still have high content of water. Thus, they are prone to intracellular ice formation which physically damages the fine networks of intracellular structures nad may even lead to the puncturing of cytoplasmatic membrane. In other words, intracellular ice formation represents a source of serious damage and is often followed by cell death (Korber et al. 1991; Mazur 1961a; Mazur 1961b; Wesley-Smith et al. 2015).

Between these two scenarios (too slow and too fast cooling rate), there exists an optimal cooling rate that minimizes the combined detrimental effect of both damage mechanisms A two factor hypothesis of freezing injury;. Cooling at this rate in itself, however, isn't sufficient for effective survival of freezing. For that, the freezing medium must be supplemented with suitable chemical substances termed cryoprotectants. Furthermore, due to structural and functional differences (e.g. membrane permeability) among various cell types, the value of optimal cooling rate falls on a broad spectrum from around 1°C/min (murine haematopoietic stem cells) to 1000°C/min (human erythrocytes) (Fuller et al. 2004).

The process of cell dehydration during freezing is mathematically described in (Mazur 1963). The Mazur equations formulated therein were later refined and extended (Fahy 1981; Karlsson et al. 1993b; Liu et al. 2000; Toner et al. 1990), but continue to form a basis of our understanding of cell cooling to this day. They describe the exchange of water between cytoplasm and extracellular space through cytoplasmatic membrane. The extracellular space contains ice, and also a concentrated liquid phase which is however in equilibrium with the ice. The cytoplasm is considered liquid and supercooled.

1.2.2 Vitrification

Very important phenomenon of cryopreservation process is formation of glassy state in the frozen solutions. Formation of the solution glassy state is in the case of cryopreservation called vitrification (quick lowering of temperature). At the molecular level, this process is associated with loss of rotational and translational degrees of freedom, only the vibration of bonds within a fixed molecular structure is preserved. The process of the vitrification prevents intracellular space from cells damaging crystals of ice.

For pure water, the glass transition temperature is -137°C (Elsaesser et al. 2010; Johari et al. 1987). The presence of cryoprotectants as well as intracellular macromolecules shift this value upwards.

Vitrification may seem like the perfect solution to the problem of cryopreservation: water molecules remain fixed in their place, with no chemical or mechanical stress ocurring. The crucial obstacle is nevertheless the realization of the vitrification process.

The cooling rate necessary to vitrify water is over 10^7 K/s (Franks 1982), which is difficult to reach especially for realistic (nonmicroscopic) sample sizes due to finite speed and inhomogeneity of heat conduction.

Despite that, cryopreservation occupies an important place in the field of cryopreservation and its importance and use has been expanding. To achieve it, however, it is also necessary to use various cryoprotectants that increase the solution viscosity, glass transition temperatures etc., and conversely reduce the necessary rate of cooling. Ironically, the concentrations needed are often higher than those needed for slow freezing.

At cryogenic temperatures (where the temperature of liquid nitrogen, -196°C, certainly belongs), biological processes come to a halt and samples can be stored without degradation almost for ever. The only limitation is cosmic radiation but its impact only becomes relevant after thousands of years of storage (Woods et al. 2016).

1.2.3 Thawing

Phenomena relevant for cell survival also occur during rewarming of the cryopreserved sample back to physiological temperature. An important one is so called ice recrystallization: due to thermodynamic favorability, larger ice crystalls have a tendency to grow at the expense of smaller ones. That causes significant mechanical injury even to cells that survived the cooling stage intact. Likewise, vitrified samples have a tendency to devitrify (i.e. undergo secondary crystallization) during rewarming as the energetic barrier separating the crystalline and amorphous state lowers.

The optimal rate of thawing depends on the previous rate of cooling. If the cells were cooled quickly (i.e. contain glass or small crystals), fast thawing yields much better results than slow thawing since the time for ice recrystallization is limited. If the cooling is slow (hence the system remained close to thermodynamic equilibrium), the effects of the rate of thawing are more complex. All possible scenarios (fast thawing superior/equal/inferior to slow thawing) have been documented, depending on the specific cell lines and used cryoprotectants etc (Akhtar et al. 1979; Kasai et al. 1982; Miyamoto and Ishibashi 1983; Rall and Polge 1984; Taylor et al. 1987; Van den Abbeel et al. 1994; Wells et al. 1979). Secondly, thawing can expose the cells to oxidative stress originating e.g. from damaged reaction centers of mitochondrial respiratory chains, or from the uneven reactivation of related coupled chemical reactions (Fuller et al. 1988).

1.3 Cryoprotectants

1.3.1 Small permeating cryoprotectants

An important group of cryoprotectants are cell-permeating substances that decrease the freezing point of the cryopreservation medium. Seemingly, this merely postpones the problem of crystallization, dehydration and chemical stress to a later stage of the cooling. In fact, such postponement is beneficial in that the chemical stress (resulting from extracellular and/or intracellular freezing) of given magnitude occurs at lower temperature. Thus, the kinetics of all chemical reactions is slowed down and their harmful effect is decreased.

In this group belongs DMSO (**Fig. 1.3.1.1**). DMSO is a polar aprotic solvent that is highly hygroscopic. It is capable of forming strong hydrogen bonds with water, but it acts only as an electron donor (its hydrogens are not sufficiently acidic – hence its aproticity). A second important property of DMSO (resulting from its ability to permeate membranes) is a tendency to substitute part of the intracellular water leaving the cell during freezing. That decreases negative effects of cell dehydration and limits the mechanical stress related to the change in cell volume and shape (Fuller et al. 2004).

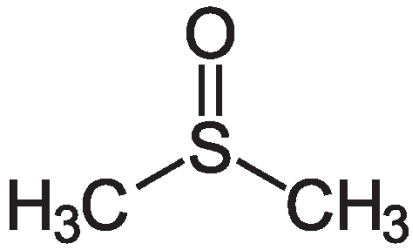

Fig. 1.3.1.1. Structure of dimethyl sulfoxide (DMSO)

DMSO molecules mix well and homogeneously with their water counterparts. On a molecular level, DMSO can form a range of different structures with water molecules depending on their relative concentration (Oh et al. 2017). At low concentrations, it seems to preferably form clusters of 1 DMSO molecule bound to 2 waters (with 1 water possiby participating in 2 such clusters). These clusters radically distort the native hydrogen bond network, and their low mutual interaction may explain the deep depression of the freezing point of the eutectic mixture (Wallace et al. 2015). Furthermore, at concentrations around the eutectic point, the system undergoes a large increase in viscosity upon cooling and eventually vitrifies. This makes such mixtures of DMSO and water useful for cryopreservation by vitrification since the resulting vitrified, amorphous solid phase causes much less mechanical stress to the cells than crystalline ice (Jena and Aksan 2017). Nevertheless, the necessary concentration of DMSO is high and causes a chemical stress of its own.

For cryopreservation by slow freezing, lower concentrations of DMSO (typically around 10% w/w) are used. That is not sufficient to bring about the vitrification of the sample as a whole, but it significantly reduces the chemical stress. Furthermore, as the aqueous part of the sample gradually freezes, the concentration of DMSO in the remaining liquid fraction increases. The ability of DMSO-water mixtures to vitrify may thus contribute to cell survival even in the case of slow freezing of cryoprotective solutions with low DMSO content In the extracellular space, DMSO interacts with cell membranes in a manner dependent on its concentration (de Menorval et al. 2012; Gurtovenko and Anwar 2007). At low concentrations, it leads to membrane thinning, undulation and increased fluidity.

Larger concentrations enhance membrane permeability for water as well as ions, even induce transient pores. Increasing the concentration even further gradually leads to disintegration/dissolution of the membrane. In the context of cryoprotection, it is likely that increased membrane fluidity/elasticity is beneficial when conforming to mechanical stresses exerted on cells during freezing. Increased permeability helps ameliorate osmotic stresses, that present another important source of cryodamage.

Apart from being used as a cryoprotectant, DMSO can also facilitate membrane fusion and drug administration through skin. A mechanism of this interaction between DMSO and lipid membranes is suggested in (Cheng et al. 2015). Leaving aside the exact effects of DMSO on cells on the molecular level, there is no ambiguity about the fact that especially at higher concentrations and at longer incubation times, DMSO has negative effects on cells (Galvao et al. 2014; Yi et al. 2017; Yuan et al. 2014). For instance, it has been shown that it impedes cell proliferation (Bentrivedi et al. 1990).

DMSO permeates membranes and thus affects osmotic processes during freezing. With no DMSO present, the concentration of ions in the yet unfrozen fraction of extracellular space increases after the onset of extracellular freezing. As a result, intracellular water starts to flow out of cells in order to compensate for the emerging osmotic imbalance. That in turn increases intracellular osmolality beyond

physiological concentration and subjects cytoplasmatic membrane to mechanical strain. DMSO decreases the freezing temperature of the medium, which means that any osmotic imbalance takes effect at lower temperatures where kinetics of harmful chemical reactions are slower.

1.3.2 Saccharides

The function of a number of saccharides like glucose, saccharose and trehalose is based on the same principles, but the natural ability of these molecules to penetrate the cell is varied (Sieme et al. 2015). Saccharides help to stabilize biological molecules. For instance, there is numerous evidence that trehalose can partially substitute the solvation shell of proteins. In the event of phase transition, this shell remains amorphous which thus protects them from dehydration and denaturation (Corradini et al. 2013; Jain and Roy 2009). Trehalose is able to intercalate into the outer phospholipid layer of the cell membrane and stabilize it by hydrogen bonding to the polar parts of its phospholipids (Villarreal et al. 2004). Thanks to this effect, saccharides can have cryoprotective effects even if present only extracellularly.

From the cited cryoprotective saccharides, most attention has centered on trehalose due to it yielding results equal or superior to other cryoprotectants. The reason for this may be its comparatively large stability (Fuller et al. 2004). It is a nonreducing saccharide (unlike e.g. glucose) which doesn't enter Maillard reaction when exposed to proteins. Saccharose is also a nonreducing sugar, but its glycosidic bond is vulnerable to hydrolysis, and its monosacharide products than do react with proteins. Organisms using glucose, sachcarose etc. for cryoprotection probably employ supporting protective mechanisms that counter this instability.

1.3.2.1 Trehalose

Among saccharides, trehalose is one of the most potent cryoprotectants (although it is less effective and universal than DMSO) (Elliott et al. 2017). It is a

disaccharide consisting of two glucose subunits linked by an alpha-1,1-glycosidic bond. The glycosidic bond of trehalose links the anomeric carbons of its glucose subunits, which prevents them from unfolding into linear, open-chain forms with free aldehyde groups. The low energy of this bond makes trehalose very stable (with respect to high temperatures or low pH) and resistant to hydrolysis. As a result, trehalose practically doesn't react with proteins (e.g. through non-enzymatic Maillard-type browning), unlike glucose or sucrose (Fuller et al. 2004; OBrien 1996; Schebor et al. 1999) (although sucrose is a nonreducing disaccharide that in other tests of stability performed similarly well as trehalose.

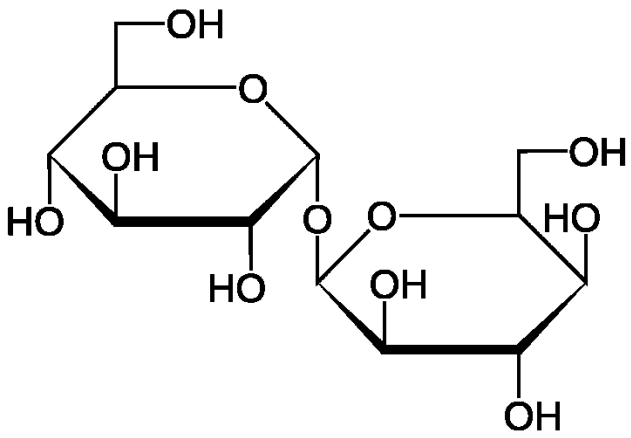

Fig. 1.3.2.1.1. Trehalose is a sugar consisting of two molecules of glucose. Some bacteria, fungi, plants and invertebrate animals synthesize it as a source of energy, and to survive freezing and lack of water.

Like many other saccharides, trehalose has an ability to form a glassy state in bulk and in solution. Compared to other sugars, however, its glass transition temperature is higher, which possibly contributes to its stabilizing properties (Green and Angell 1989; Chen et al. 2000; Jain and Roy 2010).

In aqueous solution, trehalose forms hydrogen bonds with water molecules, but also with other trehalose molecules (molecular dynamics simulations in (Sapir and Harries 2011) and (Kratochvilova et al. 2017) have shown propensity of

trehalose to form clusters). Trehalose helps prevent proteins in aqueous solutions from denaturation (i.e. distortion of their secondary and tertiary structure) caused by a range of environmental stresses (freezing, heating, desiccation…) (Hedoux et al. 2007; Hedoux et al. 2013; Hedoux et al. 2006; Olsson et al. 2016). Generally, trehalose has a strong stabilizing effect on the structure of biomolecules that is superior to most other saccharides. Trehalose molecules form a cage around the protein and inside this cage there are locked water molecules with substantially slowed dynamics. This arrangement prevents crystallization of these waters and therefore dehydration and denaturation of the protein in the center of the cage. Other models of stabilization include direct vitrification of the protein in a glassy trehalose matrix that directly shields the protein from environmental stress, preferential exclusion theory and water replacement theory (Jain and Roy 2009; Jain and Roy 2010; Liu et al. 1997).

Like proteins, trehalose also stabilizes lipid membranes (Crowe et al. 1984). Many more works have been published concerning its positive effects on liposome integrity during lyofilization and freeze-drying, which are processes that bear many similarities to cryopreservation (Ball et al. 2017; Harland et al. 2009; Chen et al. 2001; Ohtake et al. 2006).

Trehalose doesn't readily penetrate membranes of mammalian cells (Abazari et al. 2015). Therefore, it only acts extracellularly in most experiments which also makes it a contributor to osmotic stress (Lin et al. 2009).

There are however ways to load trehalose inside the cell - after longer incubation times, trehalose does in fact enter the intracellular space, but the long loading time (up to 24 hours) is a slight practical disadvantage of this approach.

Other approaches include incubation with a copolymer PP-50 which unfolds at low pH, bursting the encapsulating endosome and releasing all endocytosed trehalose into the cytoplasm (Sharp et al. 2013), or engineering membrane pores so that trehalose can pass through (Eroglu et al. 2000). Genes responsible for trehalose synthesis have also been transfected to human cells, confering resistance to desiccation (Guo et al. 2000). An acetated analogue of trehalose (with retained

cryoprotective ability) has also been engineered, with much increased permeation rates (Abazari et al. 2015).

1.3.3 Polymeric cryoprotectants

Membrane is stabilized and/or mechanically protected also by various nonpermeating cryoprotective polymers (Rajan and Matsumura) such as PEG-1500 (Zemlianskykh and Babijchuk 2017) or polyvinylpyrrolidon (Damjanovic and Thomas 1974).

These extracellular cryoprotectants can also affect the transport of water from the cell during cooling (Takahashi et al. 1988) and may impede the recrystallization of ice during thawing COOH-polylysin (Matsumura et al. 2010), hence possessing Ice Recrystallization Inhibition activity (IRI). A rather extreme but functional approach is even to encapsulate the cells in an alginate hydrogel coating (Pravdyuk et al. 2013).

1.3.4 Ice-structuring proteins and their functional analogs

A completely different mechanism of cryoprotection is the interference of the cryoprotectant molecules with the growth of emerging ice crystals. This is a key property in several (not necessarily disjunctive but rather largely overlapping) groups termed in literature as antifreeze proteins (AFP), ice-structuring proteins (ISP) (Clarke et al. 2002), ice-binding proteins (IBP), thermal hysteresis proteins/factors (THP/F), ice recrystallization inhibitors and more (Yeh and Feeney 1996).

The common structural denominator of these molecules is the existence of a planar „ice-binding“ domain with regularly spaced aminoacid residues. Among the most common aminoacids found in these residues is threonine and alanine (Daley and Sykes 2004; Krishnamoorthy et al. 2014; Wierzbicki et al. 2007).

If the temperature drops below zero, such proteins adsorb via their ice-binding domain to surface of the ice crystal and block its further growth. By

doing that, it stops the phase transition and depresses the temperature at which the solution remains in supercooled state until the level of supercooling is too large and the solution flash-freezes. When rewarmed, it is clear that the melting point won't be affected accordingly. The solution melts close to its original freezing temperature or even above it because the proteins adsorbed to the ice crystal nuclei impede their dissolution by a process inverse to the one occurring during cooling (Celik et al. 2010).

The resulting difference between the temperatures of freezing and melting is called „thermal hysteresis", and the ability to induce it is a typical trait of- antifreeze proteins (AFPs).

Specific arrangement of aminoacids in the ice-binding domain of the protein determines the crystal plane to which the protein can bind, as well as the strength of such binding. That in turn determines the magnitude of thermal hysteresis and the particular shape of the ice crystals that form when the solution is cooled.

The actual benefit of AFPs is then not its ability to bring about thermal hysteresis of bodily/intracellular fluids, but rather in limiting and suitably shapinig growth of the emerging ice crystals. Second major potential benefit of AFPs is the suppression of ice recrystallization during thawing (Ice Recrystallization Inhibition, IRI). Thawing phase of cryopreservation is at least as crucial as the cooling phase, and ice recrystallization may present (depending on cryopreservation protocol) a serious source of cryodemage. If the crystals are covered with adsorbed proteins, ice recrystallization is often strongly suppressed (Knight and Duman 1986; Zalis et al. 2013).

It is highly likely that many natural cryoprotectants and mechanisms of freezing protection used by freeze-tolerant organisms remain undiscovered. A case in point is the recent discovery of the role of Intrinsically Disordered Proteins (IDP) in the tolerance of Tardigrades towards desiccation (Boothby et al. 2017).

These proteins with loose structure form amorphous solids (vitrify) upon desiccation and thus protect other macromolecules from denaturation. Until now,

the established knowledge was that by far the most important cryoprotectant in tardigrades is trehalose, whose cryoprotective effects are explained in a similar manner. IDPs haven't yet been clearly implicated in cryoprotection but since the nature of dessication stress and low-temperature stress are in many aspects similar (dehydration, osmotic imbalance), such role is not unlikely.

The antifreeze protein ApAFP752 comes originally from a desert beetle Anatolica Polita living in the chinese Xinjiang province (Ma et al. 2012; Mao et al. 2011a; Mao et al. 2011b). Its molecular weight is around 20 kDa, and the active part of its structure is a set of β-sheet domains with regularly spaced threonine residues, aligned in a helical superstructure („β-helix") (**Fig. 1.3.4.1**).

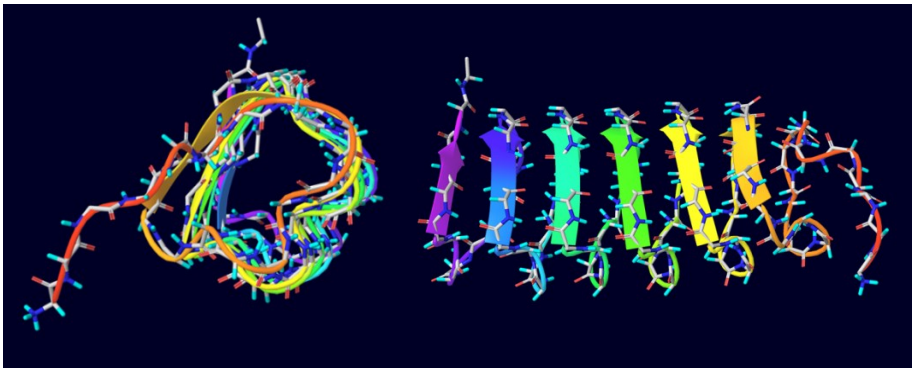

Fig. 1.3.4.1. The approximate structure of the antifreeze protein ApAFP752

This protein was shown to have a thermal hysteresis and ice-structuring activity, which is consistent with its assumed ice-binding properties. The magnitude of the hysteresis ranges between 0.5 and 5.5°C, depending on the pH and both on concentration of various ions and of the protein itself (Liu et al. 2015b). That makes it 10-fold more potent than e.g. a sea raven type II AFP, but much less so than a hyperactive protein TmAFP. ApAFP752 has been shown to confer significant cryoprotection to E. coli bacteria (Mao et al. 2011b).

1.4 Cellular structures and properties relevant for this work

1.4.1 Mechanical properties of the cell

The mechanical properties of a mammalian cell are closely related to its function. Probing these properties therefore represents a chemically noninvasive way to study the cell condition. Cell's shape, stiffness etc. are mainly determined by the structure and properties of its cytoskeleton. That consists of several distinct biopolymer networks, most importantly microfilaments, intermediate filaments and microtubules. Microfilaments, consisting of actin units, are thin (7 nm diameter) and flexible. They serve as a scaffolding for myosin molecules able to move along them (e.g. when transporting vesicles (DePina and Langford 1999)), and largely determine cell's shape. Together with non-muscle myosin and various cross-linking proteins, actin fibers can assemble into contractile stress fibers (Tojkander et al. 2012).

Intermediate filaments also contribute to the internal 3D structure of the cell. Their composition differs across various cell types and cell parts. Inside nucleus, they are made of lamin, providing support to the nuclear membrane and forming a major part of nucleoskeleton.

The cytoplasmic membrane consists of a partly fluidic lipid bilayer only about 10 nm thick. This bilayer can't itself hold its form nor resist pressure very well. It is, however, underlaid by cell cortex, a mesh approx. 200 nm thick consisting of actin fibers interconnected by spectrin molecules. This cortex is a mechanical support that the cytoplasmic membrane rests upon, and has therefore crucial influence on the apparent stiffness of the membrane. The cortex is directly linked to the cytoplasmic cytoskeleton, which allows for mechanotransduction of force from cell surface to cell interior (Pesen and Hoh 2005; Salbreux et al. 2012).

On the outer side of the cell, its physical properties are determined by the composition of the outer sheet of the plasma membrane. Outer membrane structure and composition determine the events that occur when the AFM tip is close to the point of contact with (or detachment from) the membrane (electrical forces, adhesion etc.).

The paper by (Ofek et al. 2009) shows how distinct types of cytoskeletal networks contribute to cell properties like stiffness, compressibility and Poisson ratio. For cell stiffness, actin (which constitutes the most of cell cortex) is the most important cytoskeletal component. When disrupted (by cytochalasin), stiffness is decreased by 40%. It is also demonstrated that disruption of microtubules (by colchicine) decreases the apparent Poisson ratio (by 30%) which is consistent with the finding that microtubules are important for maintaining the overall cell shape, and help anchor other cytoskeletal structures (Langelier et al. 2000). On the other hand, the state of actin and intermediate filaments doesn't seem to have an effect on the value of Poisson ratio. Apart from substances like cytochalasin, latrunculin or colchicine that have a direct impact on cytoskeleton assembly, there are other ways to affect cell stiffness, elasticity etc. Most generally, the cell regulates its mechanical properties by its gene expression. Any change in the latter may therefore have an impact on cell mechanics. A direct example of such link is presented in (Broers et al. 2004): a defect in the lamin A/C gene decreases cell stiffness and has a strongly detrimental effect on cell's ability to resist mechanical stress. As stated earlier, lamin is the main component of intermediate filaments that provide mechanical support to the nucleus, and the defect in question is found in patients suffering from various forms of muscle dystrophy or cardiomyopathy.

It has also been shown that in many cancer cells, a change in stiffness and deformability is a marker of their malignancy/metastatic potential (both positive and negative changes in stiffness have been reported for different cancer types (Janmey and Miller 2011; Xu et al. 2012). In the latter paper, which studies a specific type of ovarian cancer cells, the observed softening is due to actin cytoskeleton remodelling that takes place in these cancerous cells. Cell stiffness also changes in relation with senescence (Morgan et al. 2015) and cell death (Nikolaev et al. 2014), albeit in a non-uniform manner that is likely dependent on the precise way the cell dies. In bacteria, a large-scale screening of genes affecting cell stiffness has been performed in (Auer et al. 2016). Conversely, the cell perceives, and reacts to, the mechanical properties of its environment – its substrate, surrounding matrix and neighbouring cells (Bischofs and Schwarz 2003; Mitrossilis et al. 2009). By a process

termed mechanotransduction, such mechanical signals get translated into biochemical ones inside the cell, which then triggers a response.

1.4.2 Cell nucleus

The nucleus is a highly specialized organelle that serves as the information processing and administrative center of the cell. This organelle has two major functions: it stores the DNA and it coordinates the cell's activities, which include growth, intermediary metabolism, protein synthesis, and reproduction (cell division). The spherical nucleus typically occupies about 10 percent of a eukaryotic cell's volume, making it one of the cell's most prominent features.

A double bilayer membrane, the nuclear envelope, separates the contents of the nucleus from the cellular cytoplasm. The envelope is riddled with holes called nuclear pores that allow specific types and sizes of molecules to pass back and forth between the nucleus and the cytoplasm.

The nuclear envelope is supported by nuclear lamina, a fibrilar network consisting mainly of intermediate filaments. Lamina also plays an important role in chromatin organization (Gonzalez-Sandoval and Gasser 2016), DNA replication and cell division (Gruenbaum et al. 2003).

The semifluid matrix found inside the nucleus is called nucleoplasm. Within the nucleoplasm, most of the nuclear material consists of chromatin, a dense and highly organised structure consisting mostly of DNA (Kratochvílová et al. 2014a) coiled on histones.

Contradictory results in the literature have prevented a consensus on the extent of DNA and chromatin fragmentation that occurs during freezing and thawing (de Paula et al. 2006; Duru et al. 2001; Fraser et al. 2011; Paasch et al. 2004). Moreover, even subtle changes to the chromatin structure can be expected to affect the viability and/or genetic information of freeze-thawed cells.

Given the fundamental importance of cell nucleus for all cell activity, any pathological changes may pose a danger for proper cell functioning and

reproduction. Therefore, our work puts an emphasis on evaluating the consequences of cryopreservation on cell nucleus. Namely, we studied DNA integrity, chromatin higher-order structure, and shape and integrity of nuclear membrane.

2 Materials and Methods

The following chapter specifies the methodical details of the experiments featured in this work. For each result, the methods used are enlisted, including technical data. Furthermore, the sources of used materials and solutions are enclosed, as well as various software used for data processing.

2.1 Physical and physico-chemical methods/experiments

2.1.1 Materials

DMSO and trehalose were purchased from Sigma Aldrich, TrxA-ApAFP752 was expressed in the Department of Chemistry, University of Wyoming, 1000 E. University Ave, Laramie, WY, 82071, USA, and used in all the experiments in this work.

2.1.1.1 Expression and purification of recombinant TrxA-ApAFP752 fusion protein

The recombinant plasmid pET32b-*Apafp752* was transformed into *Escherichia coli* Rosetta-gami 2(DE3) or BL21 (DE3)pLysS competent cells (Novagen). A single transformed colony was used to inoculate 25 mL of Luria-Bertani medium containing 0.3 mM ampicillin and cultured overnight at 37°C and shaken at 225 rpm. 4 mL of the overnight culture was transferred into 1 L of fresh Luria-Bertani medium with 0.3 mM ampicillin and grown at 37°C and 225 rpm until the optical density at 600 nm (OD_{600}) reached 0.6-0.7.

The culture was induced with 1 mL of 400 mM isopropanol-1-thio-β-D-galactopyranoside (IPTG), to cause over-expression of TrxA-ApAFP752, for 8 hours at 25°C. The cells were harvested by centrifugation (20 minutes, 8700 g, 4°C) and stored at -80°C until purification. The cell pellet was resuspended with ice-cold binding buffer (EDTA-free Halt™ protease inhibitor cocktail (Fisher), 50 mM sodium phosphate, 150 mM NaCl, 20 mM imidazole and Benzonase nuclease (Millipore) at pH 8.0) and lysed using a French press (1300 psi).

The lysate was collected and centrifuged (20 minutes, 27200 g, 4°C) to remove the cell debris.

The supernatant was filtered through a 0.22 µm syringe-driven filter (Millipore) and concentrated to 5 mL before being purified by Fast Protein Liquid Chromatography (FPLC; GE Healthcare ÄKTA purifier 900) equipped with a HisTrap HP Ni-NTA column (GE Healthcare). The sample was loaded into the Ni-NTA column, washed with washing buffer (50 mM sodium phosphate, 150 mM NaCl, 20 mM imidazole at pH 8.0), and eluted with the same buffer containing 500 mM imidazole through a gradient elution. The fractions were pooled and dialysed in sodium phosphate buffer (50 mM sodium phosphate, 150 mM NaCl at pH 8.0) for 2 hours, then switched to fresh buffer and left overnight. The purity of the sample was analysed by 12.5% SDS-PAGE and stained with Coomassie blue; TrxA-ApAFP752 has a molecular weight of 27 kDa and was compared to a stained protein ladder (BioRad).

Additional purification steps were taken to obtain a pure sample and SDS-PAGE was used after each step to analyse the purity. The sample was divided into three fractions that were each concentrated to 1 mL and run through a Superdex 75 10/300 GL size exclusion column (GE Healthcare) equilibrated with sodium phosphate buffer. Fractions that were still not pure were run through a Ni-NTA column and dialysed for a second time.

Once the desired purity was obtained, the sample was buffer exchanged into a $K_xH_YPO_4$ buffer (50 mM potassium phosphate, 20 mM NaCl, and 1 mM NaN_3 at pH 8.0). The concentration was estimated using UV-Visible spectrophotometry at 280 nm with the calculated extinction coefficient of 19,575 $M^{-1}cm^{-1}$. The sample was concentrated to 1 mL and lyophilized overnight. For further experiments, the protein was rehydrated as needed and buffer exchanged.

2.1.2 Computer simulations of interactions between water and cryoprotectants

We used molecular dynamics to assess average hydrogen bond lifetimes in the solutions and DFT to calculate interaction energies between the cryoprotective solutions‘ constituents. These parameters offer a partial insight into the collective behaviour of those solutions (character of phase transitions, mechanism of its cryoprotective properties etc.).

For molecular dynamics simulations, the GROMACS 4.5.5 software package (Berendsen et al. 1995) and the AMBER99SB-ILDN force field (Lindorff-Larsen et al. 2010) were used. The simulations were carried out under periodic boundary conditions in explicit SPC/E water. For the calculation of long-range electrostatic interactions, the particle mesh Ewald method was used (Darden et al. 1993). To control the temperature of the ensemble, Berendsen thermostat was used in all simulations. Its relaxation time was set to 0.1 ps (both at room temperature and at -8°C). Each run (10 ns long) was preceded by 100 ps of equilibration.

The parameters for trehalose and DMSO residues were not available in the Amber99SB-ILDN force field, it was therefore necessary to derive the values of the missing parameters. To that end, we used a standard RESP (Restrained ElectroStatic Potential) procedure with charges taken from a HF/6-31G* calculation (M. J. Frisch 2010).

In order to perform calculations on the antifreeze protein ApAFP752, it was necessary to approximate its structure since it isn’t known exactly. This was done using the 3D-JIGSAW online structure prediction program (version 2.0) (Bates and Sternberg 1999). The prediction was based on the structure of another antifreeze protein from the beetle Tenebrio molitor (Liou et al. 2000) which has a 69% sequence homology to ApAFP752. The result was then refined using the program YASARA (Krieger and Vriend 2014). Most hydrogens were added automatically in the GROMACS environment, with the exception of histidine that was hydrogenated using a YASARA algorithm. Said algorithm optimizes the hydrogen bond networks while taking into account pKa and chemical conditions in the near environment of the aminoacid. As the initial geometry of trehalose, the crystal structure published

in (Nagase et al. 2008) was used. This was then gradient-optimized by DFT (using B3LYP-D3/6-31G*).

The individual samples were modelled under following conditions:

1) one trehalose saccharide molecule in a cubic simulation box surrounded by 500 water molecules
2) 56 DMSO molecules in a cubic simulation box surrounded by 2000 water molecules
3) four trehalose saccharide molecules and 56 DMSO molecules in a cubic simulation box with 2000 water molecules
4) ApAFP752 protein and two Cl^- ions were covered by a layer of 9043 water molecules, again in a cubic simulation box. These settings were chosen in order to reflect the conditions of the performed experiments.

Hydrogen bond forward lifetime τ_{HB} was used as a characteristic of the respective systems. Hydrogen bonds (their number, stability…) between water and cryoprotectant molecules are key for the behaviour of the solution in its liquid state, and even more so during its phase transitions. The hydrogen bonds were detected according to the geometrical configuration of the donor and acceptor. For an H-bond to exist, the distance between donor and acceptor had to be $r \leq r_{HB\text{-}max}$ 0.35 nm and the donor-hydrogen-acceptor angle α had to be less than $\alpha_{HB\text{-}max} = 30°$.

The bond's lifetime is then calculated from the autocorrelation function of the bond's existence criterion:

$$C_{HB}) = \frac{\langle s_i(t_0) s_i(t) \rangle}{\langle s_i{}^2(t_0) \rangle} \quad (1)$$

$s_i(t)=(0,1)$ for bond *i* at time *t*.

Next, hydrogen bond forward lifetime τ_{HB} is determined by (Krishnamoorthy et al. 2014; Luzar and Chandler 1993; Smiatek et al. 2013)

$$\tau_{HB} = \int_0^\infty C_{HB}(t)\mathrm{d}t \tag{2}$$

which yields an estimate for the average existence time. In order to evaluate H-bond time autocorrelation function correctly, at every 0.1 ps we recorded the trajectory in our simulations.

In order to estimate the interaction potential between individual molecules included in our study we computed the interaction energy ΔE_{int} *(BSSE)* with inclusion of the basis set superposition error (BSSE) using the following equation:

$$\Delta E_{int}\,(BSSE) = E_{dimer} - (E_{monomer1} + E_{monomer2}) + E_{BSSE} \tag{3}$$

where E_{dimer} is an electronic energy of a dimer system, $E_{monomer}$ is an electronic energy of monomer units and E_{BSSE} is a BSSE correction. The basis set superposition error was calculated using counterpoise corrections. Our computational procedure consisted of several steps:

1) gradient optimization of individual monomers with the B3LYP+D3/6-31G(d,p) method using the PCM model, which describes implicit water environment
2) geometry optimization of a few possible dimers of all investigated systems with the B3LYP+D3/6-31G(d,p) method using the PCM model
3) single point calculations directly performed on the optimized geometries of monomers and dimers with large basis set 6-311++G(d,p)
4) calculations of the basis set superposition correction with large basis set 6-311++G(d,p) in vacuo
5) applications of **Equation 1**.

2.1.3 Phase transitions parameters measured by differential scanning calorimetry (DSC)

A differential scanning calorimeter records the amount of heat absorbed or emitted by the sample during heating or cooling at a predefined rate. The output, a so-called DSC curve (heat flow vs. temperature or time) then reveals the positions and nature of phase transitions of the sample in the form of positive or negative peaks, or sigmoid regions in the case of glass transitions (Wowk 2010). This is because when e.g. the sample starts melting, suddenly a larger heat flow is needed to keep the predefined rate of warming. This manifests itself as a peak on the DSC curve. The position and character of phase transitions of cryoprotective media are crucial for the understanding of cell cryoinjury arising during each particular cryopreservation treatment. The composition of the samples measured by DSC is shown in **Tab. 2.1.3.1.**

Table 2.1.3.1. Solutions measured by DSC

Sample	Composition
Pure water	DI water
AFP	1% AFP solution
DMSO	10% w/w DMSO + DI water
DMSO + trehalose	10% w/w DMSO + 100 mM (3.2% w/w) trehalose +DI water
trehalose, low concentration	100 mM (3.2% w/w) trehalose + DI water
trehalose, medium concentration	15% w/w trehalose + DI water
trehalose, high concentration	41% w/w trehalose + DI water

The device used in our experiments was a DSC600 single-cell Calorimeter by Linkam, supplemented by the LNP95 cooling chamber. Since this chamber uses liquid nitrogen to cool the sample, it can reach temperatures as low as -196°C, it has

therefore sufficient range to cover the temperatures relevant for cryopreservation of biological samples.

The samples were scanned in two modes. First, an approximate localization of phase transitions was performed by cooling the sample down to -80°C at a rate of 5°C per minute, then equilibrating it for 5 minutes, and finally warming it back up to room temperature at the same rate. Next, the sample was repeatedly cooled and thawed in the range given by its freezing temperature T_f and melting temperature T_m at a rate of 1°C, with 10 minutes long equilibration between cooling and thawing. This way, T_m and T_f was determined with greater accuracy (±1°C).

2.1.4 X-ray diffraction (XRD)

This method was employed in order to measure the structure of frozen solutions of various cryoprotectants. Namely, it is able to describe „crystallinity“ of the sample: the amount, size distribution and relative orientation of water crystals present in the sample. Those are factors that partly determine whether the environment in the solution during freezing is favourable or hostile for the cryopreserved cells. On top of that, it is also possible to monitor the very process of freezing and thawing. That way, for instance, ice recrystallization (and its inhibition) can be observed. The composition of samples measured by XRD (and also by Raman spectroscopy) is shown in **Tab. 2.1.4.1**.

For the XRD measurements, a Bruker D8 horizontal diffractometer was used. A 12-kW copper rotating-anode was used as a source. Samples were placed in an aluminium cuvette and then inserted in an Anton Paar DCS 350 dome-type cooling chamber. The collimation of the incident beam was done by a Goebel mirror (horizontal divergence ca. 0.02°, vertical divergence ca. 4°). The device was set to detect the 110 reflection of hexagonal ice. Angular mapping (in the ω and χ direction) of each sample was then performed. The detector was placed at a fixed angle of 39.85° (2 θ), which corresponded to an integration angle of ± 0.15°. The angular mapping was achieved by tilting the sample around the ω and χ axes. Horizontal tilt (ω) ranged between 5° and 35° with steps of 0.02° while the vertical

tilt (χ) moved from -4° to +16° with steps of 2°. The resulting solid angle amounts to 0.12 sr. Since a hexagonal ice crystal gives rise to six 110 reflections that are evenly inclined (per 60°) in the basal plane, no such crystal could have more than 1 of its reflections recorded under our experimental setting. Therefore, the chance of detecting such a crystal was around 5.8%. It must therefore be emphasized that for each sample, only about 1/17 of all crystallites was observed, and that the total number of crystallites influences the quality of statistical analysis of a given sample. The signal was accumulated for 90 minutes with the temperature held constant. The difractograms were then processed in order to obtain the size distribution of present crystallites (assuming that the peak difracted intensity is qualitatively proportional to the third power of a crystallite diameter, and that the angular profile of a difracted beam is gaussian). In order to filter out possible overlapping of diffraction peaks, deconvolution was used.

Table 2.1.4.1. Composition of samples for XRD

Sample	Composition
water	deionized (DI) H_2O
DMSO solution	DMSO 10% (w/w) in DI water
DMSO + trehalose solution	DMSO 10% (w/w) + trehalose 3.2% (w/w) resp. 41% (w/w) in DI water
AFP solution	0.05%, 0.1% or 1% (w/w) TrxA-ApAFP752 in PBS 50 mM $Na_xH_yPO_4$, 50 mM NaCl)
trehalose solution	41% (w/w) trehalose in DI water

The warming was performed at a rate of 1°C, with temperature being held constant during each signal acquisition. The starting temperature for most samples was -50°C, with the acquisition steps ranging between 2 and 15°C (optimized for each cryoprotectant and acquisition temperature).

2.1.5 Raman spectroscopy

Raman spectroscopy is able to detect both intramolecular and lattice vibrations of the sample (Kratochvílová et al. 2014b). These are characteristic of its composition and phase. Here, this method is used to monitor changes in the cryoprotective solutions during freezing and thawing, their homogeneity and phase composition.

Raman measurements were performed on a Renishaw RM1000 spectrometer combined with a Leica DMLP microscope. For temperature control, Linkam LNP95 cooling stage was used (temperature control precision is 0.01°C, lowest available temperature was -196°C). The excitation wavelength was 488 nm and the objective used was Leica PL FLUOTAR L 50x/0.55 (an objective with a long working distance was necessary because of the distance between the sample and the cover glass of the cooling stage). Samples (**Tab 2.1.5.1)** were mounted on the stage in Perkin Elmer aluminium pans with 50 µl volume. Since freezing led to high opacity of the samples, the signal was collected from a surface layer whose thickness was estimated to be around 5 µm. The resulting spectra were normalized at 3175 cm^{-1}. For each sample, multiple spectra were measured.

Table 2.1.5.1. Composition of samples for Raman spectroscopy

Sample	Composition
PBS	50 mM phosphate ($Na_xH_yPO_4$) and 50 mM NaCl in DI water
DMSO in PBS	DMSO 0.8% (w/w) in PBS
trehalose in PBS	trehalose 13.2% (w/w) in PBS
AFP in PBS	0.1% (w/w) TrxA-ApAFP752 in PBS

2.2 Experiments on cells

Cryopreserved cells were treated with PEG-1500, glycerol, DMSO, trehalose (purchased from Sigma Aldrich) and TrxA-ApAFP752. TrxA-ApAFP752 was expressed in the Department of Chemistry, University of Wyoming, 1000 E. University Ave, Laramie, WY, 82071, USA, expression is described in part 2.1.1.1.

2.2.1 Cryopreserved cells viability measured by flow cytometry

In order to estimate the cryoprotective efficacy of the solutions whose physico-chemical properties were probed by XRD, DSC, Raman spectroscopy and molecular modelling, we checked the viability of cells frozen/thawed in these solutions.

Flow cytometry was used to quantify survival and apoptosis in cells that were frozen with or without cryoprotectants. The Muse® Cell Analyser (Merck Millipore) and Muse® Annexin V & Dead Cell Assay Kit (MCH100105, Millipore), which can discriminate between live, early apoptotic, late apoptotic/necrotic and dead cells, were used according to (Hofer et al. 2016a). To allow the cells to enter apoptosis, flow cytometry measurements were performed 24 h after the cryoprotectant treatment (in the case of non-frozen cells) or after thawing (in the case of frozen cells).

Cells were frozen by cooling to -80°C using a gradient of -1°C/min in standard medium (untreated cells). Cryoprotectant-treated cells were preincubated prior to cooling (to -80°C using a gradient of -1°C/min) in standard medium containing either trehalose for 24 h, in DMSO for 2 min or in AFP for 2 h (**Tab. 2.2.1.1**).

Tab. 2.2.1.1. Cryoprotectants solutions used for cell viability measured by flow cytometry

Sample	Composition
DMSO	DMSO 10% (w/w) in DMEM (cell culture) medium
DMSO + trehalose	DMSO 10% (w/w) **+** 100 mM trehalose 3.2% (w/w) in DMEM (cell culture) medium
AFP	0.5 $mg.ml^{-1}$ in DMEM (cell culture) medium
Trehalose	3.2% (w/w) (100 mM trehalose in DMEM (cell culture) medium

2.2.2 Mechanical properties of cryopreserved cells

Atomic Force Microscopy is an imaging method using direct mechanical interaction between a scanning tip and the sample to obtain data about sample topography.

We used AFM in the Force spectroscopy mode in which the tip descends down and indents the sample until a pre-set deflection is achieved. After that, the tip retrieves back up. The obtained data then contains the dependence of cantilever deflection on its position above (or in) the sample. That data can be plotted as a so-called force-distance curve (FDC) which is then fitted by an appropriate indentation model in order to extract the value of cell Young's Modulus (YM), denoted *E*. This was a novel way of characterizing the recovery process of thawed cells by monitoring their mechanical properties during their culturing.

Two sets of AFM experiments were performed. In the first set, the cells were measured with a pyramidal indentor and the goal was to:

a) describe the impact of cell incubation with selected cryoprotectants on cell mechanical properties. Hence the never-frozen cells were mapped while incubated in the medium containing a cryoprotectant (DMSO or glycerol)
b) track the recovery of cell mechanical properties after cryopreservation in DMSO, hence the frozen/thawed cells were measured after removing DMSO

from the culturing medium. As a control, cells irradiated prior to freezing (in order to block their cell cycle and reparation) were also measured.

In the second set of experiments, cells were frozen with two different cryoprotectants (either intracellular DMSO or extracellular PEG-1500). After thawing and medium exchange, the cells were measured with a spherical indentor over several hours. Thus, time series of AFM height- and stiffness maps were acquired.

2.2.2.1 Cryopreserved cells regeneration monitored by atomic force microscopy (AFM)

2.2.2.1.1 Cells treatment

Both non-irradiated (non-IR) and irradiated (IR) mouse embryonic fibroblasts (MEFs) (CF-1 mouse strain) were propagated till passage 3 (P3). IR fibroblasts were mitotically inactivated by gamma irradiation at 50 Gy delivered in 30 min (^{137}Cs; irradiator OGL from VF a.s. Cerna Hora, Czech Republic). Suspension of MEFs P3 was frozen in the amount of one million of cells per 2 ml cryo tube (TPP, Trasadingen, Switzerland). Freezing was done by addition of 0.8 ml of ice-cold freezing medium drop by drop into 0.8 ml of MEF suspension in MEF medium consisting of Knockout Dulbecco's modified Eagle's medium (KO-DMEM; Gibco), 10% heat-inactivated fetal bovine serum (FBS; Invitrogen), 1% L-glutamine (Gibco), 1% non-essential amino acids (PAA), 1% penicillin-streptomycin (PAA), and 0.1 mM β-mercaptoethanol (Sigma). Composition of freezing medium was KO-DMEM : FBS : DMSO = 3 : 1 : 1 (v/v/v); Dimethyl sulfoxide (DMSO), Hybri-Max™ (Sigma).

After the thawing procedure was finished, the Petri dish containing cells was incubated in standard CO_2 incubator for only 30 minutes in order to initialize the adhesion process. Then the dish was taken out of the incubator, installed in the AFM dish holder preheated during the calibration process.

2.2.2.1.2 Young's modulus mapping by atomic force microscope

Standard bio AFM microscope JPK NanoWizard 3 (JPK, Berlin, Germany) was used to perform force mapping procedure. The scanning-by-probe head (maximal visualization range 100-100-15 µm in X-Y-Z axis) of the AFM system was placed on inverted optical microscope Olympus IX-81, 10x objective was used to find proper area covered with cells and to place cantilever in the proper position for the force mapping procedure. Plastic Petri dish with either the distilled water for instrument calibration or with the fibroblast culture was placed inside the Petri dish heater (JPK) preheated to 37 ^{o}C.

Non-coated silicon nitride AFM cantilever Hydra 2R-100N (AppNano, Mountain View, CA, USA) equipped with pyramidal silicon tip was used for all experiments. The probe was calibrated prior to every experiment as described below.

The calibration procedure was done in double distilled water, when the whole setup was preheated (Petri dish heater) to 37 ^{o}C for 30 minutes. Then the laser reflection sum was maximized, followed by centering of the laser detector. The AFM probe was introduced in contact with the surface during a standard process of landing. The sensitivity of the AFM setup was determined as a slope of the force-distance curve measured by lifting the cantilever with Z-height of 450 nm, time per curve was 3 seconds. The sensitivity was found in the range 15.07-15.37 nm/V, cantilever stiffness was calibrated by measurement of its thermal noise and lay between 17.34 and 19.19 nN/m for different days of experiments.

The bio AFM setting was identical for all the force mapping procedures. Set Point value was 1.0 nN (relative to baseline value), time per curve 0.45 s, Z-length 15.0 µm, speed of curve recording 33.3 µm/s, the force-distance curves were recorded with data sample rate of 2 kHz. The force mapping procedure was performed as step-by-step recording of force-distance curves in the network of 64x64 points on 55x55 µm covering area of single fibroblast cell.

Reproducibility of the nanomechanical measurement was performed by repeated force mapping process on identical place (scanning over the identical cell).

Neither medium exchange nor AFM instrument adjustment was involved during the repeated mapping procedure (Dimitriadis et al. 2002; Gavara and Chadwick 2012).

Place-to-place reproducibility was studied, when the identical force mapping experiments were subsequently performed on two different places found randomly on the Petri dish surface covered with fibroblasts. Measurements were made on 3 sets of samples, each set contained 2-3 cells.

Before the measured AFM data were further processed and interpreted, all parts of each sample corresponding to the plastic dish were algorithmically removed using Gwyddion (Necas and Klapetek 2012) or Mathematica software (Wolfram Research 2017).

2.2.2.1.3 Monitoring of cell growth

Surface stiffness of the fibroblasts cultured on a Petri dish shortly (30 minutes) after thawing process was monitored during overnight nanomechanical mapping of the fibroblast cell. Petri dish containing freshly thawed suspension of cells was for a short period pre-incubated in a standard CO_2 incubator. When first cells started to adhere, culturing medium in the dish was completely exchanged and force mapping process was started immediately. AFM measurement was performed during continuous experiment of repeated force mapping process on identical place. Parameters identical to other mapping processes were used also in this case. Neither medium exchange nor AFM instrument adjustment was involved during the repeated mapping procedure.

2.2.2.1.4 Effect of DMSO or glycerol in culturing media on cell stiffness

Effect of DMSO and glycerol application (both form Penta, Prague, Czech Republic) on cell stiffness was tested during subsequent measurement of force maps in the presence of 5, 10, 15 and 20% of the solvent in standard MEF culturing medium. First, the Petri dish with cultured fibroblasts was filled with MEF medium with no addition of solvent and force map was recorded to obtain base line values of cell stiffness under standard conditions. The whole internal volume of the Petri dish was then depleted by standard medical syringe connected with the inner space

of the dish via stainless steel tubing fixed inside the Petri dish heater; AFM cantilever was kept in contact with sample surface. The Petri dish was immediately filled with preheated MEF medium containing appropriate amount of the solvent, after 3 min of temperature adjustment the force mapping of the identical area was started. After 45 min, when the process of nanomechanical mapping was finished, the inner volume of the dish was completely exchanged with MEF medium containing higher concentration of the solvent – the solvent concentration in the following sequence 5, 10, 15 and 20% was used.

When the stiffness of a single cell is investigated by the AFM indentation method on a large area, usually not only the cell is captured, but also the surrounding plastic surface. However, plastic (polystyrene dish) stiffness is about three orders of magnitude higher compared to the cell. It was therefore possible to identify the parts of each AFM image corresponding to the plastic surface by setting a YM threshold. Points exceeding the threshold were masked from further analysis using the Gwyddion software (Necas and Klapetek 2012).

2.2.2.1.5 Statistical evaluation of data

Quantitative data of Young's modulus were calculated as the mean ± the standard error of the mean from experiments in the time points where force-mapping procedure was finished simultaneously (duration depends on cell topography). In all cases the standard error was less than 7%. When values of YM within certain time interval were compared, the normality of data distribution was evaluated by Shapiro-Wilk method thus proving the data normality at 0.05 level.

2.2.2.1.6 Viability of cells determination

The viability of the cells tested by AFM testing was checked at the timepoints from 30 min (denoted "0 hours") to 6 hours 30 min (denoted "6 hours") to correspond to force mapping procedures. The cells were washed to exclude floating cells, trypsinized and collected into tubes. Cell suspension was then incubated in 0.5% TrypanBlue solution (1:1) for 2 min and viable cell ratio was counted on hematocytometer.

2.2.2.1.7 Data processing

Force mapping process provides a grid of force-distance curves (FDC, dependency of tip-sample interaction force on tip height above the surface), so called force maps (FM). The absolute value of Young's modulus was determined by fitting the FDC by **Equation 4** - pyramidal indentation model by Bilodeau (Bilodeau 1992).

$$F(\delta) = \frac{1.4906\, E\, tan\alpha}{2\,(1\text{-}\upsilon^2)}\delta^2 \tag{4}$$

where *F* is the measured force, *E* – Young's modulus, *v* - Poisson ration (0.5 for incompressible materials), *δ* is tip-sample separation (obtained by correction of the cantilever height to its bending) and *α* is half-angle to face of pyramidal tip (reflects the tip geometry).

Relative value of Young's modulus was calculated as ratio of the actual stiffness value relativized to initial value of stiffness in the first time point of time dependency:

$$E_{rel} = \frac{E_t}{E_{in}} * 100\% \tag{5}$$

where E_{rel} is relative value of Young's modulus, E_t is its value in the time point and E_{in} is value of YM in the initial time point.

The fitting of FDC by **Equation 4** was performed in the AtomicJ software (Hermanowicz et al. 2014), with the contact point position estimated by an incorporated Robust Exhaustive algorithm and best fit found by the Robust HLTA algorithm. Poisson ratio was set to 0.5. In all cases, the fitting was performed on the approach curve. Resulting Young's modulus maps were exported in order to be post-processed in Wolfram Mathematica (Wolfram Research 2017).

After the fitting, some points were removed from the YM maps based on the values of various parameters of the corresponding fit. First, a threshold of 50 kPa was introduced for the YM value in order to exclude all curves measured over the dish surface or over very thin cell regions. Furthermore, all fits yielding indentation greater than 2.5 µm were filtered out as such a large indentation always meant a faulty contact point estimation. Here, indentation was defined as the indentation

depth difference between the shallowest (i.e. contact) point and the deepest point of the fitted part of the force-distance curve (FDC).

Also, the indentation force at the deepest point of the fitted region was less than 80% of the total set point, the corresponding curve was removed. Thus, FDCs whose fitted region was too small were not taken into consideration.

We excluded force curves which couldn't be well described by the Bilodeau model with single *E* value (i.e. they typically contained a significantly stiffened region at larger depths). Such curves were typically located in the border regions of the measured cells. In the remaining curves, it was therefore not necessary to employ modified indentation models incorporating e.g. the bottom effect cone correction

Finally, the adequacy of the Bilodeau model was checked. The curves kept for final statistical analysis had root-mean-square deviation of the model from the actual data points smaller than 5% of the maximum set point, and the maximum deviation of the model values from the measured data was always smaller than 7% of the maximum set point.

After applying all filters, 70 – 80% of curves and corresponding YM values were left for statistical analysis.

Also, minimal deviations between calculated results and the measured data (the least squares method) were taken into consideration. Such curves were taken into consideration in which at each point maximum deviation of the measured data from the model values was smaller than 7% of the measured data.

2.2.2.2 AFM monitoring the influence of selected cryoprotectants on regeneration of cryopreserved cells mechanical properties

2.2.2.2.1 Cell culture, freezing and sample preparation

Mouse embryonic fibroblasts (MEFs) (CF-1 mouse strain) were propagated on 100 mm Petri dish in MEF medium (MEF medium consists of Knockout Dulbecco's modified Eagle's medium (KO-DMEM; Gibco), 10% heat-inactivated fetal bovine serum (FBS; Invitrogen), 1% L-glutamine (Gibco), 1% non-essential amino acids (PAA), 1% penicillin-streptomycin (PAA), and 0.1 mM β-mercaptoethanol from

Sigma) until passage 2 (P2). A confluently grown cell culture was washed with PBS a trypsinized (Trypsin EDTA, Invitrogen, Ca USA) for 2 min and collected into centrifuge tube. The cell suspension was spinned by 200 g/4 min and resuspended to concentration 1 000 000 cells/ml. 200 000 cells (in 0.2 ml of MEF medium) were placed into 2 ml cryo tube (TPP, Trasadingen, Switzerland). Freezing was done by addition of 0.2 ml of ice-cold freezing medium drop by drop into the tube.

Variable freezing media were used in final concentrations as follows: DMSO freezing medium consisting of 80% KO-DMEM, 10% FBS and 10% DMSO (Hybri-Max™, Sigma); DMSO/trehalose freezing medium consisting of 76.8% KO-DMEM, 10% FBS, 10% DMSO and 3.2% (50 μM) trehalose; PEG-1500 freezing medium consisting of 82.5% KO-DMEM, 10% FBS and 7.5% polyethylene glycol (Mw 1500; PEG-1500). The tubes were placed in in Nalgene dish for 24 hours in -80°C, then transferred to liquid nitrogen until measurement.

Cryo tube with MEFs P2 was taken out from liquid nitrogen (Dewar flask) and cell suspension was quickly thawed in stream of hot water until the point, where a few remaining crystals were visible in the tube. The whole volume was immediately transferred into the 15 ml centrifuge tube and 12 ml of cold (4°C) MEF medium was added dropwise from Pasteur pipette. The tube was centrifuged (200 g, 4°C) for 4 minutes, the excess of MEF medium above the cell pellet was removed by pipette, cells were resuspended in 1 ml of MEF medium (37°C) and 0,5 ml distributed onto 35 mm low Ibidi dish (Ibidi GmbH, Martinsried, DE) for AFM measurements.

The dishes were placed into standard CO2 incubator for 20 min for the cells to attach. For AFM measurements, all unattached cells from Ibidi dish were removed by PBS wash and fresh MEF medium was added into the dish, installed in the AFM dish holder preheated during the calibration process and after the AFM instrument adjustment, the force mapping measurement was immediately started.

2.2.2.2.2 Young's modulus mapping by Atomic Force Microscope

Standard bio AFM microscope JPK NanoWizard 3 (JPK, Berlin, Germany) was used to perform force mapping procedure. The scanning-by-probe head (maximal visualization range 100-100-15 µm in X-Y-Z axis) of the AFM system was placed on inverted optical microscope Olympus IX-81, 10x objective was used to find proper area covered with cells and to place cantilever in the proper position for the force mapping procedure. Plastic Petri dish with either the distilled water for instrument calibration or with the fibroblast culture was placed inside the Petri dish heater (JPK) preheated to 37 ^{o}C.

We compared set points, indentation depths and the Young modulus of cultivated cells for measurements performed by the spherical and pyramidal AFM tips, respectively. For spherical tip and small set points (e.g. lower than 0,5 nN) the contact parts of force curves were not sufficient for reliable fits. On the other hand, force curves obtained with pyramidal tip and higher set point values (1.5 nN and above) were often not smooth. The notches observed on the curves likely corresponded to structural damage of the measured cells.

When using a spherical probe at high (1nN) set point, cells were indented down to similar depth as when using the pyramidal probe at low set point (lower than 0.5 nN) with close values (deviation less than 8%) of obtained Young Modulus. Based on these considerations, we chose to use the spherical probe with set point 1 nN. Thus, the elastic properties of the cells could be probed down to significant indentation depths (approx. 0.5 – 1 um) while avoiding structural damage to the measured cells. Furthermore, the obtained YM values were less susceptible to variations caused by small-scale membrane and submembrane features thanks to the large contact surface of the colloidal probe (as opposed to the pyramidal tip). Non-coated silicon nitride AFM cantilever Hydra 2R-100N (AppNano, Mountain View, CA, USA) equipped with spherical probe (radius 3.31 micrometer) was used for all experiments. The probe was calibrated prior every experiment as described below.

The calibration procedure was done in double distilled water, when the whole setup was preheated (Petri dish heater) to 37 ^{o}C for 30 minutes. Then the laser reflection sum was maximized, followed by centering of the laser detector. The AFM probe was introduced in contact with the surface during a standard process of landing. The sensitivity of the AFM setup was determined as a slope of the force-distance curve measured by lifting the cantilever with Z-height of 450 nm, time per curve was 3 seconds. The sensitivity was found in the range 15.07-15.37 nm/V, cantilever stiffness was calibrated by measurement of its thermal noise and lay between 17.34 and 19.19 nN/m for different days of experiments.

The bio AFM setting was identical for all the force mapping procedure. Set Point value was 1.0 nN (relative to baseline value), time per curve 0.45 s, Z-length 15.0 µm, speed of curve recording 33.3 µm/s, the force-distance curves were recorded with data sample rate of 2 kHz. The force mapping procedure was performed as step-by-step recording of force-distance curves in the network of 64x64 points on 75x75 to 100x100 µm^2 covering area of either single or more fibroblast cells.

Reproducibility of the nanomechanical measurement was performed by 5-times repeated force mapping process on identical place (scanning over the identical cell). Neither medium exchange nor AFM instrument adjustment was involved during the repeated mapping procedure.

Place-to-place reproducibility was studied, when the identical force mapping experiments were subsequently performed on two different places found randomly on the Petri dish surface covered with fibroblasts.

Before the measured AFM data were further processed and interpreted, all parts of each sample corresponding to the plastic dish were algorithmically removed using Wolfram Mathematica (Wolfram 2017).

2.2.2.2.3 Long term monitoring of the cryopreserved cells properties development

Surface stiffness of the fibroblasts cultured on a Petri dish shortly (30 minutes) after thawing process was monitored during overnight nanomechanical mapping of the fibroblast cell. Petri dish containing freshly thawed suspension of cells was for a short period pre-incubated in a standard CO_2 incubator. When first cells started to adhere, culturing medium in the dish was completely exchanged and force mapping process was started immediately. Nanomechanical measurement was performed during 4 hours continuous experiment of repeated force mapping process on identical place. Parameters identical to other mapping processes were used also in this case. Fluorescence stack images were obtained before each force mapping process, and at the end of the whole time elapsed measurements.

Force mapping process provides a network of force-distance curves (FDC, dependency of tip-sample interaction force on tip height above the surface), so called force maps (FM)(Bilodeau 1992; Dimitriadis et al. 2002; Touhami et al. 2003). The absolute value of Young's modulus can be determined by fitting the FDC by **Equation 6** (spherical probe, Hertz-Sneddon model)(Gavara and Chadwick 2012; Sneddon 1965).

$$F = \frac{E}{(1v^2)}\left(\frac{R^2 + a^2}{2} Log\left(\frac{R + a}{Ra}\right) aR\right)$$

$$\delta = \frac{a}{2} Log\left(\frac{R+a}{R-a}\right) \quad (6)$$

where *F* is force, *E* – Young's modulus, *v* - Poisson ration (0.5 for incompressible materials), δ – depth of indentation; a – contact radius.

The fitting of FDC by **Equation 6** was performed in the AtomicJ software (Hermanowicz et al. 2014), with the contact point position estimated by an incorporated Robust Exhaustive algorithm and best fit found by the Robust HLTA algorithm. Poisson ratio was set to 0.5. In all cases, the fitting was performed on the approach curve. Resulting Young's modulus maps were exported in order to be post-processed in Wolfram Mathematica (Wolfram 2017).

After the fitting, some points were removed from the YM maps based on the values of various parameters of the corresponding fit. First, a threshold of 10 kPa was introduced for the YM value in order to exclude all curves measured over the dish surface or over very thin cell regions.

Furthermore, all fits yielding indentation greater than 2 μm were filtered out as such a large indentation always meant a faulty contact point estimation. Here, indentation was defined as the indentation depth difference between the shallowest (i.e. contact) point and the deepest point of the fitted part of the FDC.

Also, if the indentation force at the deepest point of the fitted region was less than 80% of the total set point, the corresponding curve was removed. Thus, FDCs whose fitted region was too small were not taken into consideration.

Among other benefits, these constraints helped us to exclude force curves which couldn't be well described by the Hertz-Sneddon model with single *E* value (i.e. they typically contained a significantly stiffened region at larger depths). Such curves were typically located in the border regions of the measured cells. In the remaining curves, it was therefore not necessary to employ modified indentation models incorporating e.g. the bottom effect cone correction (Gavara and Chadwick 2012).

Finally, the adequacy of the Hertz-Sneddon model was checked. The curves kept for final statistical analysis had root-mean-square deviation of the model from the actual data points smaller than 5% of the maximum set point, and the maximum deviation of the model values from the measured data was always smaller than 7% of the maximum set point. After applying all filters, 90% of curves measured on cells and corresponding YM values were left for statistical analysis.

Also, minimal deviations between calculated results and the measured data (the least squares method) were taken into consideration. Such curves were taken into consideration in which at each point maximum deviation of the measured data from the model values was smaller than 7% of the measured data.

2.2.2.2.4 Viability of cells

Flow cytometry was used to quantify survival and apoptosis in cells that were frozen with or without cryoprotectants. The Muse® Cell Analyser (Merck Millipore) and Muse® Annexin V & Dead Cell Assay Kit (MCH100105, Millipore), which can discriminate between live, early apoptotic, late apoptotic/necrotic and dead cells, were used according to (Hofer et al. 2016a).

The viability of the cells tested by AFM testing was checked at the time points from 30 min (denoted „0 hours“) to 4 hours in order to correspond to force mapping procedures. The wells were washed to exclude floating cells, trypsinized and collected into tubes. Cell suspension was then incubated in 0.5% TrypanBlue solution (1:1) for 2 min and viable cell ratio was counted on hematocytometer.

2.2.2.2.5 Statistical evaluation of data

Quantitative data of Young's modulus were calculated as the mean ± the standard error of the mean from 3 experiments. In all cases the standard error was less than 7%. When values of YM within certain time interval were compared, the normality of data distribution was evaluated by Shapiro-Wilk method thus proving the data normality at 0.05 level.

After measuring the force curves across the whole area, each force curve was fitted with the Hertz-Sneddon model, which yielded the YM value. Then, we removed the YM values that resulted from a faulty (aforementioned) fit (or rather a fit of faulty curves which occasionally occurred in the set). In the remaining set of curves, we analyzed the distribution of YM values in different surface parts (upper and lower half) and also calculated mean and median of the whole cell YM.

2.2.3 Critical defects in nuclear structures of cryopreserved cells nuclei (envelope disruption, chromatin condensation, DNA breaks)

2.2.3.1 Cells and cell culture

Certified normal human forskin fibroblasts BJ-5ta (NHDF) and human breast adenocarcinoma cells (MCF7) were obtained from CLS Cell Lines Service GmbH (Eppelheim, Germany), cultivated in DMEM medium (PAN Biotech, Aidenbach, Germany, cat. no: P03-0710), supplemented with 10% fetal calf serum (PAA Laboratories GmbH, Pasching, Austria) and 1% penicillin + streptomycin (stock solution mixture 10 000 U/mL penicillin + 10 mg/mL streptomycin; PAN Biotech, cat. no.: P06-07100), at 37°C in a humidified atmosphere of 5% CO_2. The cells obtained (at passage 2) were freshly thawed, multiplied, and used for experiments in low passages (about 5-7) to prevent possible effects of senescence on chromatin structure and cell functions.

2.2.3.2 Cryoprotectants and cells freezing

Aqueous DMSO and DMSO+trehalose solutions containing 50 mM sodium phosphate and 50 mM NaCl in DI water (pH 8.0) were used (phosphate-buffered saline, PBS). We also prepared 1% (w/w) solution of the fusion protein TrxA-ApAFP752 in PBS or DI water (AFP solution). D-(+)-trehalose dihydrate and DMSO were purchased from Sigma-Aldrich. DI water was purified by the Milli-Q Plus system (Millipore) and had a resistance of 18.2 MΩ.cm (25°C). Human fibroblasts and MCF7 cells were frozen down to -80°C using a gradient of -1°C/min in culture media supplemented with a given cryoprotectant (**Tab. 2.2.3.2.1.**).

Table 2.2.3.2.1. Cryoprotectants used for cell protection against freeze/thaw damage.

Sample	Composition
AFP	0.5 $mg.ml^{-3}$ in DMEM (cell culture) medium
trehalose	3.2% (w/w) in DMEM (cell culture) medium
DMSO	DMSO 10% (w/w) in DMEM (cell culture) medium
DMSO + trehalose	DMSO 10% (w/w) + 100 mM trehalose 3.2% (w/w) in DMEM (cell culture) medium

2.2.3.3 Irradiation

Cells were irradiated in the culture medium at 37°C from a ^{60}Co source (Chisostat, Chirana, Prague, Czech Republic) with a dose of 1 Gy or 2 Gy (γH2AX/53BP1 foci immunofluorescence) or 5 Gy (flow cytometry); the dose rate was 1.0 Gy/min. During the irradiation, the cells were kept in a thermostable box, ensuring a constant temperature and prevention from infection during the whole procedure. After irradiation, the cells were immediately placed back into the incubator (37°C/5% CO2) until the fixation.

2.2.3.4 γH2AX phosphorylation by flow cytometry

Flow cytometry was used to quantify γH2AX phosphorylation in cells that were frozen with or without cryoprotectants. The Muse® Cell Analyser (Merck Millipore) and Muse® H2A.X Activation Dual Detection Kit (MCH200101, Merck Millipore), which discriminate between H2AX (-)/H2AX (-) vs. H2AX (+)/H2AX (-) vs. H2AX (-)/H2AX (+) and H2AX (+)/H2AX (+) cells, were used according to the manufacturer's instructions. The cell state was analysed 1 h and 4 h after the cells were thawed.

2.2.3.5 Cell cycle by flow cytometry

The Muse® Cell Analyser (Merck Millipore) and Muse® Cell Cycle Assay Kit (MCH100106) were used according to the manufacturer's instructions (Merck).

2.2.3.6 Immunostaining

DSBs were quantified by high-resolution confocal microscopy as foci showing dual co-localization of H2AX and 53BP1; together, these proteins are generally accepted as DSB markers (Stokich et al. 2014). The proteins were visualized using a mouse monoclonal antibody against H2AX phosphorylated at serine 139 (H2AX) (dilution 1:500; Upstate) and with a rabbit polyclonal antibody against 53BP1 (dilution 1:500; Upstate). The maximum DSB signals typically appeared about 30 min post-DSB induction (Kozubek et al. 2001). Hence, after complete thawing, the cells were maintained for an additional 30 min in the incubator (37°C, 5% CO_2) in fresh pre-heated (37°C) DMEM medium supplemented with 10% FCS to allow full development of the foci.

Secondary antibodies, namely, affinity-purified donkey anti-mouse-FITC-conjugated antibody (dilution 1:100) and affinity-purified donkey anti-rabbit-Cy3-conjugated antibody (dilution 1:200) (ImmunoResearch Laboratories, West Grove, PA), were used to visualize the primary antibodies. The immunostaining procedure was performed as described in (Falk et al. 2008) and (Sevcik et al. 2012) with minor modifications. The nuclear envelope was stained with anti-lamin A/C monoclonal mouse antibody (dilution 1:1000; Sigma-Aldrich). Nuclear chromatin was counterstained with 1 µM TO-PRO3 (Molecular Probes, Eugene, USA) in 2× saline sodium citrate (SSC) prepared fresh from a stock solution. After the cells were briefly washed in 2× SSC, the samples were mounted using Vectashield medium (Vector Laboratories, Burlingame, CA, USA).

2.2.3.7 Cell survival (flow cytometry and Trypan blue exclusion assay)

Flow cytometry was used to quantify survival and apoptosis in cells that were frozen with or without cryoprotectants. The Muse® Cell Analyser (Merck Millipore) and Muse® Annexin V & Dead Cell Assay Kit (MCH100105, Merck Millipore), which discriminate between Annexin V (+)/Propidium Iodide (+) (live) vs. Annexin V (+)/Propidium Iodide (-) vs. Annexin V (-)/Propidium Iodide (+) and Annexin V (-)/Propidium Iodide (-) cells, were used according to the manufacturer's instructions. The cell state was analysed 30 min or 24 h after the cells were thawed. Trypan blue exclusion assay was used according to standard protocol as an alternative method to determine the cell survival. TC20 Automated Cell Counter was used.

2.2.3.8 Confocal microscopy and data analysis

Effects of the treatments were directly analysed on the microscopic slides under the microscope (about 50 – 2000 cells) and/or on acquired 3D images (>50 cells). Two replicas of microscopic slides for each sample were evaluated independently. The following equipment was used for confocal microscopy and image acquisition: an automated Leica DM RXA fluorescence microscope (Leica, Wetzlar, Germany) equipped with an oil immersion Plan Fluotar objective (100×/NA1.3) and a CSU 10a Nipkow disc (Yokogawa, Japan); a CoolSnap HQ CCD-camera (Photometrix, Tuscon, AZ, USA); and an Ar/Kr-laser (Innova 70C

Spectrum, Coherent, Santa Clara, CA, USA). Automated exposure, image quality control and other procedures were performed using Acquarium software (Kozubek et al. 2004). The exposure time and the dynamic range of the camera in the red, green and blue channels (R-G-B) were adjusted to the same values for all slides to obtain quantitatively comparable images. Forty serial optical sections were captured at 0.2-µm intervals along the z-axis.

2.2.3.9 Chromatin condensation quantification by 2D Fourier transform

In adition to analyses using the intensity profiles from the red, green and blue (R-G-B) channels (R: 53BP1; G: γH2AX; B: TO-PRO3, chromatin - described in part 2.2.3.10), chromatin condensation was also evaluated by the 2D Fourier transform. From a single 2D section (from a 2D projection) of chromatin (blue channel) observed in the confocal microscope, the 2D Fourier transform in polar coordinates was calculated. Results (correlation coefficients) calculated from confocal microscopy data for DMSO+trehalose, DMSO, trehalose, AFP and untreated were used as criterion for chromatin condensation (sufficiently strong and sharp middle frequency component of the signal).

2.2.3.10 Quantification of DSB induction, changes in higher-order chromatin structure and nuclear envelope integrity

The presence and number of γH2AX/53BP1 foci and other γH2AX signals, as well as co-localization of γH2AX and 53BP1 in the nuclei, was determined visually. Changes in higher-order chromatin structure (condensation) after a freeze/thaw cycle were quantified using the intensity profiles from the red, green and blue (R-G-B) channels (R: 53BP1; G: γH2AX; B: TO-PRO3, chromatin) using the 'RGB Profile Plot' plugin for ImageJ 1.47v software (Schneider et al. 2012) in addition to visual inspection of 3D microscopic images of nuclei and their confocal slices in all three planes. Intensity profiles along line segments demarcated over 0.2-µm thick confocal slices of nuclei were determined separately for the R-G-B channels. Each line segment was designed to cover a substantial part of the nucleus and to include nuclear areas showing maximum and minimum chromatin staining. Sharp changes in high amplitude chromatin staining intensity along the line segment indicate

structurally and functionally distinct chromatin domains that are well preserved after the freeze/thaw procedure.

By contrast, the absence of these changes in chromatin intensity along the line segment (i.e., only slight and slow changes) indicates extensive erosion in the higher-order chromatin structure. Intensive G-peaks (γH2AX) that co-localized with R-peaks (53BP1) mark DSBs. A continuous γH2AX signal that is more constant in intensity and that is not accompanied by a 53BP1 signal indicates apoptotic/necrotic DNA damage. Evaluation of the shape of cell nuclei (maximum area, roundness factor) was determined using the 'selection' and 'analysis' tools in Adobe Photoshop CS6. Narrowing or disruptions in the nuclear lamina, as visualized using a lamin A/C antibody, plus chromatin (TO-PRO3) leakage out of the nucleus was interpreted as indicating damage to the nuclear envelope.

2.2.3.11 Formation of medium with different osmolarities and cells treatments

All procedures have been described in (Falk et al. 2008). The osmolarity of standard culture medium is 290 mOsm. To induce reversible artificial chromatin condensation, the cells were incubated for 12 min in hyperosmotic (570 mOsm) medium. Hyperosmotic (hypertonic) medium was prepared by addition of 1 ml 20 × PBS (2.8 M NaCl, 54 mM KCl, 130 mM Na_2PO_4, 30 mM KH_2PO_4, pH 7.4) to 19 ml DMEM containing 10% FCS. Hypocondensed chromatin in cells was obtained by cell treatment (12 min) in hypoosmotic (hypotonic) medium. Hypoosmotic medium of about 140 mOsm was obtained by diluting standard DMEM medium with an equal quantity of sterile ddH2O. Since chromatin condensation and decondensation started within seconds, washing in physiological salt solution before cell fixation (immuno-fluorescence microscopy) was strictly avoided. For flow cytometry analyses of cell viability, a post-treatment (hypertonic or hypotonic) cultivation of cells in normal (isotonic) medium (30 min or 24 h) was added to allow cell recovery and/or apoptosis induction. Up to about 15 min the hyperosmotic/hypoosmotic treatment has no/minor effect on cell viability and all changes in chromatin structure and cellular processes were reversible.

2.2.3.12 Cells preparation for DART-Orbitrap and LC-MS/MS analyses and DESI

Twenty-four hours prior to the measurements, the cells in culture flasks were provided with fresh DMEM medium (37°C, pH 7.1) supplemented with 100 mM or 200 mM trehalose (Sigma). Consequently, the cells were thoroughly washed (4 × 1 min) in fresh DMEM without trehalose (as proved by LC-MS/MS), harvested by scratching, resuspended in 1 mL of DMEM (1xPBS for DESI), disintegrated by shaking with glass bead tubes 0.5 mm (MO BIO Laboratories, Carlsbad, CA), with microtube homogenizer (BeadBugTM microtube homogenizer D 1030-E, Benchmark Scientific, Edison, NJ), 3 min, 4000 rpm, all extracts were centrifuged (6000 rpm/15 min, HERMLE Z326K, Germany) to remove cells debris and glass pellets, and 100× diluted for the measurements.

Filtered (Nylon filter Mini-UniPrepTM 0.45 µm pore size, Whatman, UK) cell supernatants were used for DART and LC-MS/MS. For DESI-MS the cells were cultivated the same way as for DART. Cell culture was rinsed and centrifuged. The pellet was loaded onto a nylon membrane Nylon 66, 0.2 µm (Supelco, Bellefonte, PA). 2 µL of cell suspense were loaded using the MICROMAN pipette (Gilson, Villiers-le-Bel, France). Nylon membrane was fixed to the glass slides (Prosolia, Indianopolis, IN) by the means of double-site tape.

2.2.3.13 DART-Orbitrap analysis

DART-Standardized Voltage and Pressure Adjustable ion source with tweezer holder module (IonSense, Saugus, MA) was coupled to Orbitrap Elite mass spectrometer (Thermo Fischer Scientific, Bremen, Germany) through the interface evacuated by the diaphragm pump. The DART ion source was operated in the negative ion mode with helium ionizing gas at the pressure 0.55 MPa. The beam was heated to 400°C, the grid electrode voltage was set to 350 V. The parameters of the mass spectrometer were tuned as follows: capillary voltage 50 V, tube lens voltage 100 V, skimmer voltage 18 V and capillary temperature 300°C. The acquisition rate was set to 2 spectra/s with mass resolving power of 120,000 FWHM. All DART mass spectra were acquired over a mass range of *m/z* 50-600. Xcalibur software (Thermo Fischer Scientific, Germany) with DART web-based module was used for the instrument operation, data acquisition and processing.

2.2.3.14 LC-MS/MS

An Agilent 1200 Series Rapid Resolution LC System (Agilent Technologies, Waldbronn, Germany) consisted of an on-line degasser, a binary pump, a high performance SL autosampler, a thermostated column compartment, a photodiode array UV-vis detector. The system was coupled on-line to an MS detector Agilent Technologies 6460 Triple Quadrupole LC/MS with Agilent Jet Stream. MassHunter (Agilent Technologies, Germany) software was used for the instrument operation, data acquisition and processing. The Unison UK-Amino 250 mm x 3.0 mm, 3µm particle size (Imtakt, Portland, OR) for trehalose separation under isocratic elution was used.

The mobile phase consisted of 70% (acetonitrile) and 30% (0.1% acetic acid v/v). The flow rate was 0.7 mL/min and column temperature was 60° C. The column effluent was directly introduced into triple quadrupole mass detector operated in a negative electrospray ionization mode. Samples were analyzed by fast chromatography-MS/MS in the multiple reaction monitoring mode to maximize sensitivity. Characteristic transition for trehalose was *m/z* 341→89.

2.2.3.15 DESI-MS imaging experiments

DESI imaging analysis was performed using a Orbitrap Elite (Thermo Fischer Scientific, Bremen, Germany) with a DESI-2D ion source (Prosolia, Indianopolis, IN). Imaging experiments were performed by continuously scanning the surface in the x-direction and stepping in the y-direction (moving opposite to the direction of the spray) at the end of each line. The DESI ion source geometry was as follows: sprayer-to-sample surface distance of 0.5-1.0 mm, sprayer-to-MS inlet distance of 1.0-1.5 mm, spray impact angle of 58° was used, and collection angle of 10°. Solvent MeOH was sprayed at flow rate 3 µL/min in conventional DESI imaging. Typically, a cells slice (10 × 6 mm) was imaged using 55 lines and step size of 100 µm in the y-direction.

The lines were scanned at a constant velocity of 72 µm/s. Full scan mass spectra were acquired in negative ion mode over the range of *m/z* 50–450. The total time to record this image was 63 min. BioMap software was used to process

the mass spectral data to generate two-dimensional ion images. The optimized MS instrumental parameters used were 6 bar nebulizer (N_2) pressure, 380°C heated capillary temperature, 4 kV spray voltage, 60 V tube lens voltage. The ion injection time was 800 ms, and one microscans were averaged for each pixel in the images. DESI-MSI analysis was performed in negative ion mode for trehalose (*m/z* 341.108).

2.2.3.16 Statistical analyses

The results were analysed statistically using the Kruskal-Wallis One Way Analysis of Variance on Ranks with p=<0.05 considered as statistically significant. Positive cases were re-evaluated by the Mann-Whitney Rank Sum test.

3 Results

3.1 Impact of studied cryoprotectants on their solutions‘ freezing process

3.1.1 Molecular simulations

Liquid water is dynamic and, at its interface with other molecules or at exposed surfaces, H-bonds constantly break and re-form. At the freezing temperature, water resists the breaking of H-bonds and the molecules lock together in a lattice-like symmetry – ice is formed, which is less dense than liquid water. Our calculations showed that the studied cryoprotectants in water influenced the water dynamics (hydrogen bond lifetime). The calculated lifetimes of water/water hydrogen bonds characterized the long-range effect of cryoprotectants on the bulk water dynamics and subsequently crystallization process (**Tab. 3.1.1.1**). The short-range effect of the cryoprotectant on the water in the first solvation shell was described by the value of the hydrogen bond lifetime between the cryoprotectant molecule and water (Verde and Campen 2011) (**Tab. 3.1.1.1**). DMSO affected the largest (of all studied cryoprotectants) amount of water molecules in the solution. In addition, water molecules near the methyl groups of a DMSO molecule cannot form an alternative H-bond, which changes both their interactions with other water molecules and ice formation (Luzar and Chandler 1993). DMSO also affected the water dynamics due to the relatively large negative charge of the oxygen atom (greater than the charge on oxygens in trehalose or in water) increasing the strength of the H-bond with water. Adding 3.2% (w/w) trehalose to 10% (w/w) DMSO water solution did not significantly change the water/water and DMSO/water hydrogen bond lifetimes (compared to 10% (w/w) DMSO).

The hydrogen bond lifetime calculated for AFP/water was longer than the lifetime for DMSO/water and trehalose/water. The reduction of surrounding water mobility when AFP is present may be related to the large size of the AFP molecule and its ice-binding surface containing regularly spaced hydroxyl groups(Liou et al. 2000). The AFP does not significantly influence free water but strongly influences the solvation shell around it. This corroborates the assumption that AFP can bind to the surface of ice crystals and inhibit their growth.

Table 3.1.1.1. Hydrogen bond lifetimes (τ_{HB}) between water/water molecules and cryoprotectant/water molecules calculated at 25 °C and at -8 °C for the tested solutions (Kratochvilova et al. 2017).

Samples used in the hydrogen bond lifetime calculations	τ_{HB} (ps) at 25 °C	τ_{HB} (ps) at -8 °C
Water		
Water/water	3.02	7.93
ApAFP752 in water		
ApAFP752/water	16.90	50.64
Surrounding water/water	3.02	7.95
Trehalose in water		
Trehalose/water	4.92	15.16
Surrounding water/water	3.12	8.08
DMSO in water		
DMSO/water	5.36	13.39
Surrounding water/water	3.71	10.14
Trehalose and DMSO in water		
Trehalose/water	6.81	21.41
DMSO/water	5.19	13.45
Surrounding water/water	3.76	10.34

Molecular simulations of the studied cryoprotective solutions showed that while DMSO molecules spread evenly throughout the aqueous solution, trehalose molecules tend to aggregate and form clusters (**Fig. 3.1.1.1**).

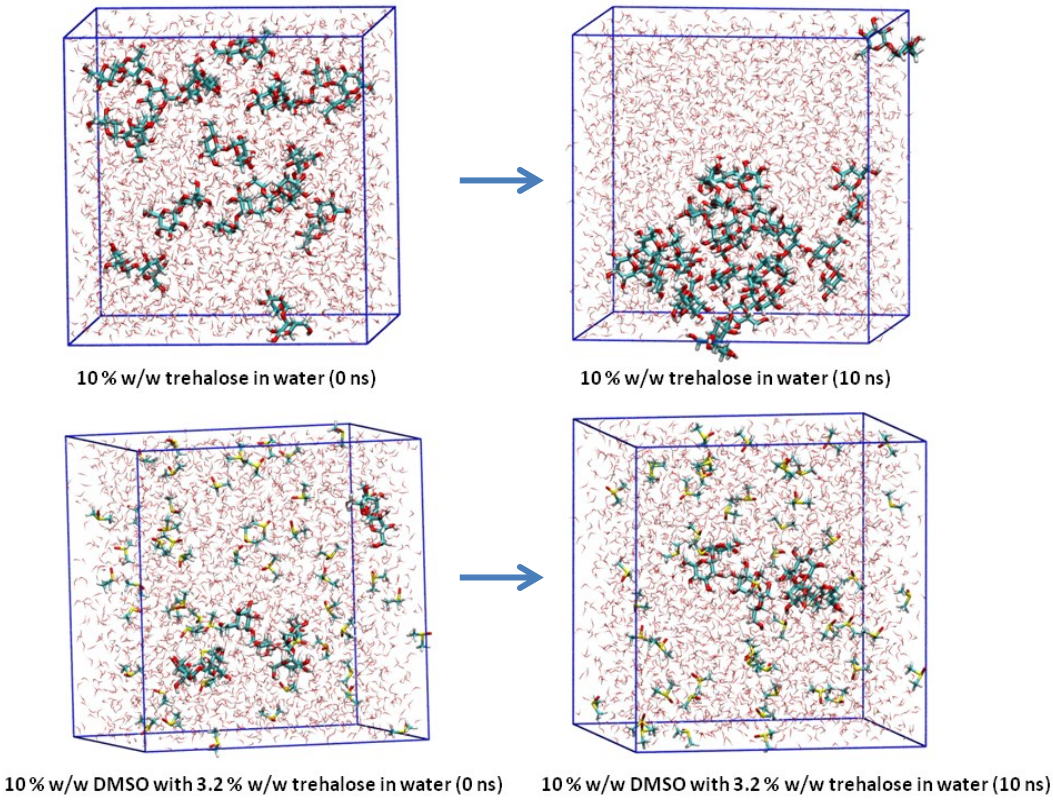

Fig. 3.1.1.1. 10% (w/w) trehalose in the solvation box (top), and 10% (w/w) DMSO with 3.2% (w/w) trehalose in the solvation box (bottom). The start (0 ns) of the molecular dynamics simulation is on the left, and the end (10 ns) of the molecular dynamics simulation is on the right. The simulations were performed at room temperature. (Kratochvilova et al. 2017)

This behaviour can be further understood by computing interaction energies between various pairs of molecules of water, DMSO and trehalose (**Fig. 3.1.1.2, Tab. 3.1.1.2**).

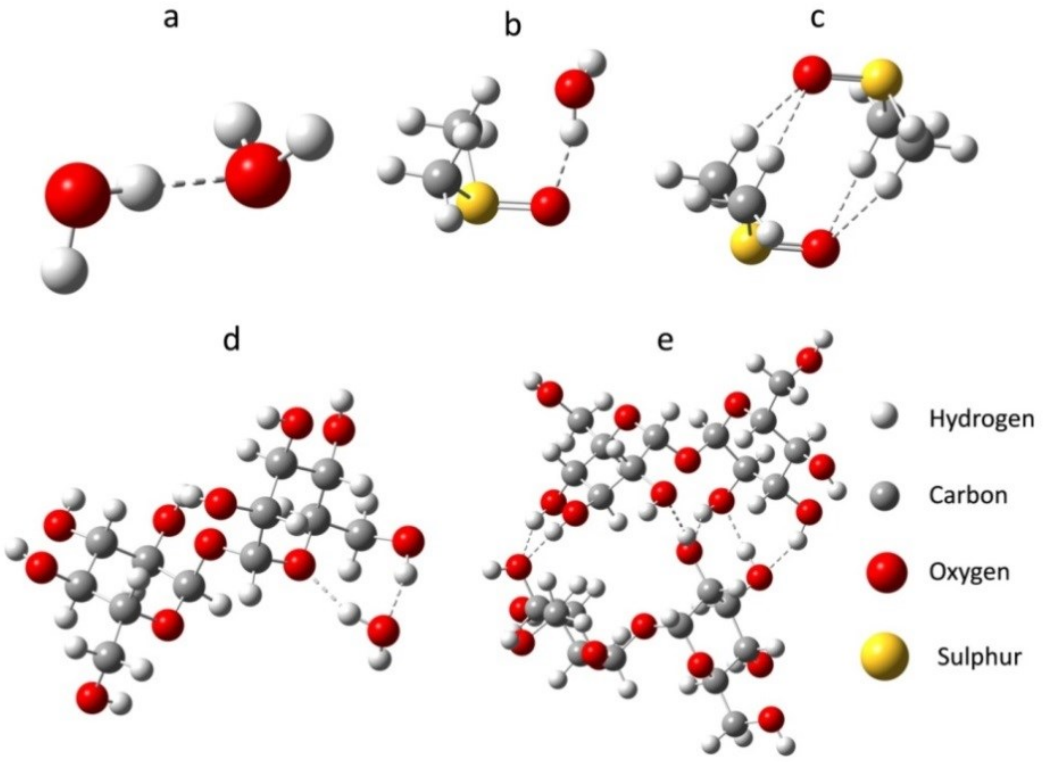

Fig. 3.1.1.2. The geometry-optimized structures; a) water dimer, b) DMSO/water system, c) DMSO dimer, d) trehalose/water system, e) trehalose dimer. Dashed line indicates inter-noncovalent interactions.

Table 3.1.1.2. Interaction energies of pairs of cryoprotectant molecules calculated using DFT

Sample	**Interaction energies [kcal/mol]**
Trehalose/water	-6.2
DMSO/water	-5.9
Water/water	-3.9
DMSO/DMSO	-5.5
Trehalose/trehalose	-7.0

It can be seen that the trehalose/trehalose interaction is more energetically favorable than trehalose/water, hence the clustering. This result is largely caused by the hydrogen bonds that easily form between the hydroxyl groups of two trehalose molecules. DMSO, on the other hand, interacts strongly with water (DMSO/water noncovalently bound dimer has lower interaction energy that water/water and DMSO/DMSO), which is likely responsible for the homogenous spreading of DMSO in an aqueous solution.

Finally, dipole moments of the cryoprotectant molecules were also calculated (also using DFT). The dipole moment of DMSO is rather high, which is due to the strong negative charge of its oxygen atom and strong positive charge of its sulphur atom. Considering the high permittivity of water, the magnitude of DMSO's dipole moment may be relevant to the way DMSO affects the freezing of water.

3.1.2 Differential scanning calorimetry

DSC curves of deionized water, AFP solution, aqueous solutions of trehalose and mixture of DMSO with trehalose were measured (melting points: **Tab. 3.1.2.1**, selected DSC curves**: Figs. 3.1.2.1, 3.1.2.2)**. In all studied cryoprotectant-containing solutions, the melting/freezing points were shifted to lower values (compared to deionized (pure) water/ice). The greatest shift of the melting/freezing point (related to the concentration of cryoprotectant in the solution) was observed in 10% DMSO containing solutions. This correlates with change in the DMSO solution crystallinity (XRD). The glass phase transition temperature for the trehalose/water solution was found to be T_1= –38°C. When the concentration of trehalose in the solution was lowered, the glass phase transition temperature was maintained around –38°C. In accordance with the results of Raman spectroscopy, the eutectic phase transition was also observed by DSC in PBS solutions (–23 and –31 ^{o}C) and ApAFP752 solution (–22 and –27 ^{o}C).

Table 3.1.2.1. Melting temperatures measured by DSC

Sample	T_m [°C]
DI water	0
AFP solution	0
100 mM (3.2% w/w) trehalose + DI water	-1
10% w/w DMSO + 100 mM (3.2% w/w) trehalose + DI water	-10
10% w/w DMSO + DI water	-10
41% w/w trehalose + DI water	-13
15% w/w trehalose + DI water	-3

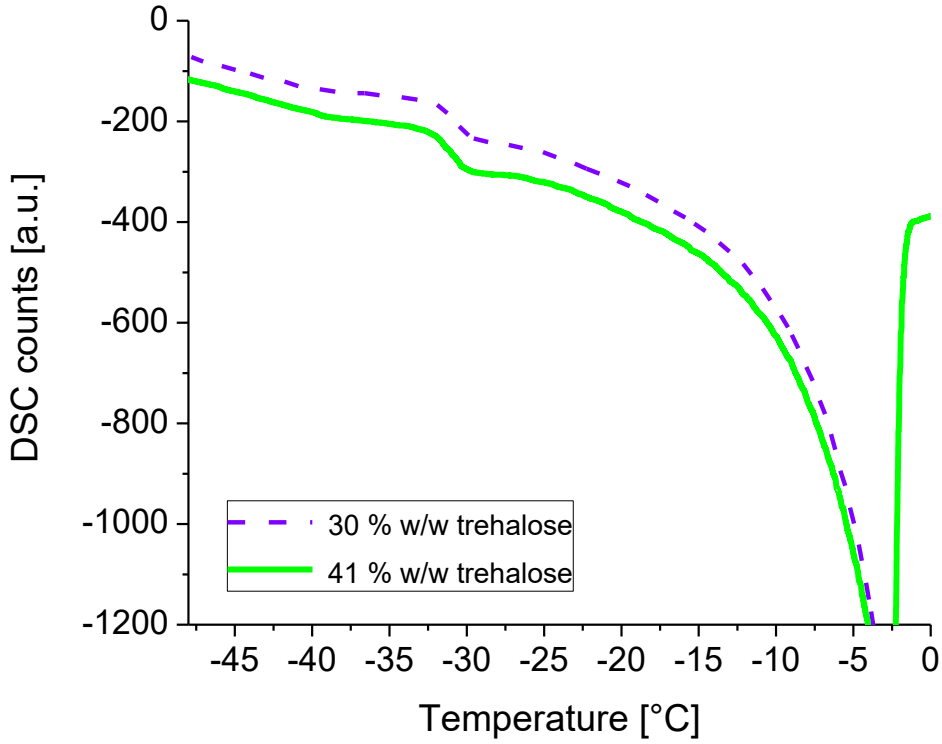

Fig. 3.1.2.1. Melting points and glass phase transition temperatures of 41% w/w and 30% w/w of trehalose solutions.

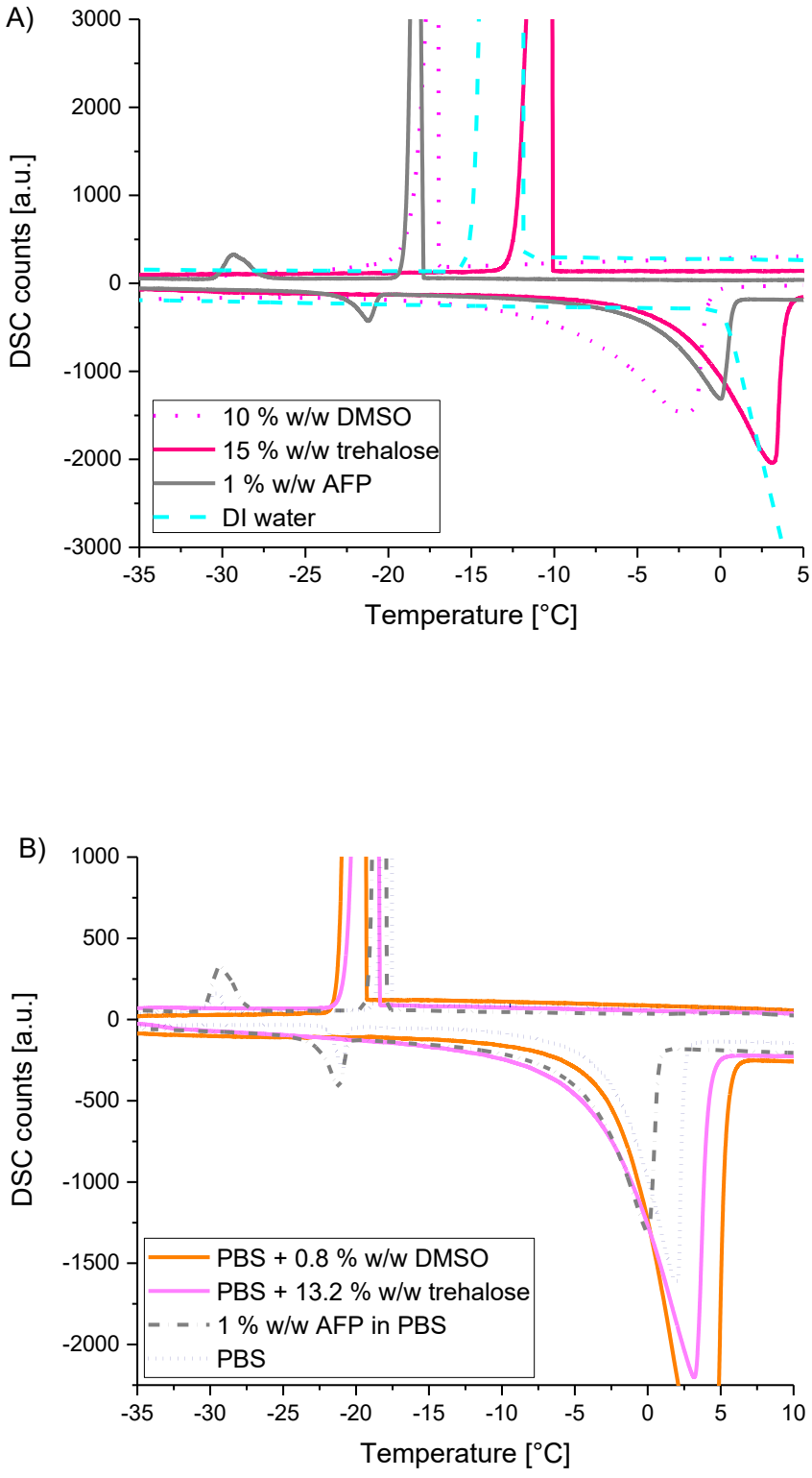

Fig. 3.1.2.2. DSC curves of DMSO, trehalose and AFP solutions A) in DI water, B) in PBS.

3.1.3 X-ray diffraction

X-ray diffraction measurements were performed on frozen samples, and the crystal angular distribution was measured and compared for the studied materials. Pure water had just a few very large crystals and the strongest diffraction intensity. An aqueous trehalose (41% w/w) solution showed crystal aggregates with similar orientations. This indicated that a crystal has grown on one nucleus and that the growth was accompanied by precipitation of another phase, leading to curved crystals with needle/platelet/dendrite shapes. Trehalose in solution supports such aggregation of crystals in frozen samples. The rest of the samples, which contained AFP, DMSO and DMSO+trehalose, showed random crystal nucleation and growth. **Fig. 3.1.3.2a** shows histograms counting the data-points whose diffraction intensities lay in the particular ranges for each of the plots from **Fig. 3.1.3.1** (from top to bottom correspondingly). Using a deconvolution procedure, equivalent histograms of distribution of Gaussian peaks with maximum intensity in particular ranges are shown in **Fig. 3.1.3.2b**. In all cases except for pure water, the results showed a decrease in the distribution for the strongest observed peaks (greatest *x*--values), which means that the distribution median lay in the range of smaller crystallites than would correspond to the maximum on the *x*-scale.

According to the kinematical theory of X-ray diffraction, the diffraction intensity of crystallites is proportional to their volume. The linear dimension (diameter) of the ice crystals, being roughly the third root of the diffracting volume, was the greatest for frozen pure water (10 times bigger than ice crystals in frozen 41% trehalose solutions). Judging from the shift of the slope, the ice crystal sizes in 10% (w/w) DMSO-frozen solutions were about half the size of those in 41% trehalose frozen solutions. Higher concentration of AFP, 1% (w/w), led to at least one order of magnitude decrease in the diffracting volume of crystals compared to 0.1% (w/w) AFP and 41% trehalose solutions. All the AFP solutions XRD measurements were compared with XRD on frozen phosphate + NaCl in DI water solutions of the same concentrations. AFP in all cases had important impact on frozen solutions constitution.

During melting, the crystals in the samples containing high concentrations of trehalose decreased with rising temperature. The distribution of crystal volumes even exhibited a shift to smaller values at around -30°C (**Fig. 3.1.3.5**), which may correspond to the secondary phase transition visible in **Fig. 3.1.2.1**. In DMSO-containing frozen solutions, signal from larger crystals gradually grows at the expense of the smaller ones, which suggests that the larger crystals grow and smaller crystals diminish. In other words, this is a sign of the ice recrystallization process (**Fig. 3.1.3.7**). When 3.2% trehalose is present in the 10% DMSO solution, the recrystallization is suppressed (**Fig. 3.1.3.8**). This may be also responsible for the slight increase in post-thaw cell viability when trehalose is added to the 10% DMSO cryopreservation solution (**Fig. 3.2.1.1**). On the other hand, the crystalline structure of the AFP-containing solution didn't undergo a significant change during warming, which suggests that AFP can act as an ice-recrystallization inhibitor (**Fig. 3.1.3.4**). The complete set of frozen solutions monitored by XRD during warming is in **Figs. 3.1.3.3-8** (Kratochvilova et al. 2017).

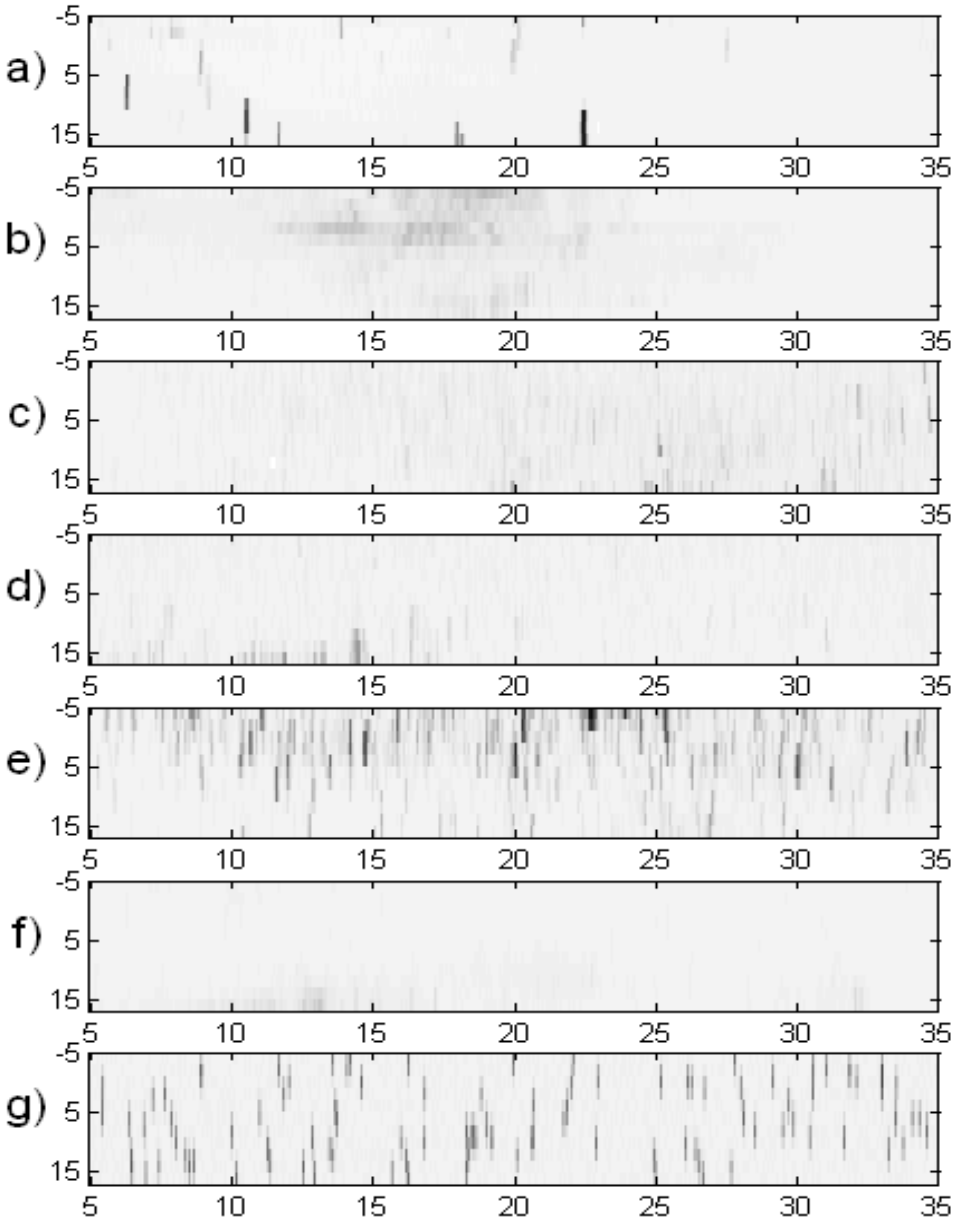

Fig. 3.1.3.1 Diffraction intensity maps in angular coordinates. A comparison of frozen specimens of (**a**) water, (**b**) 41% (w/w) trehalose, (**c**) 10% (w/w) DMSO, (**d**) 10% (w/w) DMSO + 3.2% (w/w) trehalose, (**e**) 0.1% (w/w) AFP, (**f**) 1% (w/w) AFP, (**g**) simulated peaks. Horizontal axis, angle ω (horizontal tilt); vertical axis, angle χ (vertical inclination); the grey scale is logarithmic and is the same for all plots (Kratochvilova et al. 2017).

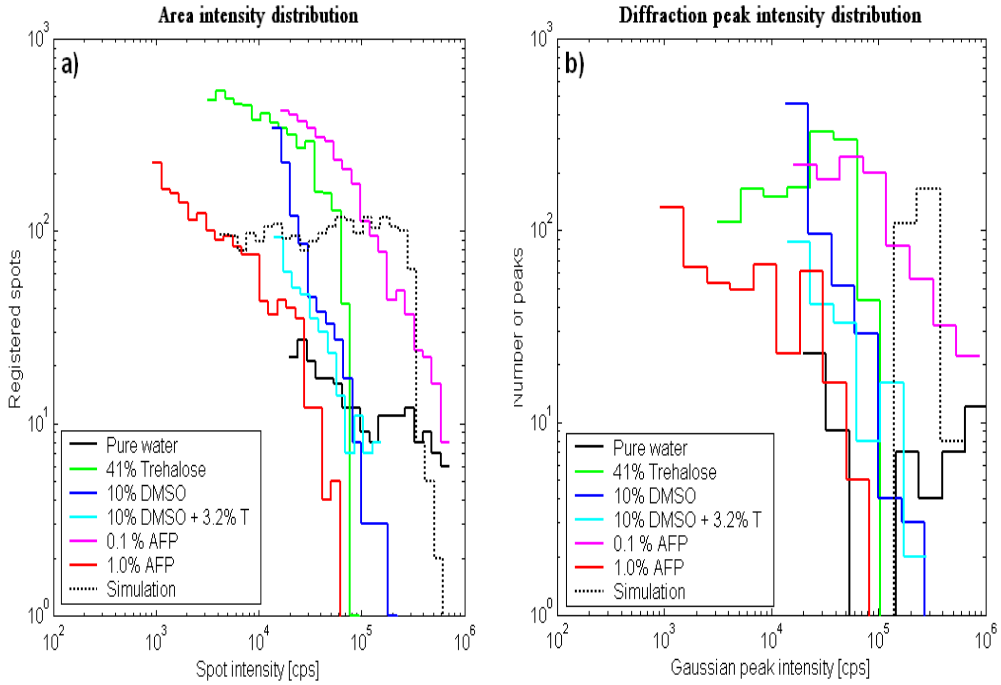

Fig. 3.1.3.2. Histograms of the (a) area intensity distribution (Kratochvilova et al. 2017) **and (b) diffraction peak intensity distribution.** The range (horizontal axis) scales start at intensity levels that are safely over the noise level. The vertical scale is either the number of data points with the specified intensity (**a**) or the number of expected Gaussian peaks with particular maximum intensity (**b**).

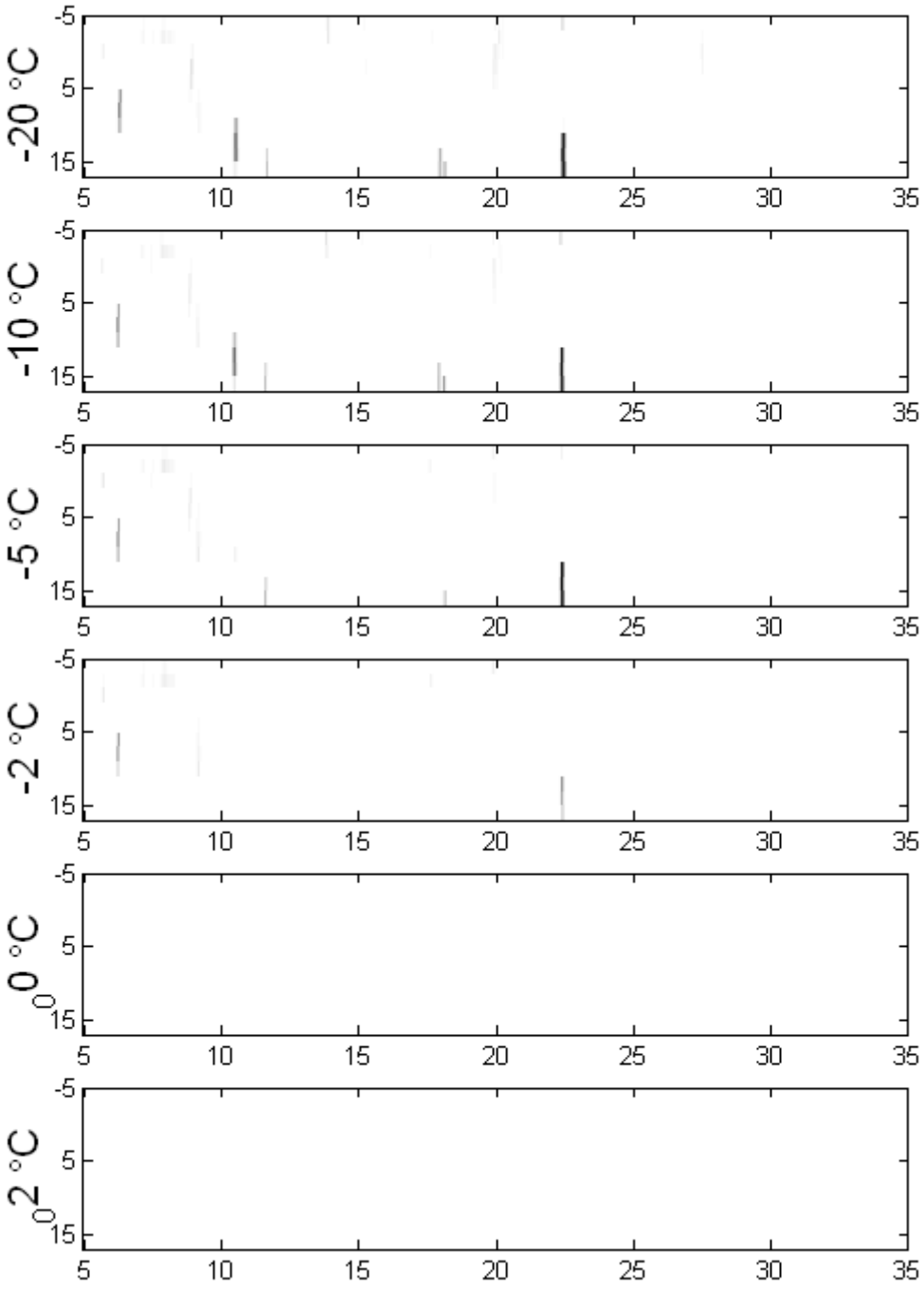

Fig. 3.1.3.3. Diffraction intensity maps in angular coordinates – pure water. The melting process (from top to bottom) of water crystals observed on 110 reflection intensities with various orientations (Kratochvilova et al. 2017).

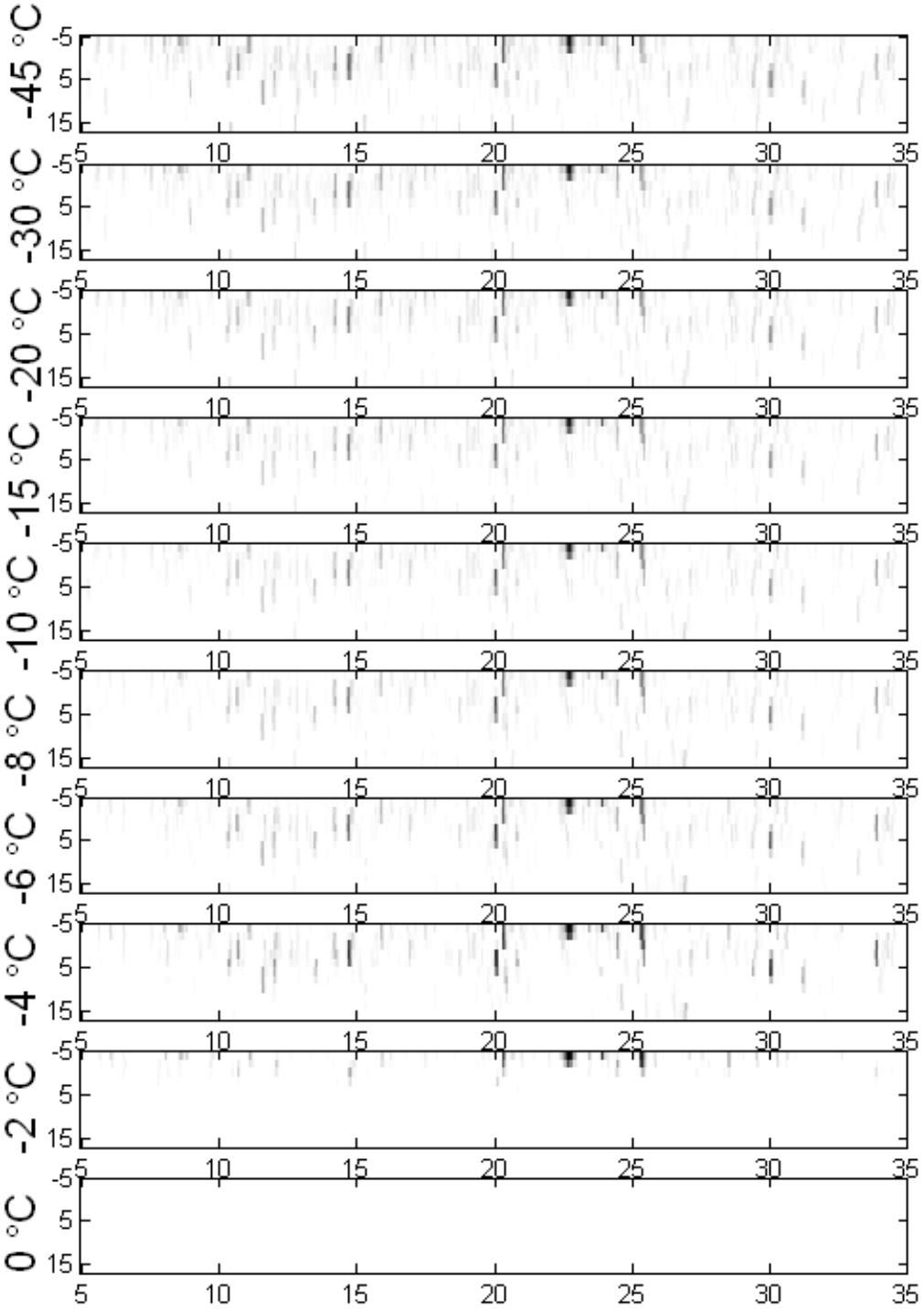

Fig. 3.1.3.4. Diffraction intensity maps in angular coordinates – 0.05% w/w AFP solution. The melting process (from top to bottom) of water crystals observed on 110 reflection intensities with various orientations (Kratochvilova et al. 2017).

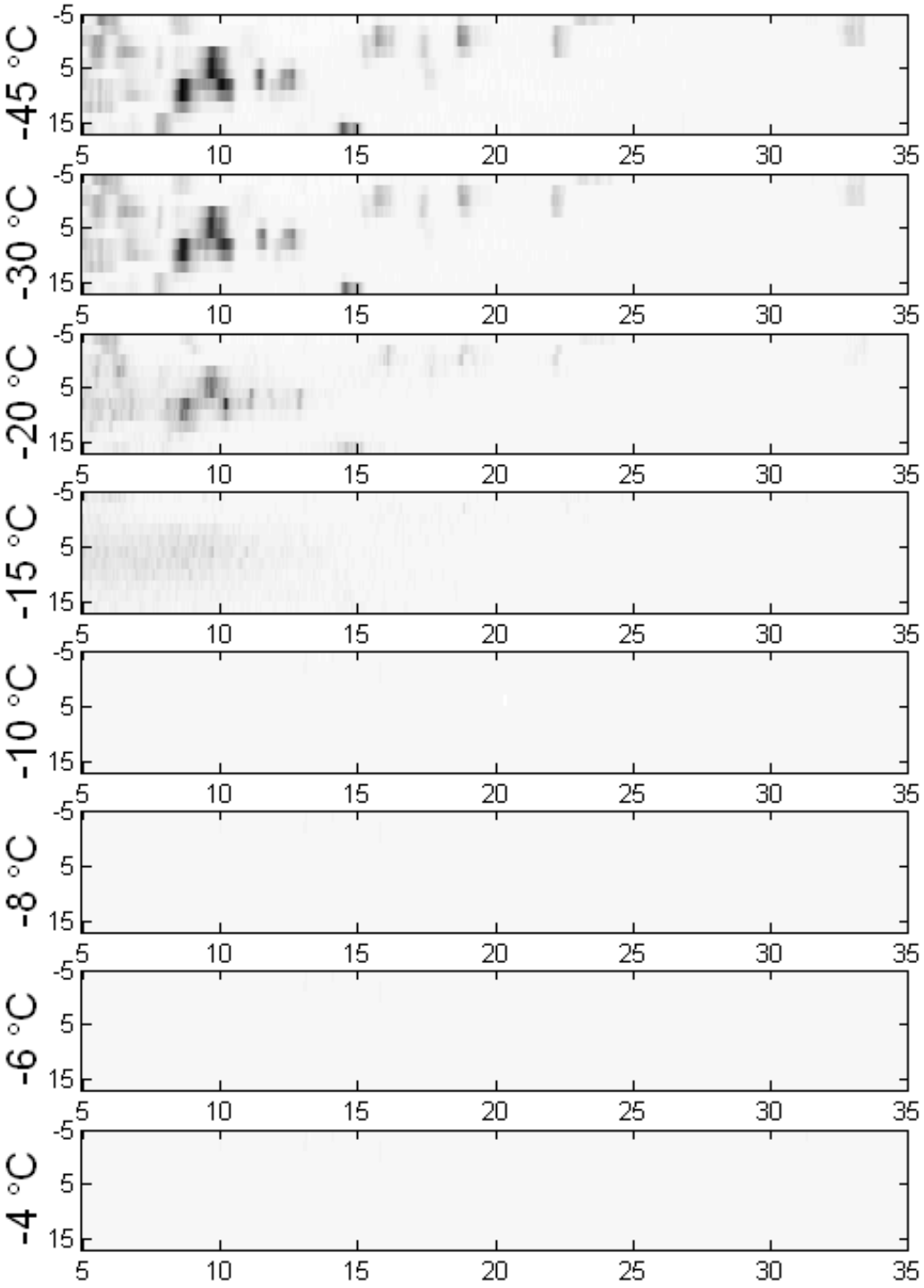

Fig. 3.1.3.5. Diffraction intensity maps in angular coordinates – 41% w/w trehalose solution. The melting process (from top to bottom) of water crystals observed on 110 reflection intensities with various orientations (Kratochvilova et al. 2017).

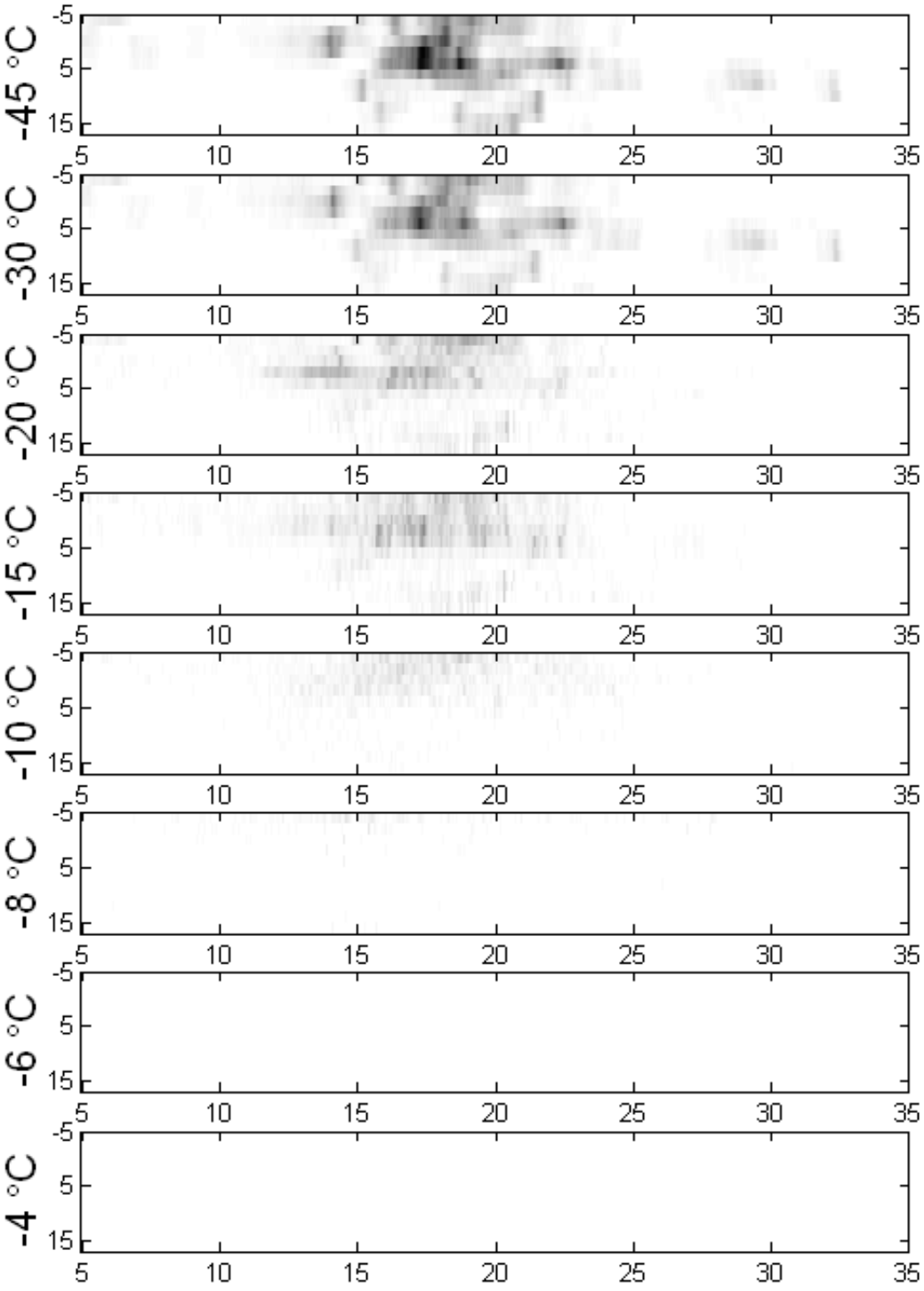

Fig. 3.1.3.6. Diffraction intensity maps in angular coordinates – 41% w/w trehalose + 10% w/w DMSO solution. The melting process (from top to bottom) of water crystals observed on 110 reflection intensities with various orientations (Kratochvilova et al. 2017).

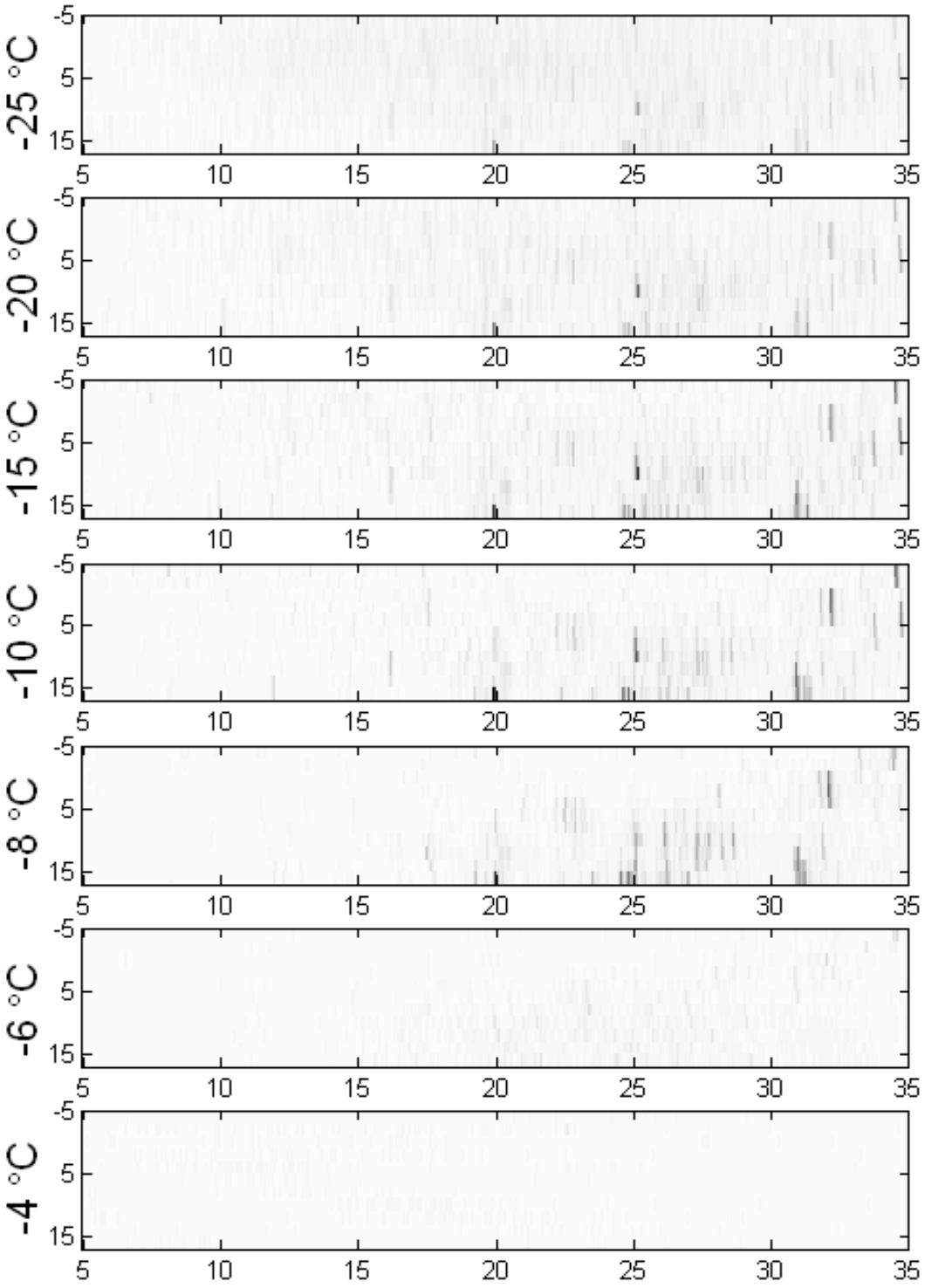

Fig. 3.1.3.7. Diffraction intensity maps in angular coordinates – 10% w/w DMSO solution. The melting process (from top to bottom) of water crystals observed on 110 reflection intensities with various orientations (Kratochvilova et al. 2017).

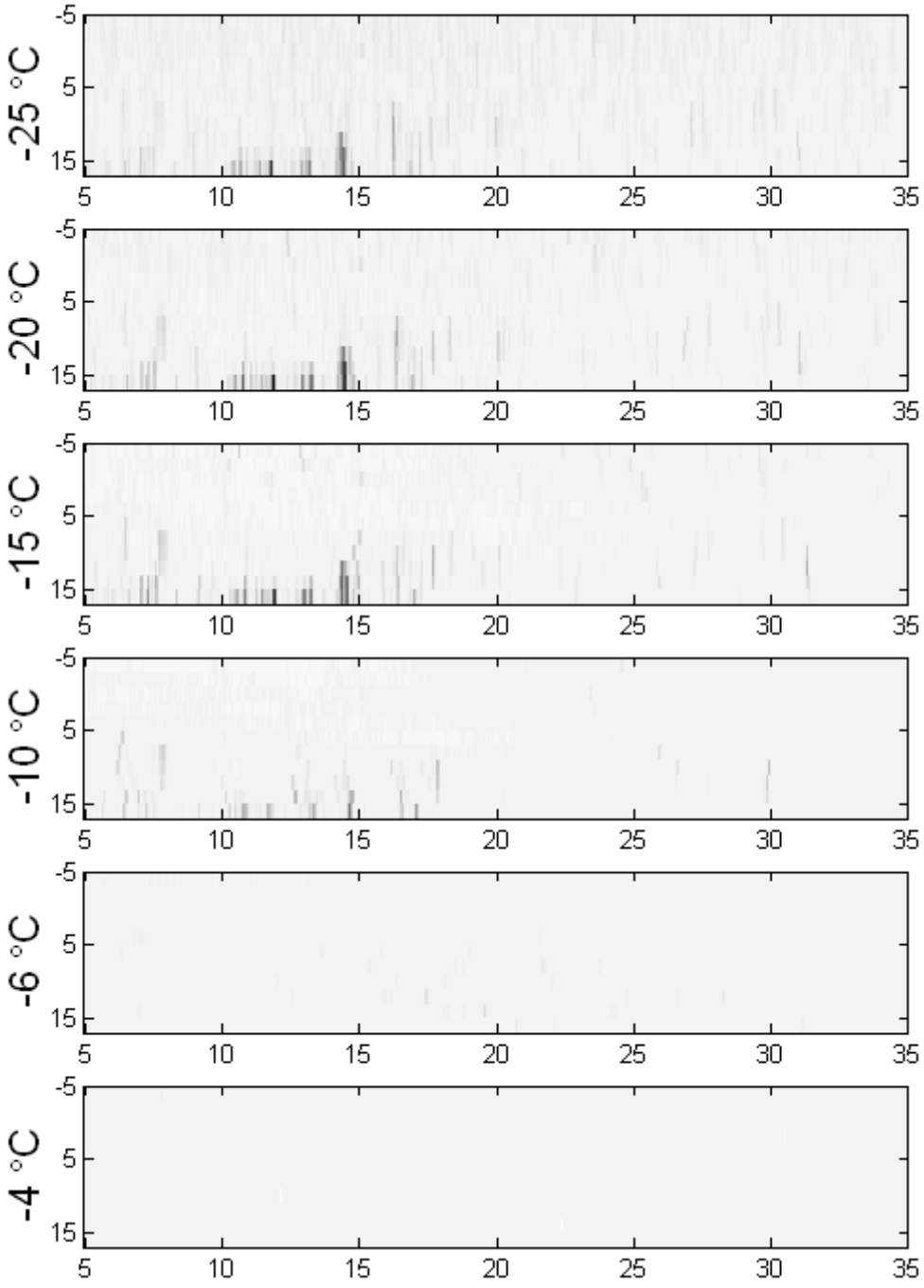

Fig. 3.1.3.8. Diffraction intensity maps in angular coordinates – 10% w/w DMSO + 3.2% w/w trehalose solution. The melting process (from top to bottom) of water crystals observed on 110 reflection intensities with various orientations (Kratochvilova et al. 2017).

3.1.4 Raman spectroscopy

Analysis of Raman spectra can reveal chemical composition of the sample as well as interactions of its constituents. **Fig. 3.1.4.1** shows spectra of cryoprotective samples frozen at -170°C (exact compositions are in **Tab. 2.1.5.1**). For each sample, multiple spectra were measured, and the spectra shown are those that exhibit all the observed spectral features of a given specimen and are thus characteristic of it.

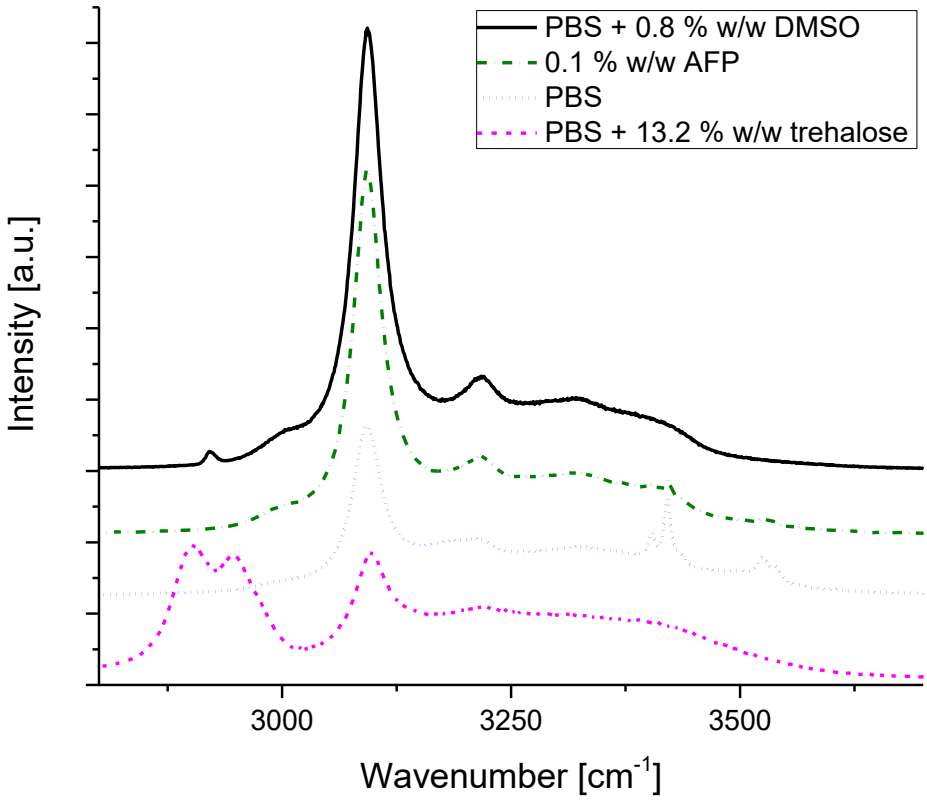

Fig. 3.1.4.1. Raman spectra of AFP, PBS, trehalose in PBS and DMSO in PBS solutions, measured at –170°C. In the spectra of PBS and AFP solutions, the hydrohalite bands at 3421 cm^{-1} and 3537 cm^{-1} can be seen.

The presence of PBS in the sample can lead to additional formation of a distinct band at 3421 cm^{-1} and a secondary band at 3537 cm^{-1}. This is a sign of the presence of so-called eutectic phase, a mixture of ice and crystalline NaCl hydrate (hydrohalite). Addition of DMSO and trehalose at given concentrations causes the

eutectic bands to disappear. It is therefore likely that DMSO and trehalose prevent water from forming a eutectic mixture with other substances present (such as NaCl). This is in line with them affecting the whole volume of the sample, unlike the AFP whose molecules adsorb to ice crystal surfaces during the onset of freezing.

3.2 Cryopreserved Cells State

In the second major section of our work, we studied the state of cryopreserved cells, focusing firstly on the mechanical properties of their surface and body (using AFM), and secondly on the damage suffered by their nuclei (nuclear membrane deformation and rupture, change in chromatin condensation, DNA breaks) using fluorescence microscopy. Our results were correlated with viability of frozen and thawed cells treated by different cryoprotectants. The most significant findings are related to the changes on the level of chromatin and the DNA.

3.2.1 Cryopreserved cells viability

Incubation of cells with cryoprotectants had only minor impact on cell viability after 24 hours. On the other hand, viability of the frozen/thawed cells (24 h after freezing) depended strongly on the used cryoprotectant (**Fig. 3.2.1.1**). For precise composition of the cryoprotective solutions, see **Tab. 2.2.1.1.** Without cryoprotectants, almost all frozen cells died after being thawed; only 7% survived 24 h post-thawing. The highest cryoprotective effect was brought about by DMSO (81% survival 24 h post-thawing), especially when it was combined with trehalose (trehalose for 24 h followed by DMSO for 2 min); in that case, about 86% of cells survived 24 h after thawing. The improvement of cell viability by trehalose only (24 h-incubation) was also relatively large: 59% of cells survived 24 h after thawing. However, the cryoprotective effect of trehalose strongly depended on the incubation time and was only observable for incubations ≥24 h (4 h and 6 h incubations had no effect). AFP exerted the smallest effect among the cryoprotectants studied with only 32% cell survival.

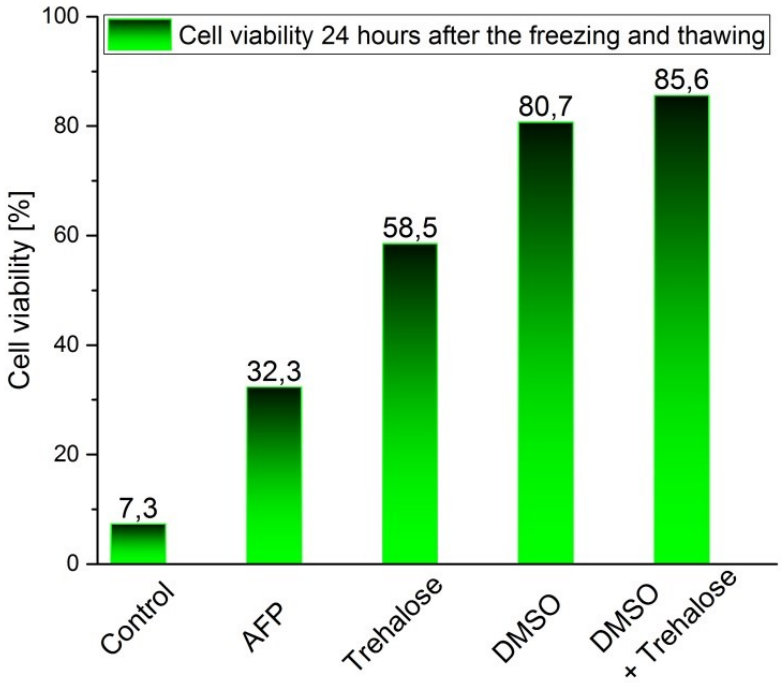

Fig. 3.2.1.1. Cell viability measured 24 h after freezing/thawing by flow cytometry (Annexin V/7-AAD staining) (Kratochvilova et al. 2017).

3.2.2 Mechanical properties of cryopreserved cells

AFM microscopy allowed us to evaluate elastic properties of cryopreserved cells in different cell parts and at different times after thawing. First, we measured stiffness of cultured (never frozen) fibroblasts incubated with different cryoprotectants (DMSO and glycerol). Then we measured development of fibroblasts surface stiffness after freezing/thawing. For this case, mitotically inactivated (denoted IR) cells frozen/thawed with DMSO were used as a negative control for which cell stiffness changes are not expected after freezing/thawing (IR frozen/thawed cells were compared to non-IR frozen/thawed cells). Furthermore, we observed differences in distribution and temporal development of cell stiffness depending on the use of a permeating (DMSO) or nonpermeating (PEG-1500) cryoprotectant, respectively. Stiffness as a mechanical property of the cell was characterized here by Young's modulus (a measure of elasticity), as is common in other works (Luo et al. 2016; Radotic et al. 2012).

3.2.2.1 Cryopreserved cells regeneration monitored by atomic force microscopy

To properly interpret the AFM results, we compared various models of the cell surface reaction to AFM tip pressure, specifically the equations containing the material parameter of stiffness – the Young's modulus (YM) - *E*.

We used a pyramidal sharp tip as this indenter shape ensured sufficiently high resolution in horizontal direction, which was necessary for proper description of cryopreserved cells after thawing. In this connection, a number of studies have reported that cell stiffness can be reliably measured using "sharp" probes and that the values obtained are similar to those found with spherical probes, as well as observing no detrimental effects due to persistent probing of individual cells with a pyramidal tip (Gavara 2017; Chiou et al. 2013; Vargas-Pinto et al. 2013).

The advantage of the sharp tip we used is the possibility to simultaneously combine high resolution mapping of the cell topography with measurements of local mechanical and adhesion properties of the cell, without a necessity to change the tips during experiments. For a given amount of applied force, the sharper probes can penetrate deeper into the probed sample, which was important for our purposes.

In order to select the indentation model most suitable for the analysis of our data, we compared a number of models: e.g. Rico's (Rico et al. 2005), Ogden's (Ogden 1972), Fung's (Fung 1967), Maugis' (Maugis 1992) and Bilodeau's (Bilodeau 1992). AtomicJ software was used to apply the indentation models (Hermanowicz et al. 2014). It was the Bilodeau model that gave the best agreement between our data and calculated force-indentation relationship.

When only a small area on the surface of a fibroblast is studied, a lower set point (SP) value (i.e. 0.4 nN) can be used, which allows studying cell stiffness in the membrane and submembrane region. In our measurement, we chose to use set point 0.4 nN because below this value, the signal-to-noise ratio was not satisfactory.

Using a higher SP (1 nN) value and larger area (100x100 μm^2) provides information about the overall cell stiffness (the inner cell structure dynamics). Relative differences in the cell stiffness development between individual cells were less than 6%.

First, we investigated the correlation between the cell membrane stiffness and cell adhesion in never frozen murine embryonic fibroblasts incubated with the DMSO or glycerol (cultured cells). Their stiffness changes were identical for both cryoprotectants (DMSO, glycerol) at the corresponding concentrations within the tested concentration range. The relative stiffness in the presence of 5% DMSO or glycerol decreased to 84% of the initial value. Increasing the concentrations of these cryoprotective compounds in the culture media (i.e., to 10%, 15% and 20%) further decreased the relative stiffness to 70%, below 50% and below 15%, respectively (**Fig. 3.2.2.1.1)**. Such membrane stiffness changes (i.e., decreases in Young's modulus) presumably correspond to change in the cell surface composition caused by DMSO or glycerol. Stiffness maps and height profiles of fibroblasts treated with various percentages of cryoprotectants are shown in **Fig. 3.2.2.1.2**.

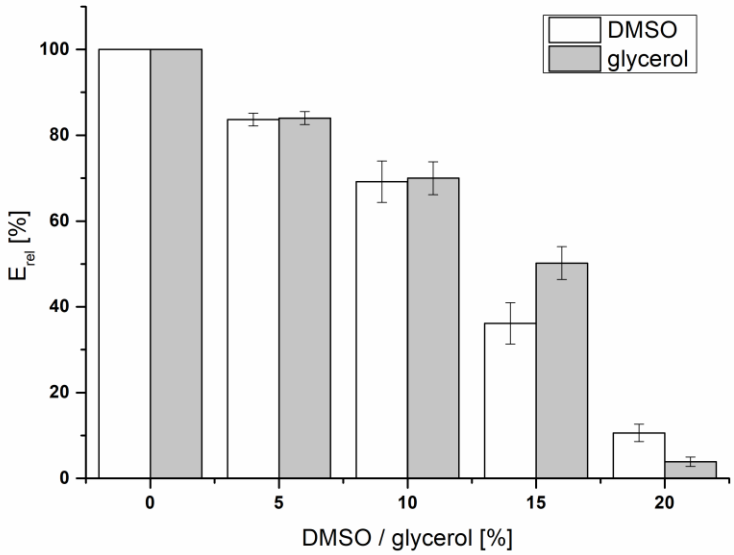

Fig. 3.2.2.1.1. Immediate effects of the cryoprotectant presence (DMSO or glycerol) in the culture media on the relative stiffness of non-frozen and non-IR cells determined by measuring the change in the relative stiffness (relative value of Young's modulus - E_{rel}). Increasing the concentrations of DMSO/glycerol in the culture media further decreased the relative stiffness.

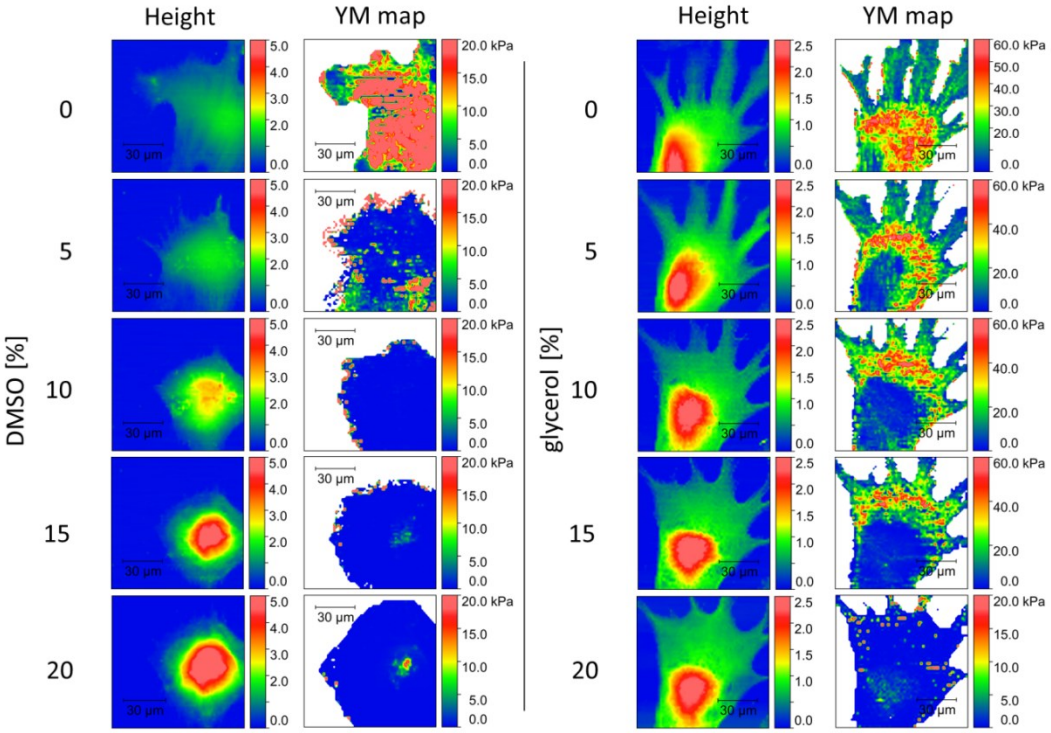

Fig. 3.2.2.1.2. Height profile images and corresponding stiffness maps taken during the force mapping of non-IR fibroblast cells exposed to different concentrations of cryoprotectant compound (left – DMSO, right - glycerol). The concentration of the cryoprotective compound in the culture medium is shown on the left side of both panels, and a high set point (SP) measured height and stiffness maps are presented for each concentration. The displayed area is 100x100 μm^2.

After that we investigated the never frozen cell adhesion properties in the presence of cryoprotectants. It is generally accepted that as the cell adhesion increases, the cell profile height decreases, and the cell surface stiffens because of stretching of the membrane on the surface. We correlated cell height and stiffness maps. The far left column (DMSO Height) in **Fig. 3.2.2.1.2** presents the height maps. The increasing height together with the decreasing stiffness observed in the corresponding Young's modulus map suggests that DMSO-treated cells exhibit lower surface adhesion and that the surface adhesion decreases as the DMSO concentration in the medium increases, causing cells to lose their adhesion and form higher and softer structures.

The glycerol-treated cells, which are shown in the two columns of images on the right side of **Fig. 3.2.2.1.2,** exhibit a decrease in average cell stiffness (i.e., cell surface softening). Glycerol did not induce an increase in the cell height within the tested glycerol concentration range, suggesting that better adhesion of the cells to the surface occurs in the presence of glycerol than in the presence of DMSO.

Next, we mapped the temporal development of frozen/thawed cell stiffness using two distinct values of setpoint and measurement area. High-SP (1 nN) measurements were done on an area of 100x100 μm^2, low-SP (0.4 nN) measurements were performed on an area of 10x10 μm^2.

The 100x100 μm^2 area always contained regions of the plastic substrate, whose stiffness is approximately 2 orders of magnitude higher than that of the cell. Therefore, these regions were filtered out (masked) before the data were further processed. For illustration, **Fig. 3.2.2.1.3b** shows an unmasked and masked (respectively) AFM image. As a result of the masking procedure, the average stiffness decreases from 1.08 MPa to 22.2 kPa.

Small areas **(Fig. 3.2.2.1.3a**, bottom image) were chosen out of the large areas so that they are positioned neither at the cell edge nor over the cell nucleus. The mapping was done under conditions that guarantee that the interaction between the AFM probe and sample surface is not interrupted during the period of the measurement.

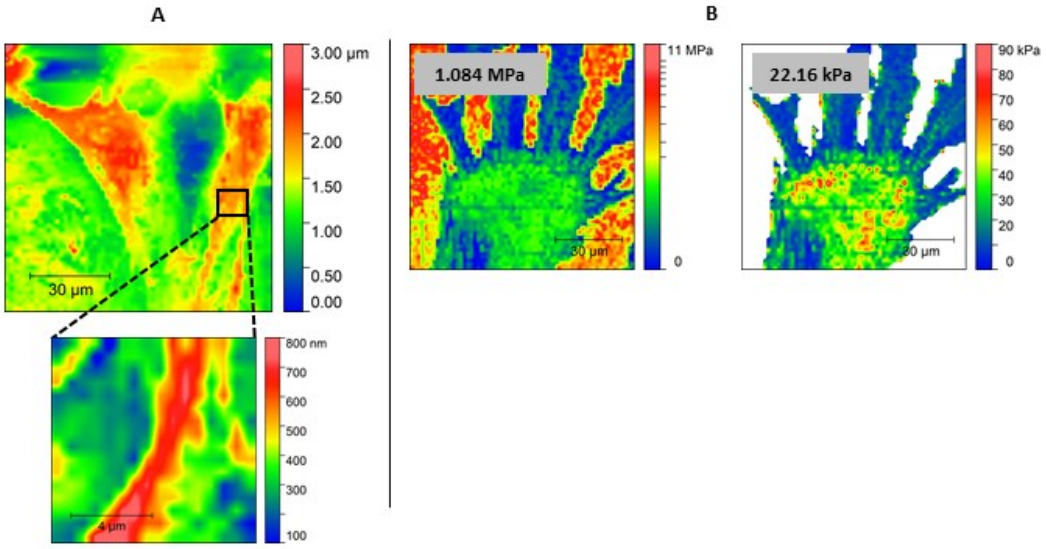

Fig. 3.2.2.1.3. Comparison of large versus small measurement area (A); Demonstration of the effect of the masking on average cell stiffness (B). A) Two approaches were used to study cell stiffness development by AFM in force mapping mode. Large area (100x100 µm^2) containing one or more cells can be monitored by a nano-indentation process when higher SP values are used (upper image). The image below schematically shows the selection of a small area on the cell surface (10x10 µm^2), which enables using a faster nano-indentation process with a low value of the maximum loading force (low-SP). B) The effect of masking the plastic substrate area around the cell. The average value of Young's modulus is shown in each respective image (left - unprocessed map; right - map with masked regions of plastic surface).

When investigating the post-thaw temporal development of fibroblast stiffness and cell height, the results obtained on frozen/thawed fibroblasts were compared to results obtained on the same type of cells that were mitotically inactivated, i.e. irradiated with γ-rays prior to freezing/thawing (denoted IR cells/fibroblasts) (**Scheme 3.2.2.1.1**).

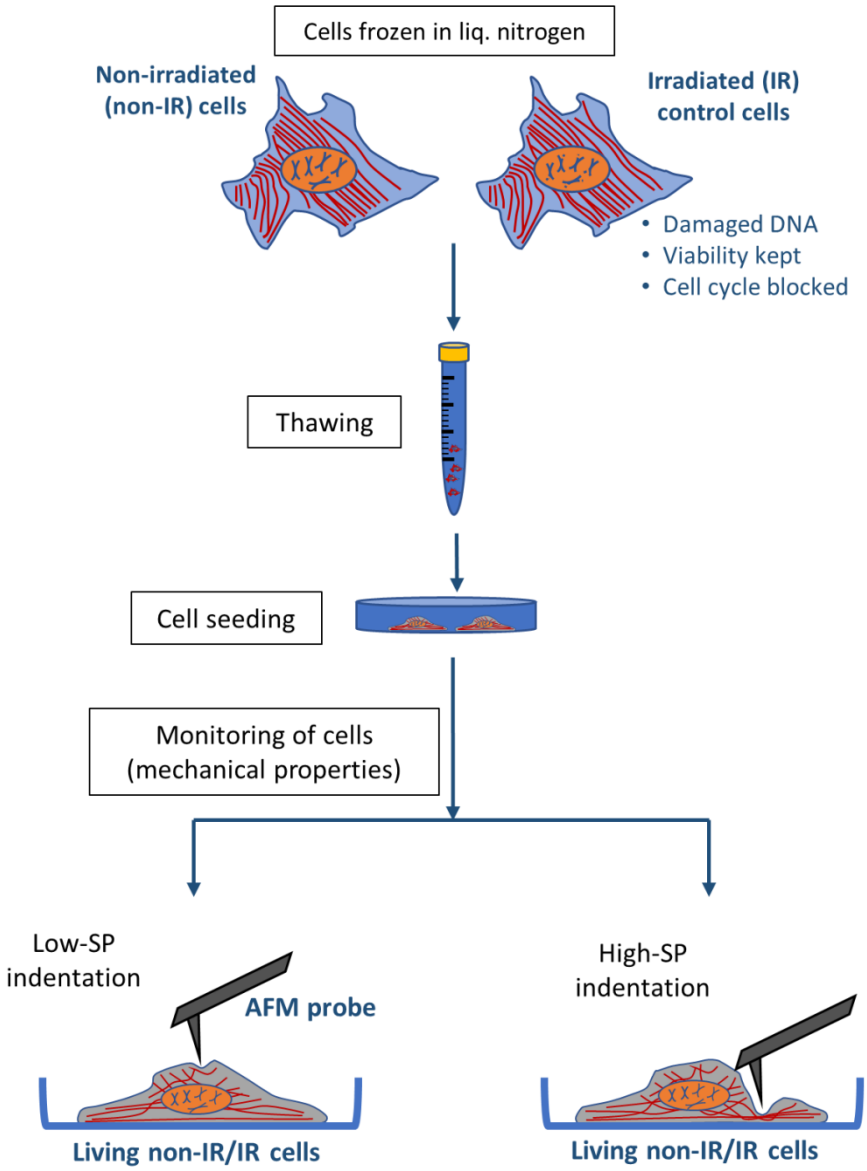

Scheme 3.2.2.1.1: Overall schematic view of the experiments aimed at monitoring the post-thaw development of cell stiffness. Irradiated cells (IR cells) are prepared by exposing the non-irradiated cells (non-IR) to gamma radiation. Irradiation affects cell ability to proceed with the cell cycle, cell viability is however kept unchanged. Both IR and non-IR cells are frozen in liquid nitrogen to be subsequently thawed and plated. Mechanical properties of the cells during the post-thawing period are subsequently monitored by AFM nano-indentation. Low-setpoint and high-setpoint measurements enable probing the cell at different depths (submembrane vs. cytoplasmic region).

When measurements of small areas (10x10 µm^2) were performed (with low SP of 0.4 nN), their position was selected in the space between the cell nucleus and cell edge, thus avoiding affecting the results by distinct mechanical properties of these regions. Each point in **Fig. 3.2.2.1.4** represents statistics from 100 curves at 10x10 µm^2 part of each cell. Mapping area 10x10 µm^2 was selected because for frozen/thawed fibroblasts, it was always possible to locate an area of such size distinct from both the nucleus and the cell edges.

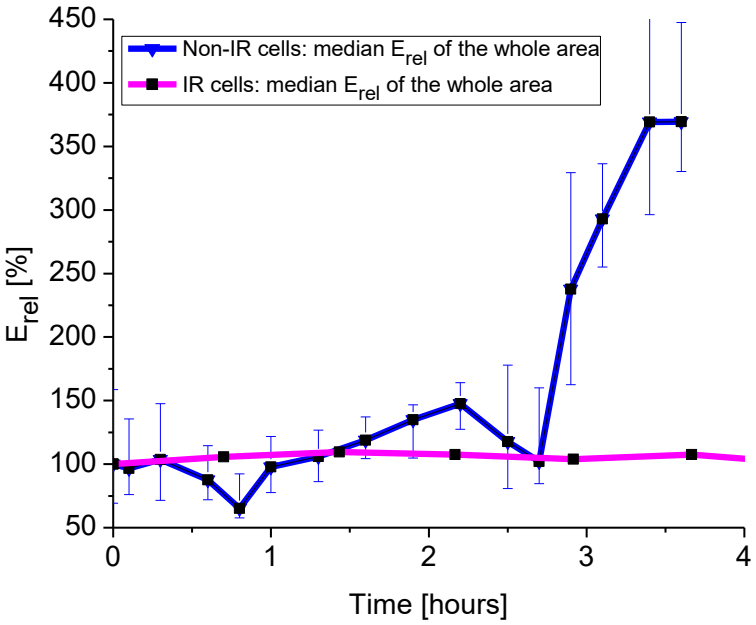

Fig. 3.2.2.1.4: Time development of non-IR and IR fibroblasts' relative value of surface stiffness (relative Young's modulus, E_{rel}) measured by AFM nano-indentation method after thawing. Low SP value of 0.4 nN was used to scan over a small region (10x10 µm^2) situated on a single cell. For non-IR fibroblasts, error bars span values between the 1st and 3rd quartile. For IR fibroblasts, the standard deviation of E from median was smaller than 10% across the measured area. All values are relative to the first datapoints in each respective series.

As low-SP measurements were performed on a relatively small cell area, the values of *E* were quite uniform across the area (maximum deviation from median was 28%), with error bars (1st and 3rd quartile) visible in **Fig. 3.2.2.1.4**. The elastic response of the cell in the measured region was predominantly determined by its

membrane and sub-membrane structures. Until 3 hours after adhesion initiation, the stiffness of the frozen/thawed non-IR fibroblasts oscillated around the initial value, and 2.7 hours after the initiation of adhesion, the fibroblast membrane and sub-membrane structures' stiffness began to increase continually **(Fig. 3.2.2.1.4)**. IR fibroblasts' stiffness (median of YM over measured area) did not change significantly during measured period of time. Hence, the change in stiffness of thawed non-IR cells is a marker of cell activity (reparation mechanisms) while the thawed IR cells show no such signs.

Use of a higher SP value (1.0 nN) and a large mapping area (100x100 μm^2) of frozen/thawed cells enabled observing the inner cell structure which is an important indicator of cell life and development of the whole-cell state. The dynamics of changes in high-SP-measured fibroblast stiffness obtained from stiffness measurements after thawing and plating is shown in **Fig. 3.2.2.1.5**.

Due to fibroblast inhomogeneity, we divided the sample surface into 3 basal regions: the high region, middle region and low region, comprising 80-95%, 30-80% and 15-30% of the sample height above the dish surface, respectively. This selection was used in the case of interpretation of data obtained from 100x100 μm^2 area and high SP AFM measurement. In every such area, around 2000 indentation curves were analyzed. We correlated cell height and stiffness maps.

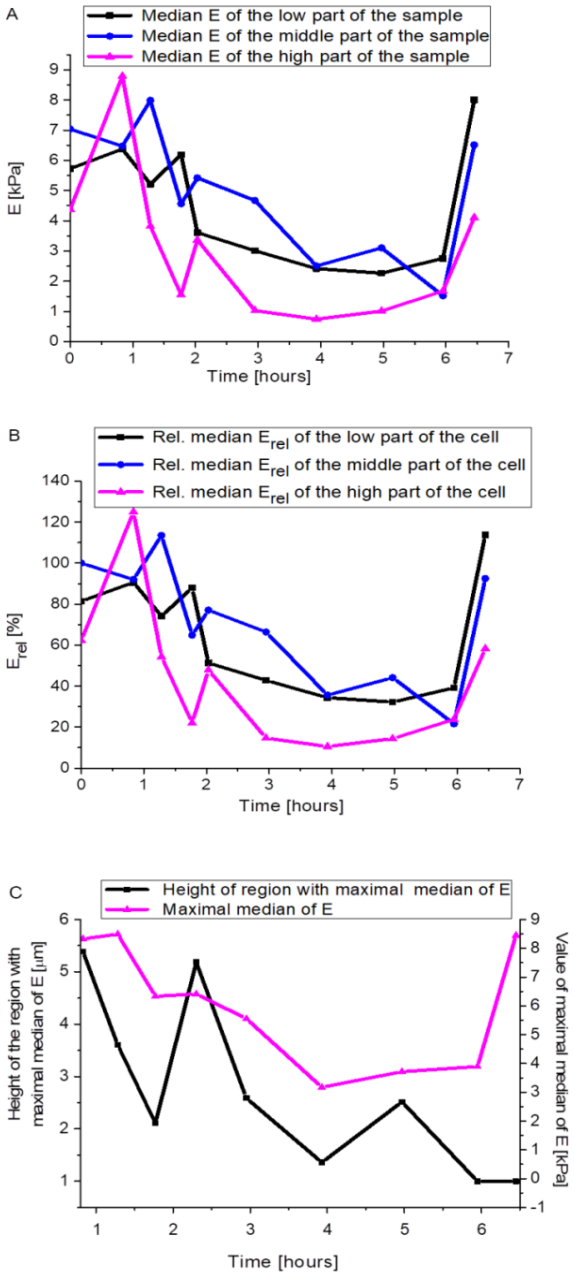

Fig. 3.2.2.1.5: Time development of non-IR thawed fibroblasts' surface stiffness. High-SP AFM nano-indentation was used to scan over a large cell-covered region (100x100 µm^2). A) Median of stiffness (Young's modulus E) change in time in low, middle and high part of cell B) Median of relative values of stiffness (Er_{el}) change in time in low, middle and high part of the cell. C) Time development of the height of the region (in this case, cell was divided to horizontal parts of 0.5 µm in height) with maximal Young's modulus together with the median of E values in the corresponding regions.

One hour after plating, the stiffness of all regions of the sample starts decreasing. Compared to cultured (non-frozen) DMSO-treated fibroblasts, the surface stiffness of cryopreserved fibroblasts is at all parts remarkably lower. Despite that, the distribution of E values measured at each region was relatively broad. That is because a sharp AFM tip is able to distinguish even small spatial inhomogeneities in the cell. The biggest continuous areas was found in the middle part (30-80% of cell height) where the deviation from median *E* of the middle region was smaller than 35%.

Stiffness of the high part of non-IR fibroblast cells is remarkably lower than stiffness of the low and middle parts (**Fig. 3.2.2.1.5 a, b**). The stiffness of the surface in the high area of the sample begins to increase more than 5 hours after plating.

For non-IR fibroblasts, the stiffness of the low part of the sample decreases 1.5 hours after thawing/plating. As time progressed (more than 5 hours after plating), the stiffness of the border (low) part of the cell markedly increased. More than 6 hours after plating, the edge of the cell had a much stiffer surface compared to the highest part of the sample (**Fig. 3.2.2.1.5**). The stiffness of the middle part, following initial decrease after thawing/plating, increased back in 6 hours (**Fig. 3.2.2.1.5**).

Fig. 3.2.2.1.5c shows that the non-IR cells region with maximum median *E* (YM) gradually shifts from higher parts of the cells to their lower parts. At the same time, median *E* itself decreases as well. Its decrease is however less pronounced in the lower parts of cells, which may reflect an ongoing reconstruction of the inner parts of the cell. Non-IR cells immediately after thawing and plating had the highest elevation and stiffness. After 1.5 hours, the interaction of cell with the substrate gradually built and cell stiffness and height significantly decreased. Six hours after plating, the reconstruction of the inner parts of the cell probably begins as cell height decreased and cells stiffness significantly increased.

Compared to non-IR fibroblasts, the repairs of the inner and surface parts of the IR cells were not significant at any of the 3 basal regions. Results obtained by low SP AFM on IR fibroblasts indicated that extensive remodeling did not occur. The stiffness of non-IR fibroblasts increased significantly after 6 hours, which is possibly

related to cell regeneration since IR cells (not able to regenerate) did not show such development.

Non-frozen/cultured fibroblasts stiffness was slightly growing immediately after plating and oscillated around 115-128% of the initial low-SP *E* value 4 hours after plating. The viability of the cells probed by AFM measurements was checked at the time points up to 6 hours in a way corresponding to force mapping procedures. It was shown that viability of AFM-tested cells was more than 90% (**Fig. 3.2.2.1.6**).

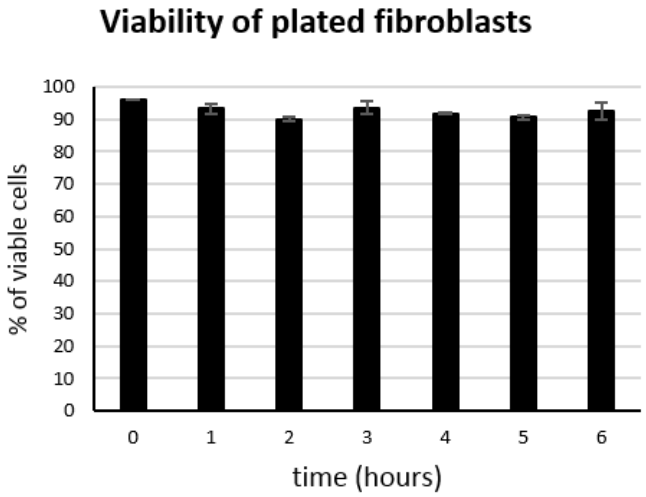

Fig. 3.2.2.1.6. The viability of the cells tested by AFM testing was checked at the timepoints to correspond to force mapping procedures time points. All timepoints show high viability of attached cells that does not change with time.

3.2.2.2 AFM monitoring of the influence of selected cryoprotectants on regeneration of cryopreserved cells mechanical properties

We measured the surface stiffness of cells treated with DMSO or PEG-1500. By repetitive measurements we further observed the dynamics of the development of the cell surface stiffness in detail. In order to see the differential effect of cryoprotectants on different parts of the cryopreserved cells we correlated the surface stiffness maps and cell surface height (**Figs. 3.2.2.2.1, 3.2.2.2.2**).

For the purpose of monitoring the mean stiffness values of the cryopreserved cells in time, we defined two major cell regions defined by percentages of cell height. The core/nuclear region formed 50-100% of the total cell height and cell edges located outside the nuclear region formed 0-50% of the total height of the cell (**Figs. 3.2.2.2.3, 3.2.2.2.4**).

DMSO affected most significantly the cell's stiffness in the core region. Approximately 30 mins after thawing, the DMSO-treated cells had a nucleus softer (mean values) than surrounding cytoplasm **(Fig. 3.2.2.2.1**). On the contrary, PEG-cryopreserved cells have a more spheroidal shape after thawing and initial attaching, with rather homogeneous spatial distribution of stiffness (mean values). The stiffness of PEG-treated frozen/thawed cells nuclei are close to stiffness of the surrounding cytoplasm (mean values) **(Fig. 3.2.2.2.2**).

The observed difference in cell properties is likely underlied by the different molecular behaviour of DMSO and PEG. DMSO itself causes thickening of microfilaments and formation of stress fibers (Lampugnani et al. 1987) while nonpenetrating PEG can’t interact with the cytoskeleton during freezing/thawing. Therefore, it can‘t prevent the disruption of actin fibers and the slowdown of the initiation of new actin protein expression caused by the freezing process (Lin and Tsai 2012).

Time development of stiffness of cryopreserved cells reflects the cryoprotectant interaction with the cell and cryoprotective functionality of the material. The stiffness of PEG treated frozen and thawed cells was low (compared to DMSO treated cells - **Fig. 3.2.2.2.3, Fig. 3.2.2.2.4**) and homogeneous over the whole cells (**Fig. 3.2.2.2.2**). The stiffness of PEG-treated cells (compared to DMSO-treated cells) changes in time relatively mildly after thawing. The time required for proper attachment significantly differ between DMSO and PEG medium. The time required for flattening of the cell was 27±15 min in DMSO and 53±24 min in PEG freezing medium. This corresponds to the measured greater height of the PEG-frozen cells and constant lower stiffness.

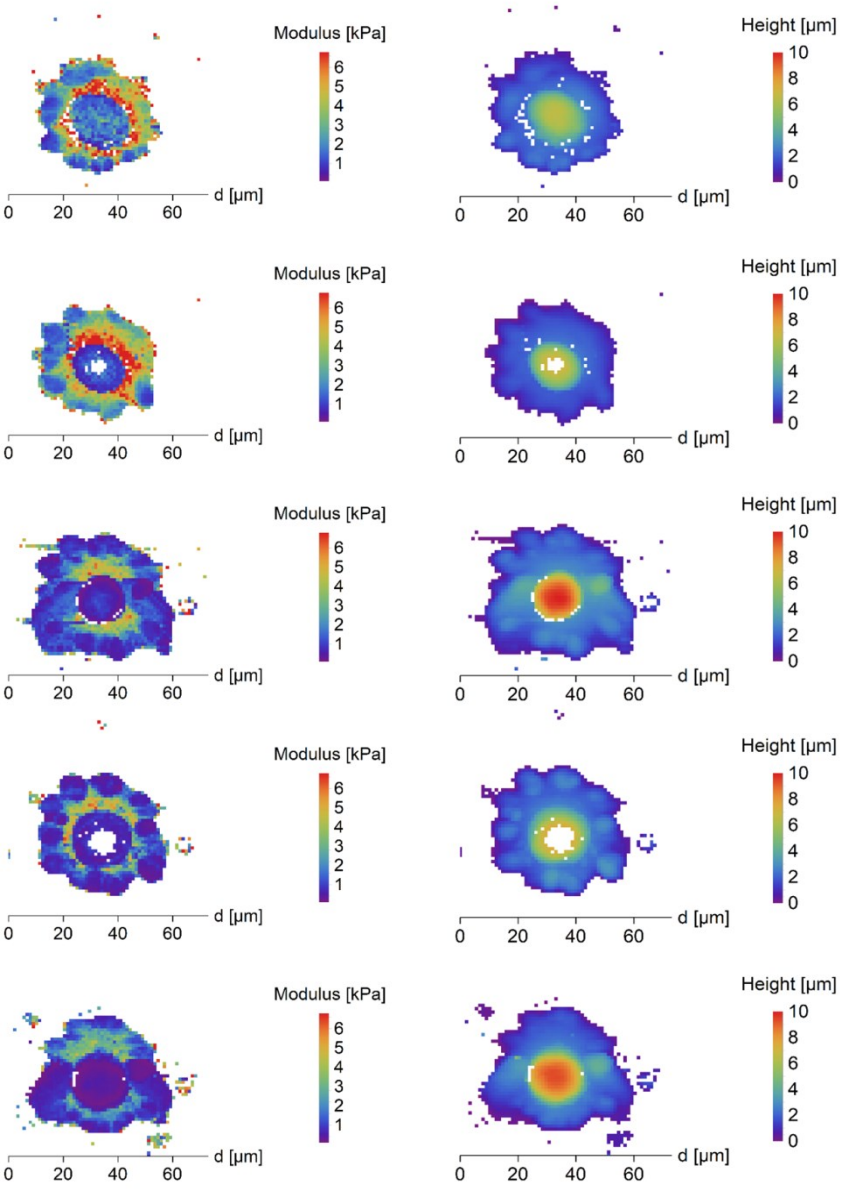

Fig. 3.2.2.2.1: AFM maps of Young's Modulus (left), height (column of image in the middle) and fluorescence images of cytoskeleton (right) of DMSO treated frozen/thawed cells during monitoring of the post-thawing process. Each step shows a change of the cell biomechanical and structural properties during 60 minutes of the cell life. DMSO affected most significantly the cell's stiffness in the core region. First measurements was made after cell adhered on the surface (30 minutes post-thawing). The DMSO-treated cells had a softer core after thawing - compared to extra nuclear region/ surrounding cytoplasm and clearly recognizable cytoskeleton in the map of thawed cells surface stiffness (Golan et al. 2018a).

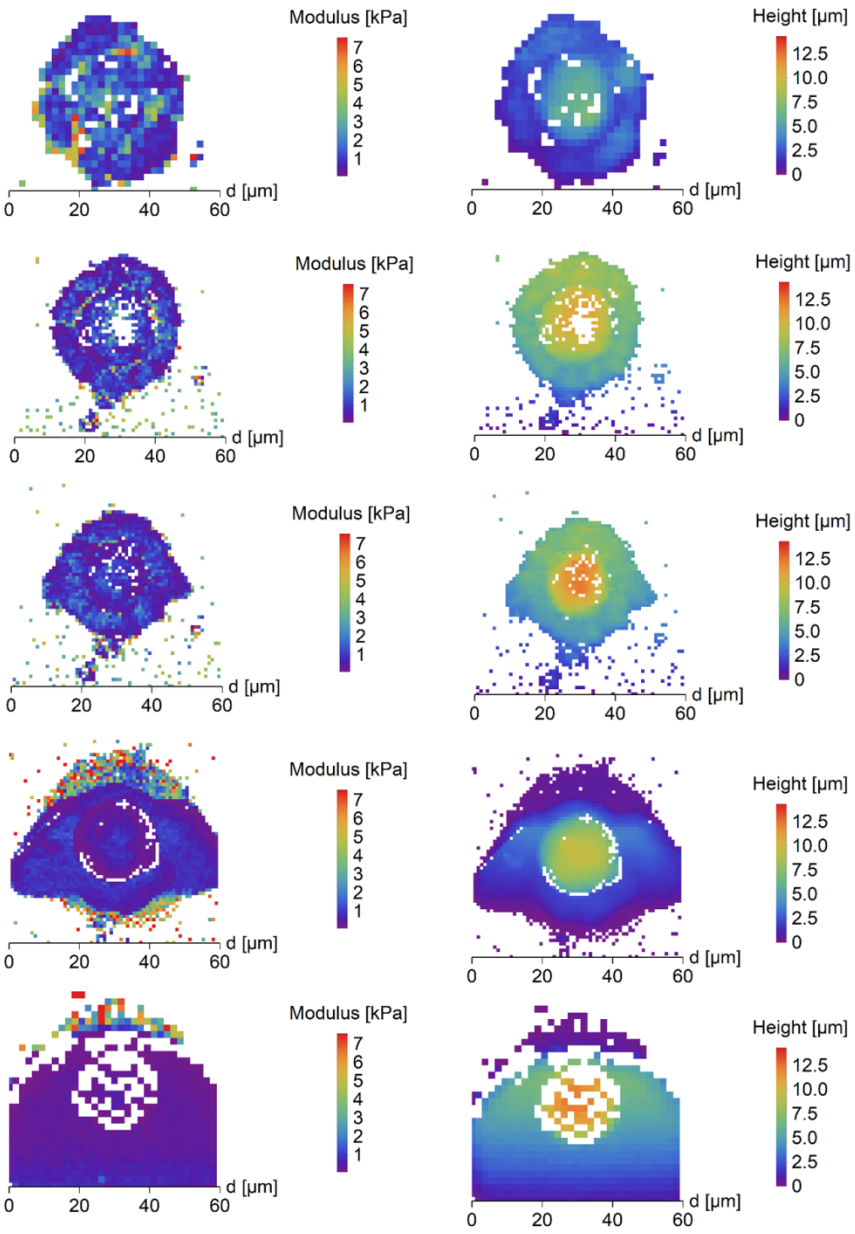

Fig. 3.2.2.2.2: AFM maps of Young's Modulus (left), height (column of image in the middle) and fluorescence images of cytoskeleton (right) of polyethylene glycol (Mw 1500, PEG-1500) treated frozen/thawed cells during monitoring of the post-thawing process. Each step shows a change of the cell biomechanical and structural properties during 60 minutes of the cell life. First measurements was made after cell adhered on the surface (30 minutes post-thawing). Polyethylene glycol (Mw 1500) treated cells both cytoskeleton and cell nuclei became softer and the height of the cell increased (Golan et al. 2018a).

As far as cell stiffness time development after thawing is concerned, the stiffness of DMSO-cryopreserved cells significantly decreases during first 2 hours (up to 60%), while the stiffness change of the PEG-1500-cryopreserved cell is low (maximum decrease of 20%) even during 4 hours after thawing (**Figs. 3.2.2.2.3, 3.2.2.2.4**). For DMSO or PEG treated frozen and thawed cells the values of *E* from the core part of the cell had the smallest spatial deviation from median *E* – less than 10%. Such deviation corresponds to relatively sharp distributions of *E* values (within core regions). Spatial deviation of *E* from the whole area median of *E* was for extra-nuclear cells regions smaller than 20%.

The difference in stiffness between the core and the edge of DMSO treated/ thawed cells was reduced within 2 hours after thawing.

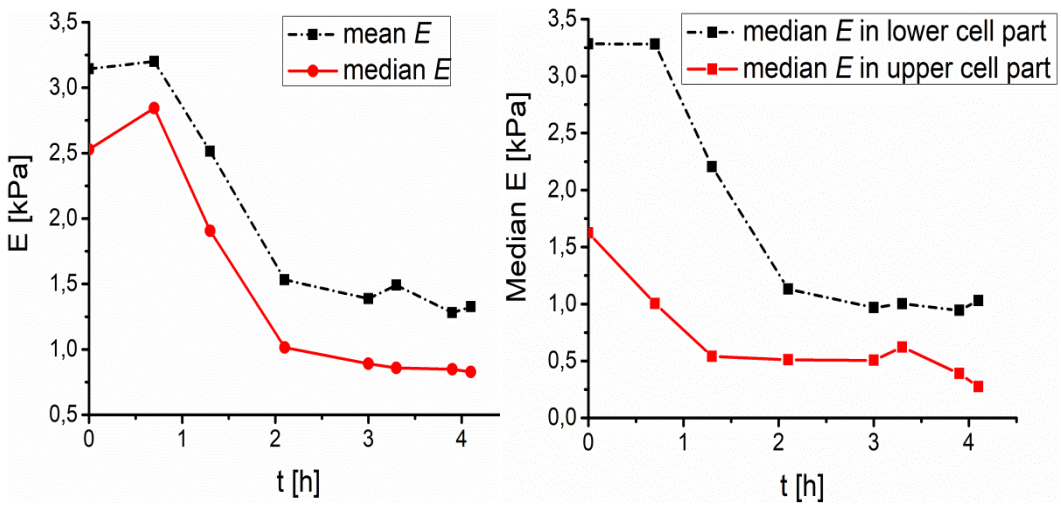

Fig. 3.2.2.2.3 Time development of DMSO treated fibroblasts surface elasticity median after thawing. Left: Median and mean value of elasticity over time, right: median value of elasticity in lower (0-50% of the full cell height), and higher (50-100% of the full cell height) part of cell over time. Values of *E* from the core part of the cell had the smallest spatial deviation from median *E* – less than 10%. Spatial deviation of *E* from the whole area median of E was for extra-nuclear cells regions smaller than 20% (Golan et al. 2018a).

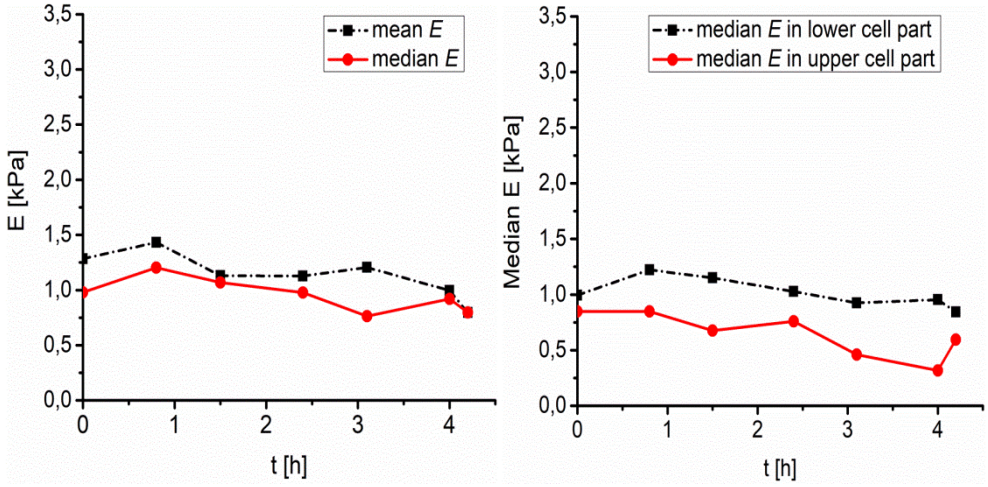

Fig. 3.2.2.2.4 Time development of PEG treated fibroblasts surface elasticity (Young's modulus E) after thawing. Left: Median and mean value of elasticity over time, right: median value of elasticity in lower (0-50% of the full cell height), and higher (50-100% of the full cell height) part of cell over time. Values of E from the core part of the cell had the smallest spatial deviation from median *E* – less than 10%. Spatial deviation of E from the whole area median of E was for extra-nuclear cells regions smaller than 20% (Golan et al. 2018a).

3.2.3 Critical defects in cryopreserved cell nuclei (envelope disruption, chromatin condensation, DNA breaks)

Firstly, we identified important DNA defects associated with the freezing (-80°C; rate of -1°C/min) and thawing of normal human skin fibroblasts (NHDF) and MCF7 mammary carcinoma cells (MCF7). We showed that MCF7 and NHDF frozen/thawed cells exhibited enhanced numbers of γH2AX/53BP1 foci. These foci corresponded to collapsed replication forks that possibly turned into DSBs. The additional co-staining of the DSB-marker protein 53BP1 (Schultz et al. 2000) was done because γH2AX foci can be formed even in the absence of DSB (Loebrich et al. 2010). Using high-resolution immunofluorescence confocal microscopy for γH2AX and 53BP1 signals (Hofer et al. 2016a), we compared DSB induction in frozen and thawed cells that had been cryopreserved in standard medium ("untreated cells") or in standard medium supplemented with different cryoprotectants – trehalose,

DMSO or trehalose+DMSO according to **Tab. 2.2.3.2.1.** ("cryoprotectant-treated cells").

Using high-resolution immunofluorescence confocal microscopy to detect γH2AX and 53BP1 signals, which are the two accepted markers of DSBs (Hofer et al. 2016b), we compared DSB induction in frozen and thawed cells that had been cultured in standard medium (untreated cells) or in standard medium supplemented with cryoprotectants of different classes, which have different abilities to penetrate cells (or even the cell nuclei) and influence the chromatin status. Since γH2AX foci can be formed in the absence of DSBs, in parallel, we co-stained cells with an additional DSB marker, the protein 53BP1. We also irradiated MCF7 and NHDF cells with 1 Gy or 2 Gy of γ-rays as a DSB positive control. This process resulted in the rapid development of relatively large γH2AX foci co-localized with the 53BP1 repair protein 30 min post-irradiation, showing extensive formation of γH2AX/53BP1 (DSB) foci with approximately 23 DSB/Gy/nucleus (**Fig. 3.2.3.1 D)**.

Mere incubation with the respective cryoprotectants had only minor effects on the viability of non-frozen cells and did not increase DSB induction.

After freezing and thawing (-80°C; rate of -1°C/min), we identified important DNA defects that were associated with this process in both NHDF and MCF7 cells. Based on the character of these defects, the populations could be sorted into three distinct groups. In all samples, we found a small population of cells that exhibited a dramatically enhanced number of γH2AX/53BP1 foci (>30 to >100 foci/nucleus). A second, more numerous subpopulation contained cells with very few foci (<30 foci/nucleus). Finally, some cells showed diffuse, localized or pan-nuclear γH2AX signal that did not colocalize with 53BP1 (**Fig. 3.2.3.1**).

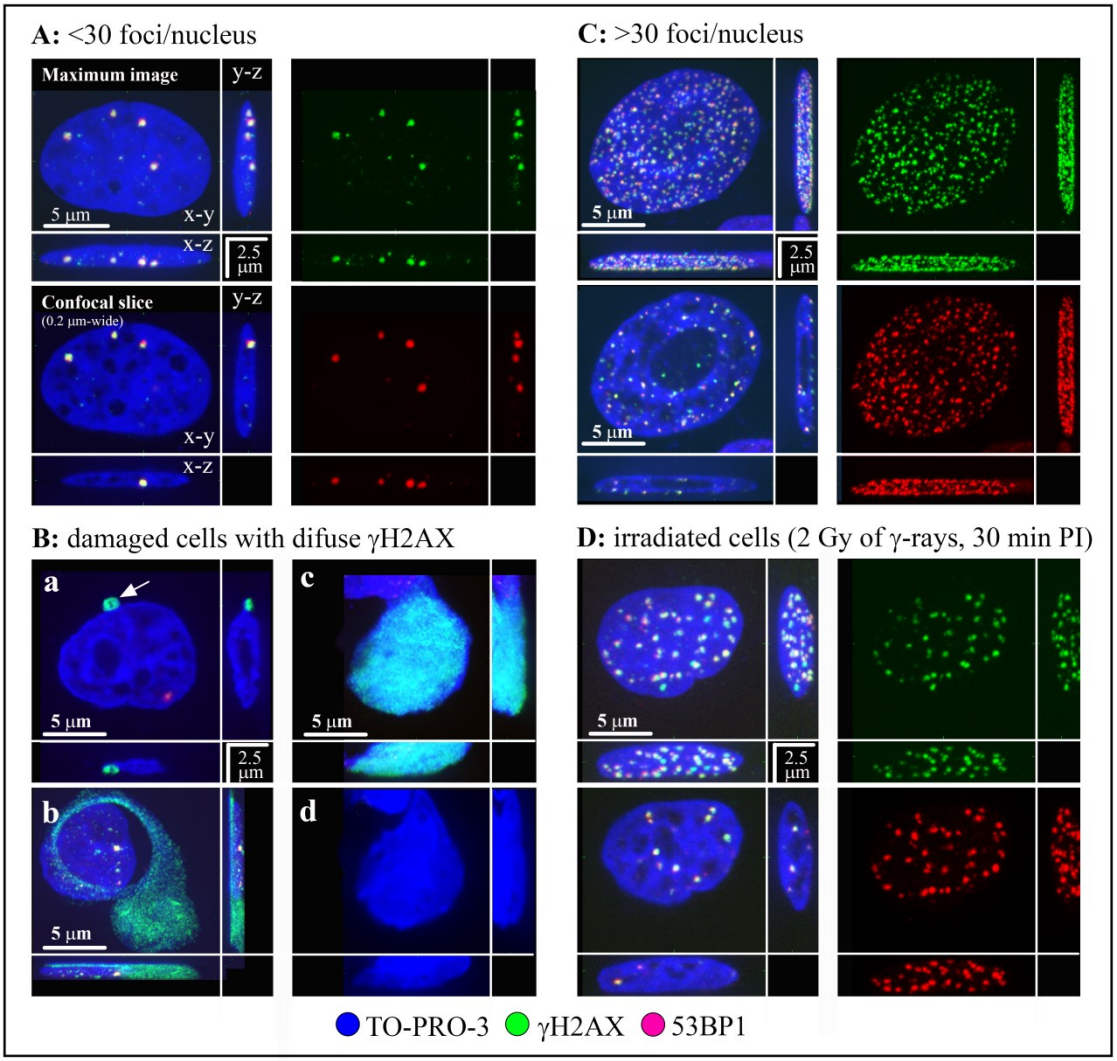

Fig. 3.2.3.1. Three main categories (A–C) of MCF7 cells according to their γH2AX signal upon freezing/thawing. A. The majority of cells remained unaffected by freezing/thawing in terms of DSB induction (*category A, <30 γH2AX/53BP1 foci*); the cells of this category were typical for DMSO-treated samples since in unprotected ones or those incubated with trehalose, a substantial proportion of cells had damaged nuclei (B). In category **B**, nuclei were stained with diffuse, localized (**a**, **b**) or pan-nuclear (**c**) γH2AX signals that did not colocalize with 53BP1. Cells with localized intense γH2AX signals largely preserved chromatin structure but with localized structureless chromatin protrusion(s) from the cell nucleus (white arrow). The chromatin structure of cells with pan-nuclear γH2AX was frequently altered (**d**), typically decondensed with complete loss of structure (panel **d** only shows chromatin staining). **C.** A fraction of cells showed, for all cryoprotectant treatments,

extremely high numbers of tiny γH2AX foci (green) that colocalized with 53BP1 protein foci (red) (*category C, >30 γH2AX/53BP1 foci*). The overall chromatin structure of these cells remained preserved, especially in cryopreserved samples. **D**. Formation of γH2AX/53BP1 foci at sites of DNA double strand breaks (DSBs) in MCF7 cells irradiated with 2 Gy of γ-rays (^{60}Co, 1 Gy/min) and visualized 30 min post-irradiation. γH2AX – green, 53BP1 – red, TO-PRO-3 (chromatin) – blue (Falk et al. 2018).

The nuclear patterns (numbers plus spatial distributions) of γH2AX/53BP1 foci in cells with >30 γH2AX/53BP1 foci (many of them even contained >100 γH2AX/53BP1 foci/nucleus) were clearly different from the rest of those in freeze-damaged cells or cells exposed to γ-radiation (**Figs. 3.2.3.1** and **3.2.3.2)**.

A careful inspection of the images in 3D-space allowed us to sort cells with high frequencies of γH2AX/53BP1 into three categories, as presented in **Fig. 3.2.3.2**: nuclei belonging to the 1st category contain approximately 100 or more small γH2AX/53BP1 foci dispersed throughout the nucleus; nuclei in the 2nd category have similar numbers of small γH2AX/53BP1 foci, but these foci are concentrated along the nuclear rim; finally, nuclei in the 3rd category show a mixture of approximately 30 to 100 both small and large γH2AX/53BP1 foci distributed along the nucleolus and irregularly throughout the rest of the nucleus.

The γH2AX/53BP1 foci patterns in categories 1, 2 and 3 perfectly corresponded to those observed in early-, mid-, and late-S-phase (replicating) cells with collapsed (e.g., by camptothecin or topotecan) replication forks (Berniak et al. 2013; Zhao et al. 2012). It is thus reasonable to assume that γH2AX/53BP1 foci (cells of category 1 – 3) correspond to replication forks in S-phase cells that had collapsed upon freeze/thaw. In the following section, we back up this claim by further conclusive evidence.

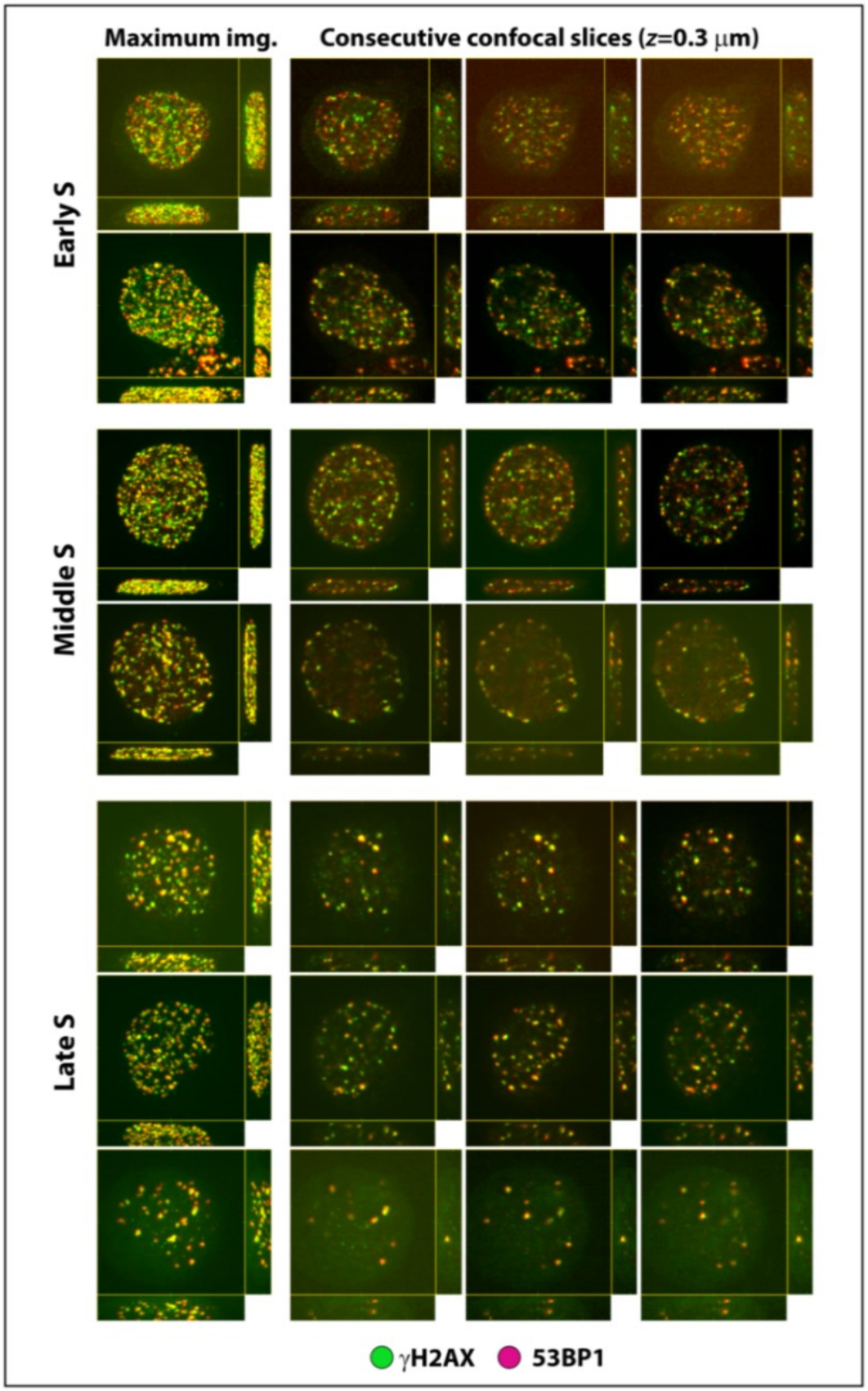

Fig. 3.2.3.2. Three subcategories of MCF7 cells with high numbers of γH2AX/53BP1 **foci/nucleus after freezing/thawing, as determined using immunofluorescence confocal microscopy.** Category 1 (top): nuclei with about >100 small γH2AX/53BP1

foci dispersed throughout the nucleus. Category 2 (middle): nuclei with >100 small γH2AX/53BP1 foci but distributed largely along the nuclear rim. Category 3 (bottom): nuclei with approximately 30 to 100 both small and large γH2AX/53BP1 foci distributed along the nucleolus and irregularly throughout the rest of the nucleus. There is evident similarity between the described γH2AX patterns (numbers and distribution) and the patterns of early (top), mid (middle), and late (bottom) S-phase replication (left captions). γH2AX foci (cells of category 1 – 3) thus seem to represent replication forks in S-phase cells, collapsed upon freeze/thaw. 3D projections (x-y, x-z and y-z) of representative nuclei are shown for the composed of 40 confocal slices, each 0.3 µm thick (left column) and three consecutive single confocal slices, 0.3 µm thick (remaining columns). γH2AX – green, 53BP1 – red, chromatin staining suppressed to improve the visibility of γH2AX/53BP1 foci.

For never frozen (unfrozen) and frozen/thawed cells we directly compared the proportions of cells with >30 γH2AX/53BP1 foci/nucleus with the proportions of replicating (S-phase) cells determined by flow cytometry (PI staining, **Tab. 3.2.3.1**, **Fig. 3.2.3.3)**. Number of S-phase unfrozen cells was higher for the faster-propagating MCF7 cells (approximately 13%, **Tab. 3.2.3.1**) than for NHDF fibroblasts (approximately 8%, **Tabs. 3.2.3.1** and **3.2.3.2**). A fraction of cells, containing more than 30 γH2AX/53BP1 foci/nucleus, was very rare (<1%) among cryoprotectants-treated and untreated non-frozen MCF7 and NHDF cells.

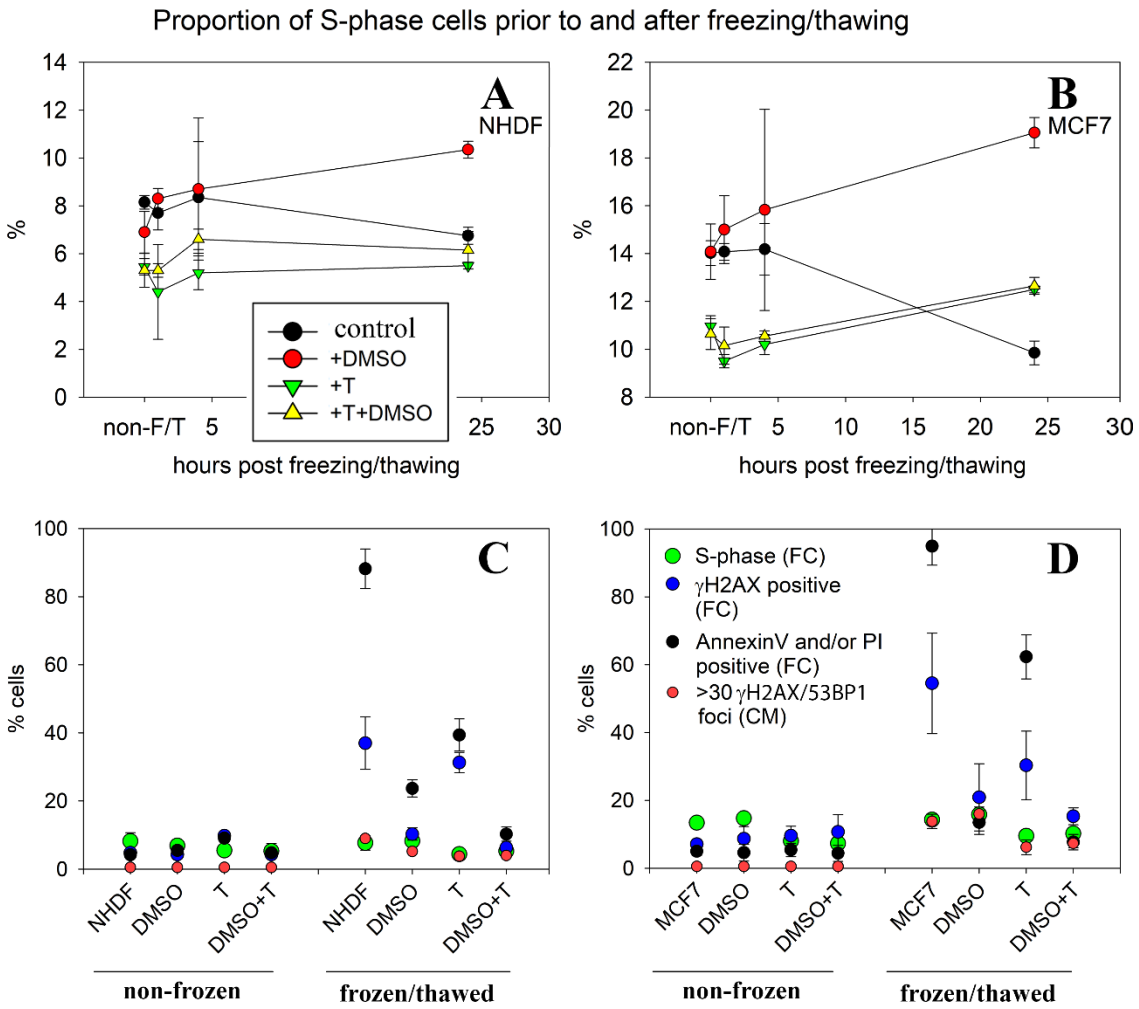

Fig. 3.2.3.3. Fractions [%] of S-phase NHDF (A) and MCF7 (B) cells before freezing and at different time periods after freezing/thawing, determined by flow cytometry (PI staining), for the indicated cryoprotectant treatments**.** Dish-attached cells and cells released into culture media were included into the analyses. Fractions [%] of NHDF (C) and MCF7 (D) cells with >30 γH2AX/53BP1 foci, determined using immunofluorescence confocal microscopy (CM) prior to and 30 min after freezing/thawing (F/T), are compared to flow cytometric fractions of S-phase cells, γH2AX-positive cells and Annexin V/PI-positive cells were quantified using flow cytometry (FC) prior to and 1 h after F/T. S-phase cells were identified using propidium iodide (PI) staining to show DNA content. Values represent the means and standard errors (Falk et al. 2018).

Table 3.2.3.1. Fractions [%] of NHDF and MCF7 cells with >30 γH2AX/53BP1 foci before freezing and after freezing/thawing compared to the fraction [%] of S-phase cells. Results for the indicated cryoprotectant treatments are shown. The fractions of cells with >30 γH2AX/53BP1 foci were determined using immunofluorescence confocal microscopy (CM) prior to and 30 min after freezing/thawing. S-phase cells were quantified at the corresponding times by flow cytometry with propidium iodide (PI) staining. Values represent the means and standard errors (Falk et al. 2018).

NHDF cells **Non-frozen cells**	**Treatment**	**Cells with >30 foci (CM)**	**S-phase cells (PI staining FC)**
	Untreated	0.5±0.2	8.2±2.5
	Trehalose	0.5±0.2	5.5±1.5
	DMSO	0.5±0.2	6.9±1.7
	DMSO+trehalose	0.5±0.2	5.3±2.2
NHDF cells **Cells after freezing/thawing (30 min)**	**Treatment**	**Cells with >30 foci (CM)**	**S-phase cells (PI staining FC)**
	Untreated	9.0±0.5	7.7±2.5
	Trehalose	3.8±0.2	4.4±0.6
	DMSO	5.2±0.4	8.3±1.6
	DMSO+trehalose-	4.0±0.2	5.3±1.5
MCF7 cells **Non-frozen cells**	**Treatment**	**Cells with >30 foci (CM)**	**S-phase cells (PI staining FC)**
	Untreated	0.5±0.2	13.4±0.2
	Trehalose	0.5±0.2	8.0±0.5
	DMSO	0.5±0.2	14.7±1.2
	DMSO+trehalose	0.5±0.2	7.3±0.5
MCF7 cells **Cells after freezing/thawing (30 min)**	**Treatment**	**Cells with >30 foci (CM)**	**S-phase cells (PI staining FC)**
	Untreated	13.8±2.1	14.3±0.4
	Trehalose	6.2±2.2	9.5±0.6
	DMSO	16.0±2.0	15.8±0.3
	DMSO+trehalose	7.3±2.3	10.2±0.6

For both cell types and all treatments, the percentage of S-phase cells before and after freezing/thawing doesn't change (**Tab. 3.2.3.1**. and **Fig. 3.2.3.3**). On the other hand, the percentages of cells with >30 γH2AX/53BP1 foci/nucleus rise from less than 1% before thawing to percentages corresponding to the S-phase population sizes. That supports the notion that the thawed cells with many foci are mostly S-phase cells which during freezing/thawing suffered damage specific for their cell cycle phase.

Regardless of the cryoprotectant used, the number of cells exhibiting >30 γH2AX/53BP1 foci/nucleus decreased 8 h after freezing/thawing, indicating that a proportion of S-phase cells with collapsed replication forks either repaired their damage (with potential damage to genetic information due to misrepair) or died due to irreparable damage (**Fig. 3.2.3.3**).

To further specify the nature of the S-phase cell damage, we also show that the γH2AX/53BP1 foci in these cells colocalized with proliferating cell nuclear antigen (PCNA)**,** a key factor in DNA replication that is localized to replication forks (**Fig. 3.2.3.4)**. These results thus confirmed the identification of γH2AX/53BP1 foci with collapsed replication forks in cells with >30 γH2AX/53BP1 foci. The proliferative status of these cells was further supported by immunofluorescence microscopy images of frozen/thawed MCF7 cells stained with anti-γH2AX and anti-Ki67 antibodies, which in most of the cells with >30 γH2AX foci revealed preferential nucleolar Ki67-staining, as is typical of S-phase.

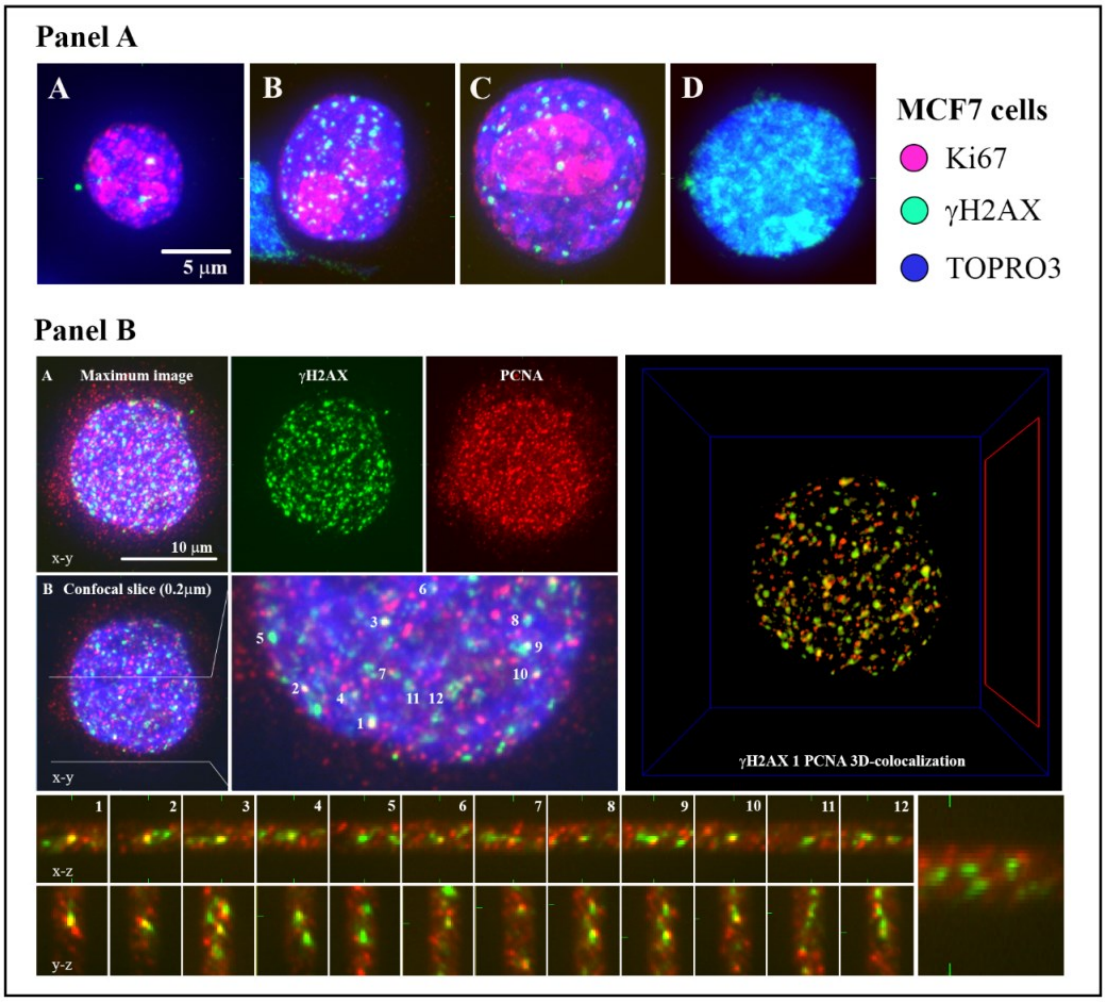

Fig. 3.2.3.4. Cells with >30 -γH2AX/53BP1 foci are S-phase cells with collapsed replication forks. Panel A. Immunofluorescence microscopy of frozen/thawed MCF7 cells, stained with anti-γH2AX (green) and anti-Ki67 (red) antibodies, demonstrates the S-phase status of the cells with >30 γH2AX foci. **A**. Cell nuclei with <30 γH2AX foci mostly showed jaguar-like patterns of Ki67 distribution typical of G1-phase or nucleolar staining with nucleoplasmic staining typical of G2-phase. **B+C**. Cell nuclei with >30 γH2AX foci predominantly showed intense nucleolar Ki67-staining as typical for S-phase cells. **D.** Most nuclei with pan-nuclear γH2AX staining (apoptotic or disintegrated nuclei) showed no Ki67 signal. Maximum projection images composed of approximately 40 confocal slices, each 0.3 µm thick, are displayed. Chromatin was counterstained with TOPRO3 (artificially colored blue). **Panel B.** Immunofluorescence microscopy of frozen/thaw MCF7 cells, stained with anti-γH2AX (green) and PCNA (red) antibodies, demonstrates the colocalization

of γH2AX foci with replication forks (PCNA) in cells containing >30 γH2AX foci. **A**. Maximum projection images (composed of approximately 40 confocal slices, each 0.3 µm thick), showing patterns for anti-γH2AX and anti-PCNA antibodies, merged and separately. **B.** Same as (A) but only showing the central confocal slice. The right panel shows an enlarged view of the colocalization of γH2AX and PCNA signals in the x-y plane. **C**. Detailed 3D colocalization for twelve γH2AX foci shown in (B) (right panel). **D.** Software-generated 3D-colocalization for all γH2AX and PCNA foci (Acquiarium software). Chromatin was counterstained (where relevant) with TOPRO3 (artificially colored blue)(Falk et al. 2018).

Cryoprotectants added to the cell cultures prior to freezing/thawing do not influence their susceptibility to the collapse of replication forks due to freeze/thaw (**Fig. 3.2.3.3**). Trehalose decreased the proportions of total S-phase cells both in never frozen and frozen/thawed cells.

The collapse of replication forks caused by freezing/thawing is expected to affect more severely cell populations where S-phase cells are more abundant. That is typical for rapidly dividing (e.g. cancer) cells. The long-term development of thawed cells with collapsed replication forks remains to be elucidated. A collapsed replication fork may possibly be repaired or transformed into a double-strand break (DSB) (Fugger et al. 2015; Yingjie Zhu 2017). The damaged cells likely die, but their survival cannot be ruled out (Maya-Mendoza et al. 2014). This poses a threat of pathological changes in the genome and/or epigenome resulting from defective repair, even if the DNA lesions are not converted into DSBs (Rasmussen et al. 2016; Sarni and Kerem 2017).

In addition to immunofluorescence microscopy, we quantified γH2AX-fluorescence using flow cytometry, which provided us with a broad view of chromatin defects in statistically relevant numbers of cells (**Table 3.2.3.2**). All frozen/thawed samples showed higher fractions of cells with increased γH2AX-fluorescence compared to never-frozen cells, for both normal human skin fibroblasts (NHDF) and mammary carcinoma cells (MCF7). While the highest increase (up to approximately 40%, 30 min after thawing) appeared in unprotected controls, these values were lower in trehalose-treated samples and the lowest in cells treated with DMSO or the combination of trehalose+DMSO.

Table 3.2.3.2. Proportions [%] of NHDF (A) and MCF7 (B) cells with >30 γH2AX/53BP1 foci/nucleus compared to proportions of S-phase cells, γH2AX-positive cells and Annexin V/PI-positive cells. Cells with >30 γH2AX/53BP1 foci/nucleus were determined using immunofluorescence confocal microscopy (CM); γH2AX-positive and S-phase cells were quantified by flow cytometry using γH2AX/H2AX and Propidium iodide (PI, DNA content) staining. Experiments were performed prior to and 30 min after freezing/thawing (F/T). The values are the means with standard errors. CM, confocal microscopy; FC, flow cytometry; PI, propidium iodide

A. NHDF cells		Cell categories			
Treatment		with >30 γH2AX/53BP1 foci (CM)	in S-phase (PI staining; FC)	γH2AX-positive (FC)	annexin V/PI positive (FC)
non-frozen	untreat.	<0.5	8.2 ± 2.5	4.8 ± 1.1	4.2 ± 0.4
	DMSO	<0.5	6.9 ± 1.7	4.3 ± 0.8	5.5 ± 1.2
	T	<0.5	5.5 ± 1.5	9.8 ± 0.4	9.1 ± 0.9
	DMSO+T	<0.5	5.3 ± 2.2	4.3 ± 0.4	4.8 ± 0.3
post-F/T	untreat.	9.0 ± 0.5	7.7 ± 2.1	37.0 ± 7.7	88.2 ± 5.8
	DMSO	5.2 ± 0.4	8.3 ± 1.8	10.3 ± 1.8	23.7 ± 2.5
	T	3.8 ± 0.2	4.4 ± 0.6	31.3 ± 3.0	39.4 ± 4.7
	DMSO+T	4.0 ± 0.2	5.3 ± 1.5	6.3 ± 0.7	10.3 ± 2.1

B. MCF7 cells		Cell categories			
Treatment		with >30 γH2AX/53BP1 foci (CM)	in S-phase (PI staining; FC)	γH2AX-positive (FC)	annexin V/PI positive (FC)
non-frozen	untreat.	<0.5	13.4 ± 0.2	7.1 ± 0.7	5.0 ± 1.2
	DMSO	<0.5	14.7 ± 1.3	8.7 ± 3.6	4.6 ± 2.5
	T	<0.5	8.0 ± 0.5	9.6 ± 2.8	5.4 ± 2.0
	DMSO+T	<0.5	7.3 ± 0.5	10.7 ± 5.1	4.4 ± 2.4
post-F/T	untreat.	13.8 ± 2.1	14.3 ± 0.4	54.5 ±14.8	94.9 ± 5.6
	DMSO	16.0 ± 2.0	15.8 ± 0.3	20.9 ± 9.9	18.1 ± 3.5
	T	6.2 ± 2.2	9.5 ± 0.2	30.3 ±10.1	62.3 ± 6.5
	DMSO+T	7.3 ± 1.3	10.2 ± 0.6	15.3 ± 2.5	7.7 ± 2.3

A comparison of confocal microscopy and flow cytometry results provided interesting conclusions: The relative number of S-phase cells with >30 γH2AX/53BP1 foci/nucleus was strongly correlated with the relative number of all γH2AX-positive cells, as determined by flow cytometry of cells frozen/thawed with DMSO (**Tab. 3.2.3.2**). The proportion of (damaged) replicating cells with >30 γH2AX/53BP1 foci was much lower than the proportion of all cells positive for γH2AX (flow cytometry) in cells frozen/thawed with no cryoprotectants or with trehalose only. In these cultures, microscopy revealed numerous cells with higher-order alterations in chromatin structure (TO-PRO3 staining), chromatin protrusions (stained with γH2AX but not 53BP1) or completely disintegrated chromatin (**Figs. 3.2.3.1, 3.2.3.5**).

These results suggest that freezing affects chromatin in at least two distinct ways, both leading to γH2AX phosphorylation.

Firstly, S-phase cells have collapsed replication forks after freezing/thawing, which was not prevented by any cryoprotectant studied. Collapsed replication forks thus represent the dominant type of damage in cells cryopreserved with DMSO or trehalose+DMSO. Currently, the best way to avoid this type of damage is to exclude S-phase cells from the population prior to freezing/thawing.

Secondly, freezing/thawing affects the higher-level integrity of cell nucleus. This type of disruption is preventable by a suitable cryoprotectant. In our case, the best result was achieved with a combination of trehalose and DMSO.

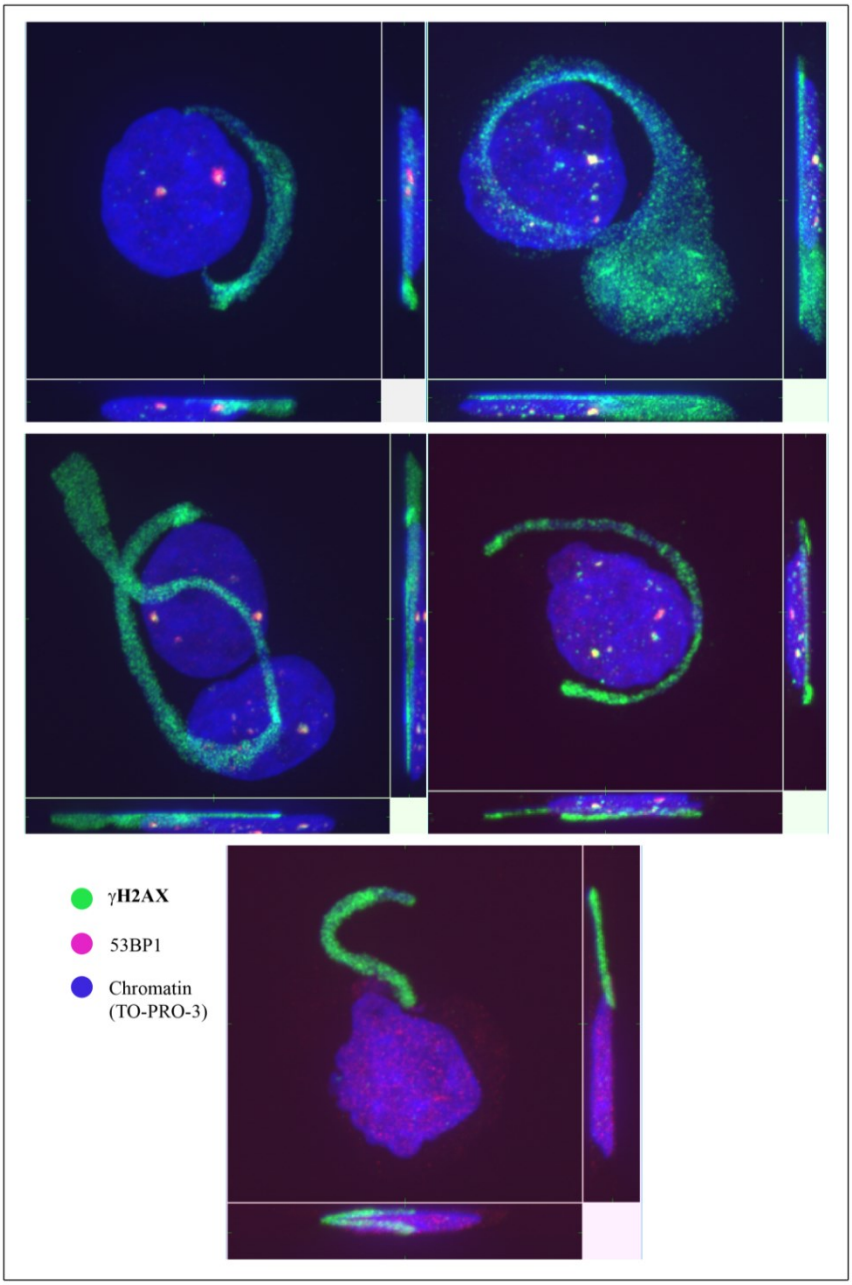

Fig. 3.2.3.5. Major chromatin perturbations caused by freeze/thaw processes and marked by γH2AX. The γH2AX-positive chromatin is extracted out the nuclei. Visible is also altered (decondensed) higher-order chromatin structure (blue, TO-PRO3) while DSBs (colocalized γH2AX and 53BP1 signal, green + red) are detected in the extent corresponding to never frozen cells. Images consist of 40 superimposed 0.2 µm thick confocal slices; magnification 100×).

To thoroughly examine important source of defects in epigenome maintenance in frozen/ thawed cells cultured in standard medium or in media containing cryoprotectants (DMSO, trehalose, AFP, trehalose+DMSO **Tab. 2.2.3.2.1.**), we investigated higher-order chromatin structure: chromatin domains, chromatin condensation and degradation before and after freezing/thawing (-80°C; rate of -1°C/min). Also, to evaluate just the effects of chromatin condensation on cell survival we studied the impact of a short pre-freezing incubation of cells in media with different osmolarities (hypertonic, hypotonic and isotonic).

To clarify the relationship between chromatin state and viability of cells upon freezing/thawing, we statistically quantified changes in nuclei for each cryoprotectant and compared them with cell viability assessed by flow cytometry (**Tab. 3.2.3.3**). We performed these measurements at 30 min and 24 hours post-thaw to evaluate immediate cell damage by freezing/thawing and to potentially observe additional cells dying from delayed apoptosis, respectively.

Table 3.2.3.3. Correlation between condensed chromatin, determined by confocal fluorescence microscopy (TO-PRO-3 staining) in combination with image 2D Fourier transform, and cell survival quantified by flow cytometry (Annexin V + PI positivity) before freezing and at 30 min and 24 h after thawing. A – NHDF cells; B – MCF7 cells.

A - NHDF cells	Condensed chromatin [% of cells]		Viable cells [%] (flow cytometry)	
treatment:	before freezing/thawing	30 min after freezing/thawing	30 min after freezing/thawing	24 h after freezing/thawing
untreated	16.7 ± 2.9	12.0 ± 2.5	13.9 ± 4.4	22.2 ± 2.1
AFP	25.8 ± 5.1	15.1 ± 4.6	31.5 ± 4.8	35.4 ± 5.3
trehalose	21.1 ± 6.4	43.5 ± 6.9	48.1 ± 5.1	60.3 ± 3.5
DMSO	56.7 ± 9.2	73.2 ± 2.5	68.1 ± 2.2	79.0 ± 7.0
DMSO + trehalose	52.3 ± 6.4	82.5 ± 5.0	69.2 ± 2.5	65.8 ± 2.2

B - MCF7 cells	Condensed chromatin [% of cells]		Viable cells [%] (flow cytometry)	
treatment:	before freezing/thawing	30 min after freezing/thawing	30 min after freezing/thawing	24 h after freezing/thawing
untreated	8.6 ± 2.8	7.9 ± 2.3	0.9 ± 0.2	0.6 ± 0.8
trehalose	12.0 ± 2.2	16.0 ± 2.8	14.3 ± 0.5	9.2 ± 1.0
DMSO	31.6 ± 5.1	59.7 ± 2.8	76.3 ± 1.0	80.0 ± 0.5
DMSO + trehalose	39.5 ± 4.7	62.0 ± 5.8	76.2 ± 1.5	66.5 ± 1.0

The relationship between the state of higher-order chromatin structure (as determined by TO-PRO-3) and γH2AX phosphorylation in frozen/thawed cells was following.

The majority of cells with altered higher-order chromatin structure (based on TO-PRO3 staining) did not express γH2AX. The proportion of these damaged cells (both γH2AX -positive and -negative) varied by the cryoprotectant used, with the highest values for untreated cells and the lowest for cells treated with DMSO (and DMSO+trehalose).

However, a smaller part of the cells with altered higher-order chromatin structure (based on TO-PRO3 staining) also showed pan-nuclear γH2AX signal or γH2AX-stained chromatin perturbations not colocalizing with 53BP1. The chromatin

structure of cells with such pan-nuclear signal was often disrupted in a strong way (extremely condensed apoptotic, decondensed, or totally disintegrated chromatin) (Falk et al. 2018).

To objectively quantify the level and statistical occurrence of chromatin condensation among the observed cell nuclei, in addition to performing visual inspections of chromatin structure in large sets of cells, we calculated a 2D Fourier transform in polar coordinates from a single 2D section (for each analyzed cell). To discriminate nuclei with condensed chromatin, the best criterion appears to be the first momentum of the middle frequency of the Fourier-transformed data component **(Fig. 3.2.3.6)**. The discrimination criterion was 7.5×10^{-6} (where unity is the zero frequency maximum). Typical trehalose- and AFP-treated condensed chromatin cells were close to the boundary defined by the first momentum of the middle frequency of Fourier-transformed data between condensed and standard or disintegrated chromatin, while typical DMSO-treated cells were farther from this condensation border.

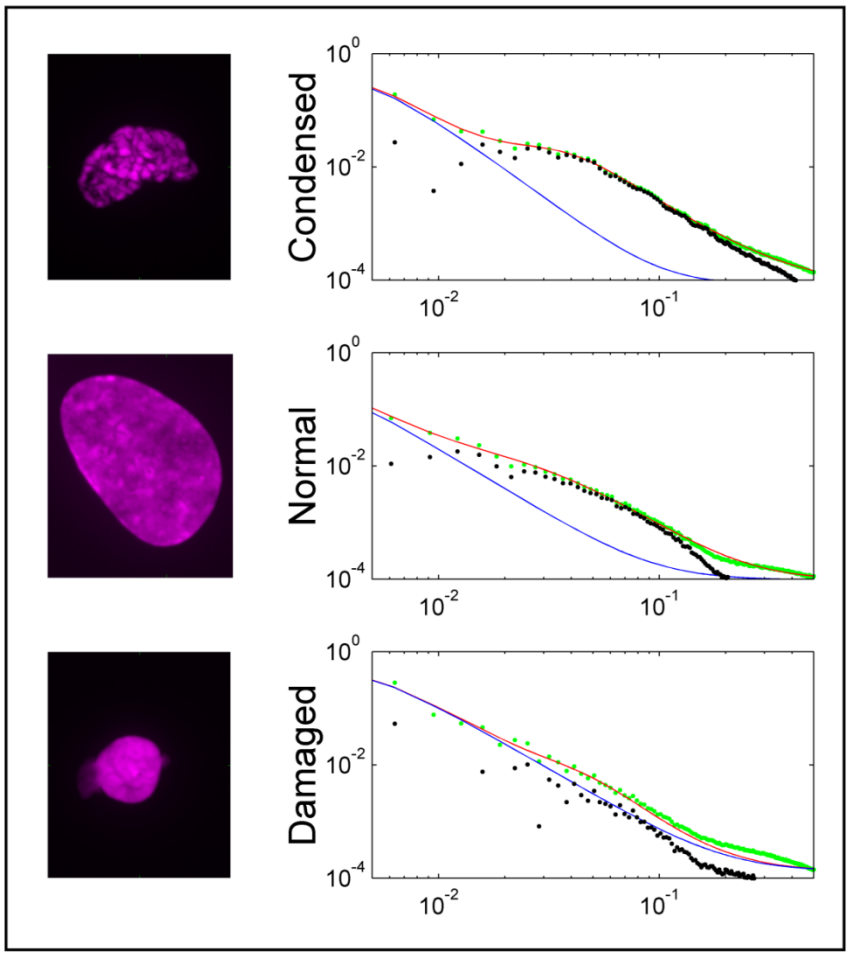

Fig. 3.2.3.6. Examples of nuclei (left) with (top to bottom) condensed, normal, and damaged/structureless chromatin with corresponding radial profile of Fourier transform intensity in log-log scale (right). Green dots are data calculated from the pictures, blue line represents the low-frequency component and the background, red line includes also a middle frequency component. Black dots show the difference of measured data from the blue line.

We analyzed the effects of the cryoprotectants on never-frozen cells (**Figs. 3.2.3.7, 3.2.3.8**). As quantified for NHDF fibroblasts, non-frozen cells incubated with trehalose or AFP typically exhibited slightly condensed nuclear chromatin. By contrast, the application of DMSO to never-frozen NHDF cells caused extensive chromatin condensation. Besides studying the chromatin condensation, we also monitored the shape and integrity of nuclear envelope (lamin A/C staining).

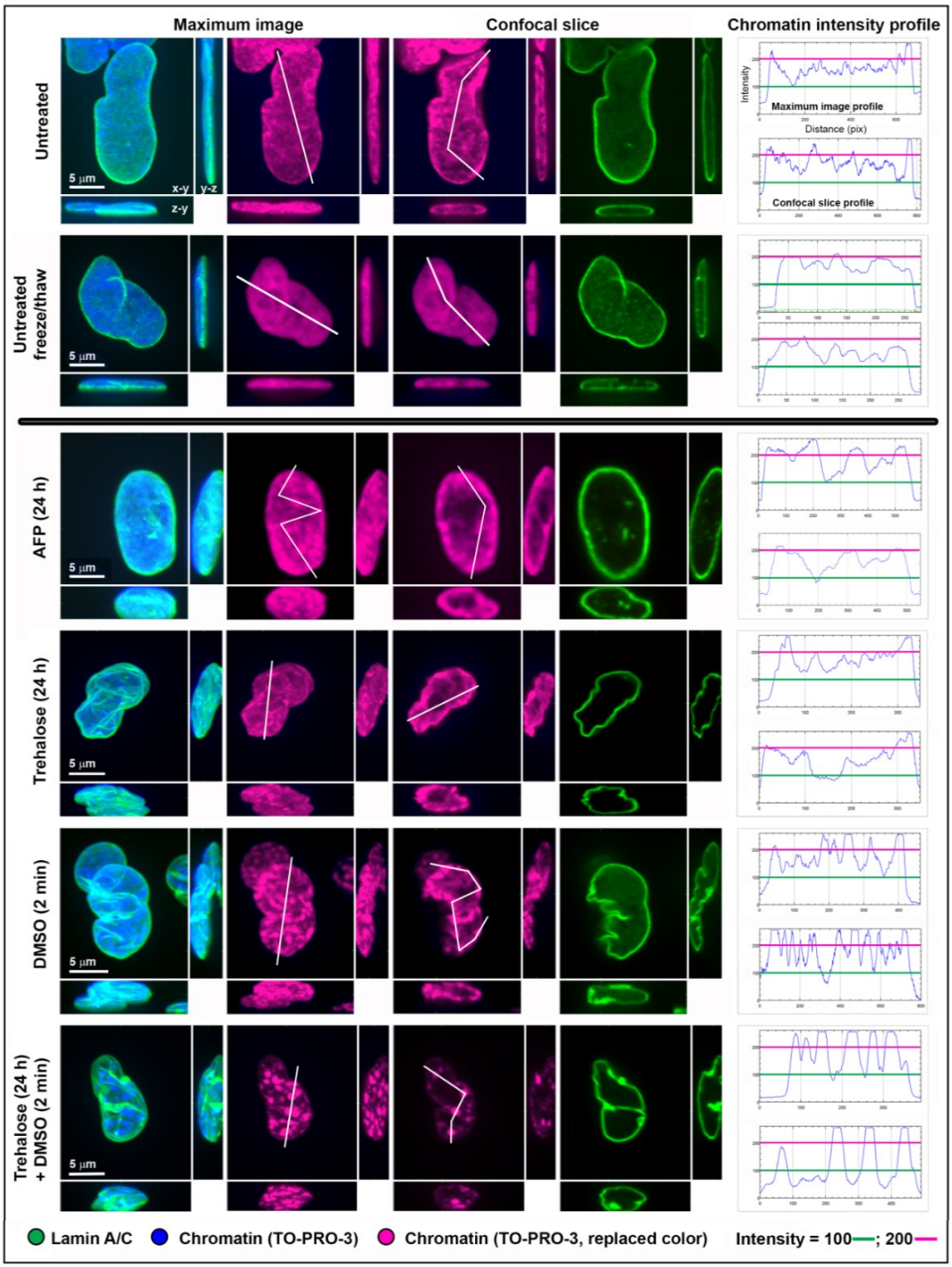

Fig. 3.2.3.7. Effects of a freeze/thaw cycle on the higher-order chromatin structure and nuclear envelope of NHDF fibroblasts in the presence of cryoprotectants. Top row: untreated control cells that were not frozen. Other rows: cells frozen in the presence of the indicated cryoprotectant. 'Maximum images' are composed of 40 superimposed 0.2 µm thick confocal slices and are shown with x-z and y-z projections (1st and 2nd columns from the left). The 3rd and 4th columns of images present single confocal slices (0.2 µm thick) through the central nuclear plane with

x-z and y-z projections. Nuclear envelopes were visualized using lamin A/C antibodies (green), and the chromatin was counterstained with TO-PRO3 (blue or violet to better visualize the chromatin structure). 5th column: intensity profiles of the violet (chromatin) channel along the demarcated paths (white lines) drawn above the maximum images and confocal slices of the cell nuclei. Each profile path was chosen to include nuclear areas with the maximum and minimum chromatin (red) intensity. The intensity profiles show differences in the nuclear chromatin 'texture' and chromatin condensation; “Intensity” [0–255] corresponds to relative fluorescence. Red and green lines, which correspond to intensities of 100 and 200, respectively, are shown to facilitate comparisons.

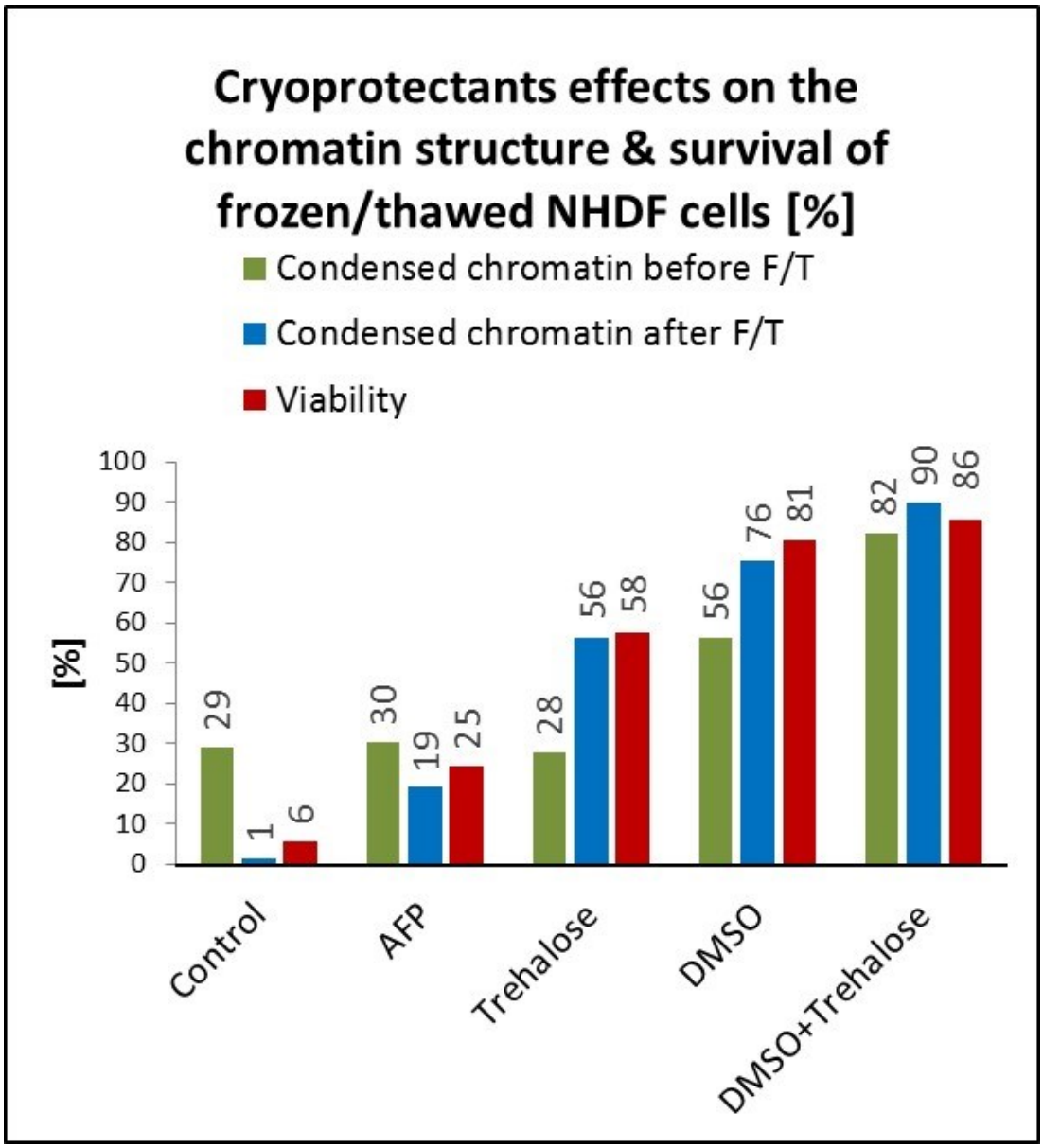

Fig. 3.2.3.8. Effects of cryoprotectants on the chromatin structure of NHDF fibroblasts before and after a freeze/thaw cycle. For frozen/thawed cells, the levels of chromatin condensation were correlated with the cryoprotective effects of cryoprotectants, quantified as the proportion of surviving (24 h after thawing) cells identified by flow cytometry (Annexin V/7-AAD staining). Errors are in all cases less than 3%.

The quantification of NHDF cells with condensed chromatin prior and after freezing, as well as their post-thaw viability, is summarized in **Fig. 3.2.3.8** for each cryoprotectant. Importantly, the post-thaw percentage of chromatin condensation correlates with viability (not only 24 h post-thaw but also 30 minutes post-thaw) very closely. Freezing and thawing of untreated cells causes chromatin damage (disrupted chromatin structure) practically irreconcilable with cell survival - only small percentage of untreated samples survived freezing/thawing. Freezing/thawing caused hypotonic chromatin structure alterations; the majority of chromatin became decondensed to a variable extent.

The proportion of thawed NHDF cells with condensed chromatin constituted 76% and 90% of the total when DMSO and DMSO+trehalose was applied, respectively. More than 75% of the cells survived freezing/thawing with treatment of DMSO whose small molecules are able to enter cell nuclei. Viability of DMSO and trehalose treated thawed cells was 86%. For AFP treatment, the level of post-thaw viability and post-thaw chromatin condensation was around 19% and 25%, respectively (**Fig. 3.2.3.8**). For trehalose treatment, the level of post-thaw viability and post-thaw chromatin condensation was around 56% and 58%, respectively. We also found that DMSO is able to trigger chromatin condensation even prior to freezing, and addition of trehalose further exacerbates this effect.

Fig. 3.2.3.9. shows typical NHDF cell nucleus morphologies observed in the thawed cell samples.

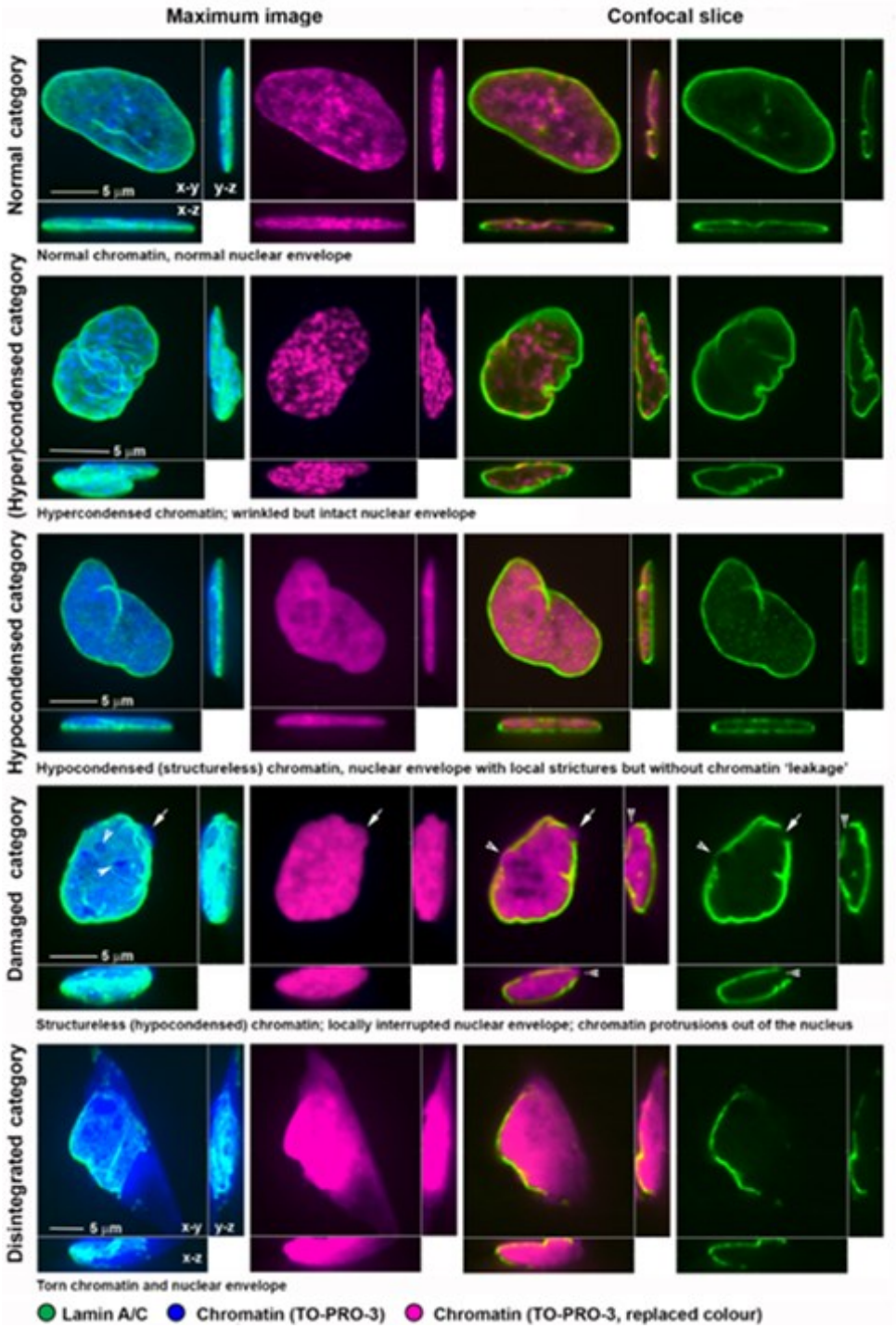

Fig. 3.2.3.9. Cell nuclei after a freeze/thaw cycle, as illustrated by NHDF cells. Top two rows: cells with a high probability of surviving had a normal appearance or hypercondensed chromatin and an intact or wrinkled/shrunken nuclear envelope. Though a small fraction of cells with condensed chromatin may be apoptotic cells, our results show that chromatin condensation was generally correlated with cell survival. Bottom three rows: cells with a low probability of surviving had damaged

nuclei with hypocondensed chromatin and a nuclear envelope with or without local interruptions and chromatin leakage (minimal or no probability of surviving), or a disintegrating nucleus showing leaking chromatin with no structure (no probability of surviving). Two right columns show 'maximum images' composed of 40 superimposed 0.2 µm thick confocal slices; central nuclear confocal slices (0.2 µm thick) are provided in the two left columns; x-y, x-z and y-z projections are displayed for each image. Nuclear envelopes were visualized using lamin A/C antibodies (green), and chromatin was counterstained with TO-PRO3 (blue or violet to better visualize the chromatin structure). Holes in the nuclear membranes are indicated by white arrows (Falk et al. 2018).

Furthermore, the post-thaw levels of chromatin condensation also correspond very well to the percentages of cells with shrunken nuclear envelope (**Fig. 3.2.3.10 b**). However, incubation of non-frozen cells in AFP or trehalose strongly increases nuclear envelope shrinkage without affecting the chromatin condensation levels (**Fig. 3.2.3.10 a**).

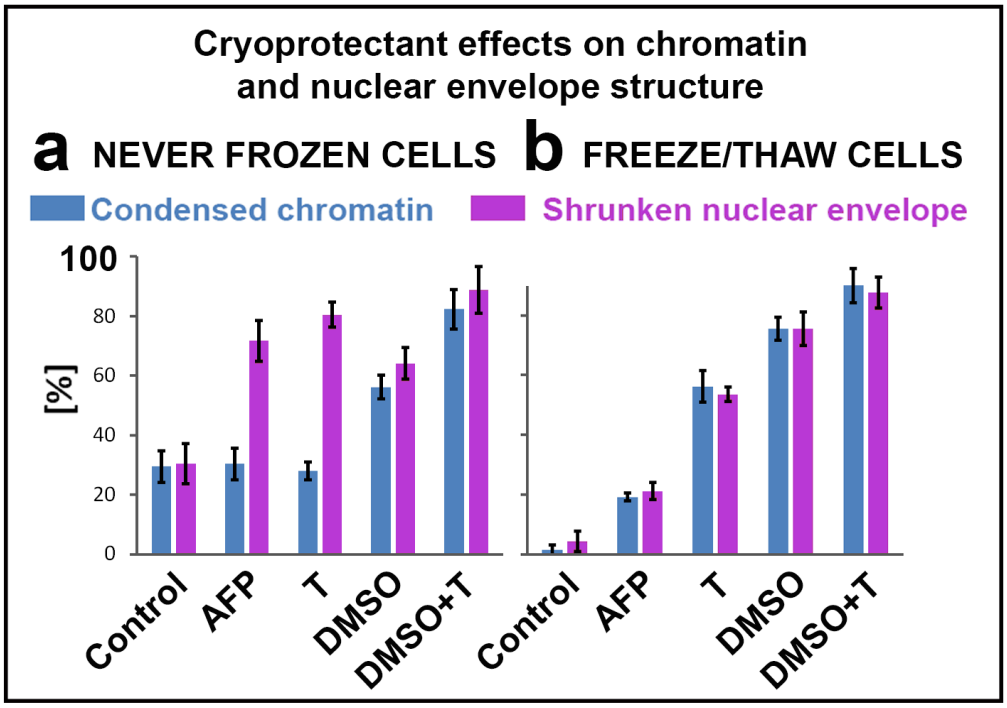

Fig. 3.2.3.10. Effects of cryoprotectants on the NHDF cell nuclei states (their chromatin structure and envelope structure) during (a) pre-freezing incubation and (b) after a freeze/thaw cycle. Error bars indicate SE from three analyses; between 50 and 150 cells were analysed for each sample. For frozen/thawed cells, the levels of nuclear envelope shrinkage and chromatin condensation correlated with the cryoprotective effects of the cryoprotectants.

After thawing, AFP-cryopreserved NHDF cells had the lowest levels of chromatin condensation, nuclei envelope shrinkage and survival (25%) among the cryoprotectants studied (**Fig. 3.2.3.8, Fig. 3.2.3.10**). Due to large molecular size, the effect of AFP is restricted to extracellular space which poses a limit on its effectivity.

Trehalose had an intermediate effect on the frozen/thawed NHDF cells inducing chromatin condensation/envelope shrinkage in 56-57% of the cells, this value being very close to the real cell survival rate (58%) of trehalose-treated cells 24 h after thawing. Importantly, when trehalose was applied for shorter periods of time (4 or 6 h), it provided almost no cryoprotectivity. The survival of NHDF cells was improved only when trehalose was applied for 24 h. This observation indicates that trehalose penetrates the cells, but does so slowly.

To further support this hypothesis, we analysed this phenomenon using LC-MS/MS, DART-Orbitrap and DESI-MS techniques (Falk et al. 2018). The LC-MS/MS results demonstratedand quantified the presence of trehalose in the filtered lysates of both cell types under study (**Fig. 3.2.3.11 A,B)**. DART-Orbitrap successfully confirmed the identity of the trehalose peaks detected by LC-MS/MS (**Fig. 3.2.3.11 C)**. For the NHDF fibroblasts and two trehalose concentrations in the culture medium, we further demonstrated the penetration of trehalose into the intact cells using DESI-MS (**Fig. 3.2.3.12**).

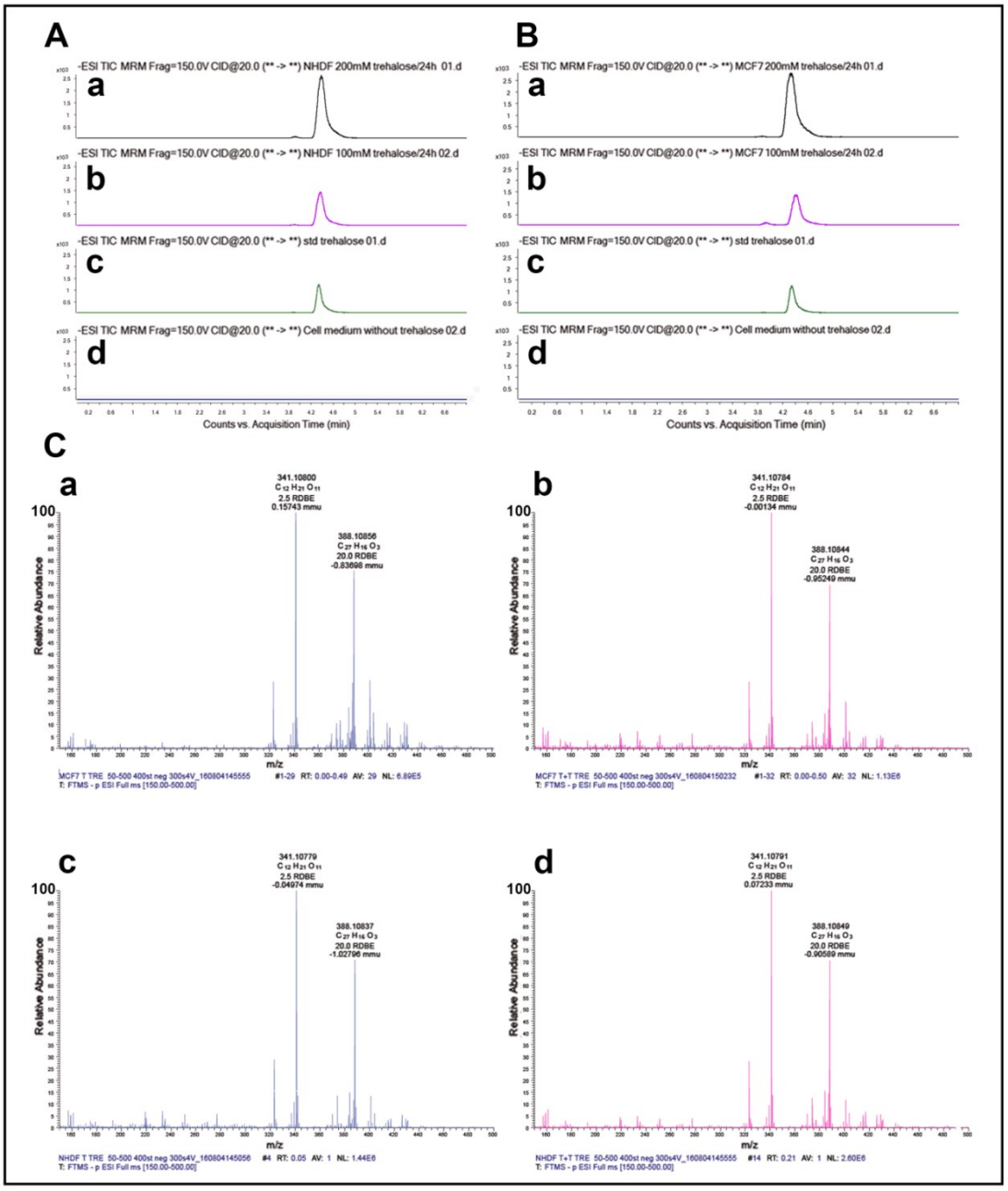

Fig. 3.2.3.11 LC-MS/MS + DART-Orbitrap analysis of trehalose in NHDF and MCF7 cells. A + **B**: Negative ion mode of MRM chromatograms: **a**. NHDF cells with 200 mM trehalose/24 h; **b**. NHDF cells with 100 mM trehalose/24 h; **c**. standard of trehalose; **d**. Cells medium without trehalose **B**. MCF7 cells (a-d as for A). **C**. DART: **a**. MCF7 cells incubated with 100 mM trehalose for 24 h; **b**. MCF7 cells incubated with 200 mM trehalose for 24 h; **c**. NHDF cells incubated with 100 mM trehalose for 24 h; d. NHDF cells incubated with 200 mM trehalose for 24 h (Falk et al. 2018).

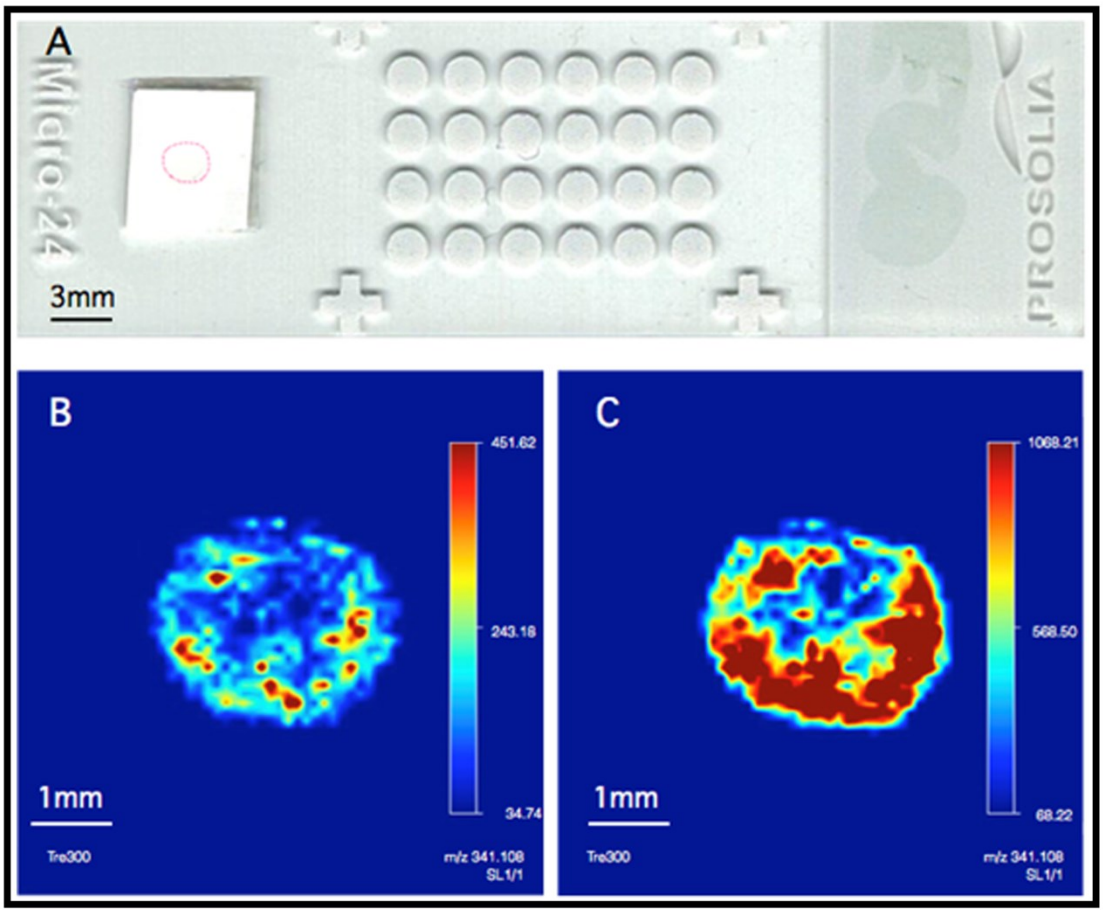

Fig. 3.2.3.12 DESI-MS images showing the cell absorption and relative ion intensity of trehalose (m/z 341.108) by/in NHDF cells. A: Cell culture loaded onto a nylon membrane, fixed to the glass slide by the means of double-site tape**.** Displayed are spots of cells incubated for 24 h with: **B –** 100 mM trehalose; or **C –** 200 mM trehalose. Trehalose is being absorbed by cells in the time course of our experiments; blue-to-red scale indicates increasing concentrations of trehalose in cells (Falk et al. 2018).

In parallel, the same experiments done with NHDF cells (pre-freeze and post-thaw levels of viability, chromatin condensation and nuclear envelope shrinkage) were also performed with MCF7 cells. Comparing the results of MCF7 cell survival after freezing/thawing with the data on nuclear state changes, with or without cryoprotectant treatment, provided similar results as those of NHDF fibroblasts. Correlations between the nuclear envelope structure, chromatin structure, and cell viability for NHDF fibroblasts and MCF7 cells, both prior to and after freezing/thawing, in the presence or absence of cryoprotectants, are compared in **Fig. 3.2.3.13.**

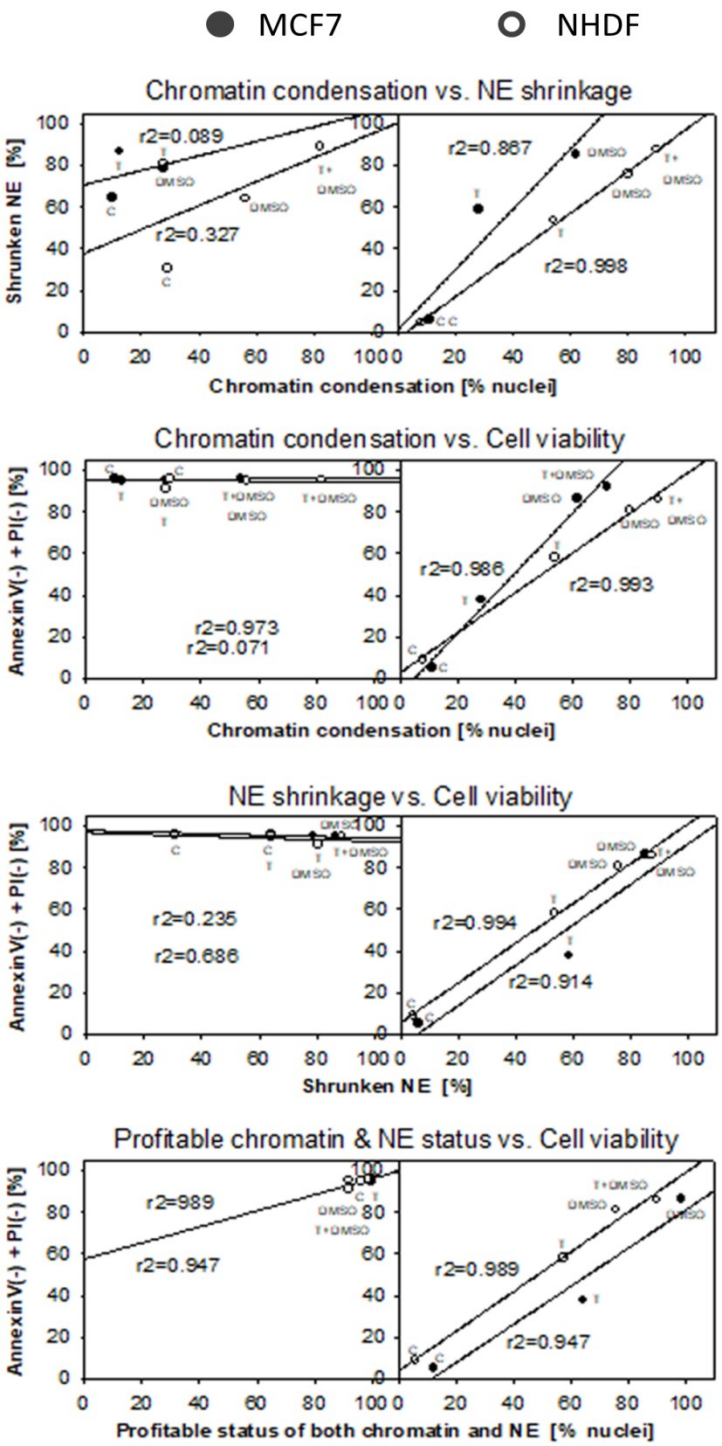

Fig. 3.2.3.13. Correlations between structural parameters of the nuclear envelope, chromatin structure, and cell viability compared for NHDF fibroblasts and MCF7 cells prior to and after freezing/thawing of cells in presence or absence of cryoprotectants. Parameters of the nuclear envelope and chromatin structure were determined by high-resolution confocal microscopy immediately after thawing, cell viability 24 h later (to allow detection of apoptotic cells) by flow cytometry with Annexin V + PI.

The chromatin condensation in MCF7 cells was less visually obvious than in NHDF fibroblasts (treated with the same cryoprotectant), but clearly resulted in a significant decrease in nuclear size after freezing/thawing. In principle, the correlation between chromatin condensation and viability of thawed MCF7 cells was similar as in the case of thawed NHDF cells.

We conclude that the viability of NHDF and MCF7 cells upon freezing/thawing is strongly correlated with chromatin structure and nuclear envelope shrinkage (**Fig. 3.2.3.13**). Chromatin condensation is influenced by cryoprotective compounds to varying extents. Replicating (S-phase) and non-replicating cells both suffer from non-DSB chromatin damage (i.e., secondary chromatin fragmentation in cells with disintegrated or apoptotic nuclei), which can be efficiently reduced by DMSO and to a lesser extent by trehalose.

To evaluate the effects of chromatin condensation on cell survival from freezing/thawing separately from the other effects of cryoprotectants, we studied the impact of a short pre-freezing incubation of cells in media with different osmolarities (hypertonic, hypotonic and isotonic) on the higher-order chromatin structure, and cell viability - **Fig. 3.2.3.14.** The frozen/thawed cells treated with hypertonic medium showed the strongest chromatin condensation and the highest (approximately 40%) cell viability compared to other osmolarities. On the other hand, the hypotonic pretreatment of non-frozen cells induced slight chromatin hypocondensation compared to the isotonic pretreatment. Upon freezing/thawing, the viability of the hypotonic-treated cells was similar to that (below 10%) of the cells frozen/thawed in normal (isotonic) medium.

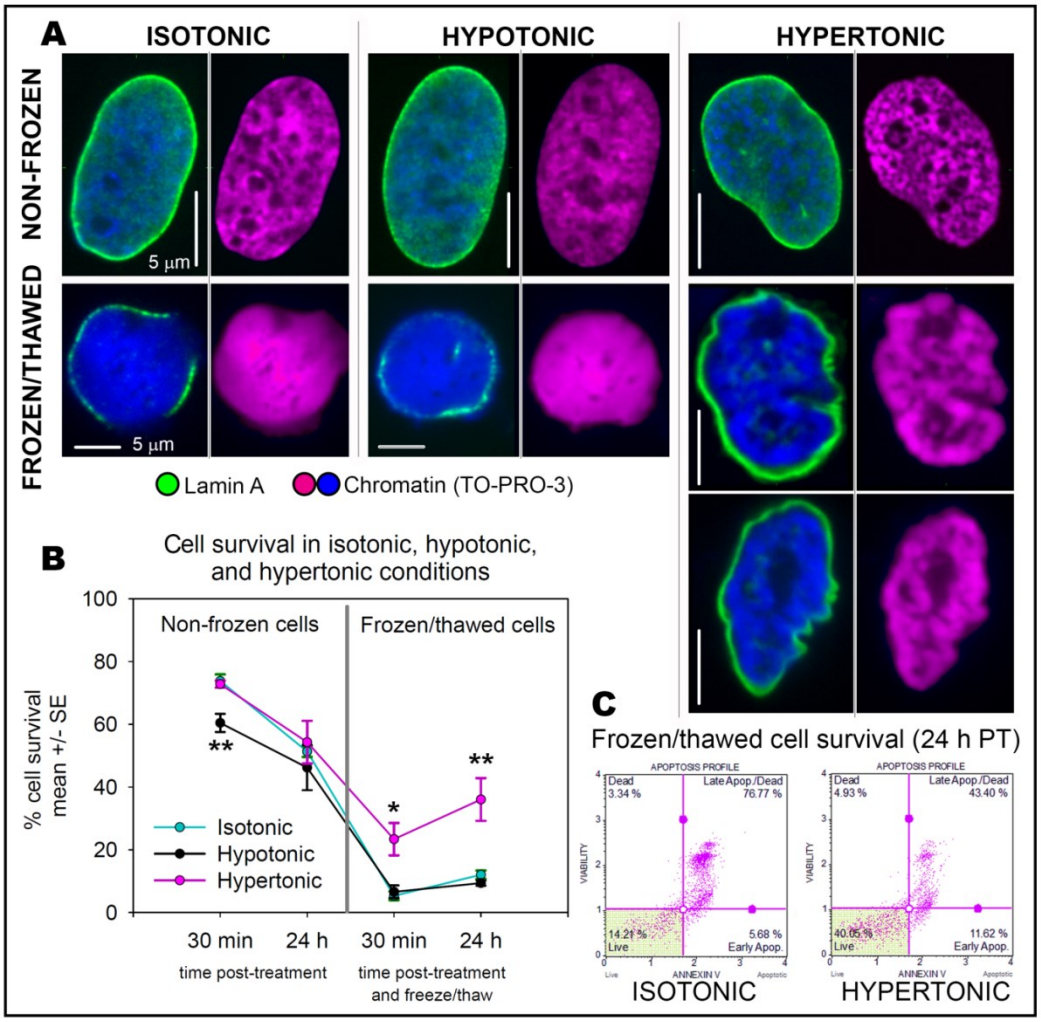

Fig. 3.2.3.14. Impact of short pre-freeze incubation of NHDF cells in media with different osmolarities on higher-order chromatin structure, nuclear envelope quality and cell viability. Before freezing, cells were incubated for 12 min in hypertonic (570 mOsm), hypotonic (140 mOsm), or normal culture medium (isotonic control, 290 mOsm). (A) Higher-order chromatin structure and nuclear envelope quality of non-frozen (top line) and frozen/thawed skin fibroblasts (NHDF), determined by high-resolution confocal immunofluorescence microscopy immediately (without changing the media) after the incubation or after the incubation and freezing/thawing. Nuclear envelopes were visualized using lamin A/C antibodies (green), and the chromatin was counterstained with TO-PRO-3 (blue or purple to better visualize the chromatin structure). (B) Viability of control NHDF (isotonic medium) and NHDF pre-incubated for 12 min in hypotonic or hypertonic

medium before and after a freeze/thaw cycle as determined by flow cytometry (see C). After freezing/thawing, cells were transferred to normal (isotonic) medium and cultured for 30 min or 24 h before viability was assessed. Error bars correspond to the SE; statistically significant (unpaired two-tailed t-test) differences relative to control (isotonic) cells are indicated by asterisks (*, $P < 0.05$; **, $P < 0.01$; ***, $P < 0.001$). (C) Representative flow cytograms for NHDF cells that were frozen/thawed in isotonic (left) and hypertonic (right) medium. Horizontal axis: Annexin V staining, vertical axis: 7-AAD staining (bottom-left corner contains viable cells).

4 Discussion

In this work, we deepened the current understanding of the cryopreservation process both at physical and biological level. We described the freezing process and properties of aqueous solutions of studied cryoprotectants (DMSO, trehalose and antifreeze protein ApAFP752) using computer simulations, Raman spectroscopy, Differential Scanning Calorimetry and X-Ray Diffraction. These results were correlated with the viability of cells frozen/thawed in the respective cryoprotective solutions, with the impact of cryopreservation on the stiffness of thawed cells (measured by AFM) and with the post-thaw state of cell nuclei studied by fluorescence microscopy (higher-order chromatin structure, formation of DNA double-strand breaks, nuclear envelope integrity).

4.1 Impact of studied cryoprotectants on the process of liqiud/solid phase transition

Ability to altering the physical conditions of the liquid/solid phase transition inside the cells or in their proximity is an important attribute of materials that confer cell cryoprotection. One important reason for death of frozen cells is the direct membrane damage caused by the increase of ice volume. In our work, ice crystal size in frozen solutions was quantified (using XRD) and correlated with theoretical models (DFT, MD). The results were complemented by Raman spectroscopy and DSC measurements. Influence of cryoprotectants on the ice constitution was then correlated with post-thaw viability of cells cryopreserved by slow freezing.

The diameter of ice crystallites was greatest in frozen water (without cryoprotectants) so all cryoprotectants in this study more or less efficiently suppressed the ice crystal growth (as shown by XRD). The mean crystal sizes in frozen 10% (w/w) DMSO solution (with or without 3.2% (w/w) trehalose) were smaller than ice in frozen water. The smallest diameter of ice crystallites was detected in frozen 1% (w/w) AFP, where the size of ice crystals was even smaller

than in frozen 10% (w/w) DMSO. Ice crystals in frozen 3.2% (w/w) trehalose solutions were biggest from all frozen cryoprotective solutions (half in size compared to frozen water).

As seen by Raman spectroscopy and DSC, DMSO and trehalose in PBS solutions prevented water from forming eutectic mixture (ice and hydrohalite). In frozen AFP solutions, the eutectic mixture was formed.

During the melting process of the frozen solutions, the large crystals present in 1% (w/w) AFP and trehalose (41% w/w) frozen solutions were melted continuously to small crystals. In DMSO-containing frozen solutions, the larger crystals grow and smaller crystals diminish - this is a sign of the ice recrystallization proces (possible source of further cell damage). When 3.2% trehalose is present in the 10% DMSO solution, the recrystallization is suppressed.

The modelling studies showed that DMSO, which has an oxygen atom with a strong negative charge and a sulphur atom with a strong positive charge (and correspondigly a large dipole moment), influencesstrongly the dynamics of water (a material with high permittivity), and consequently also its freezing process. In addition, water molecules near the DMSO methyl groups cannot form alternative hydrogen bonds with DMSO, which affects their interactions with other water molecules and also ice formation. DMSO molecules homogeneously distributed in solution (forming practically no clusters) have a long-range effect on water dynamics, affecting the thermodynamics of the solution. In other words, DMSO molecules strongly change the conditions for water freezing in the entire volume, which results in the formation of small ice crystals.

Trehalose, due to its high inter-molecular interaction potential can easily form cluster structures containing dendritic crystals and possibly also an amorphousglass phase. Trehalose impacts neighbouring as well asremote water molecules' dynamics only moderately. In solutions in which trehalose concentrations were relevant for biological applications (3.2% w/w) ice crystal sizes were biggest from all cryoprotectants solutions.

AFP had the strongest influence on the neighbouring water molecules hydrogen bond dynamics (short-range effect). This is mainly caused by the fact that AFP is a large and less mobile molecule with abundant hydroxyl groups on the surface. AFP, attached to the ice crystal surface, inhibits ice crystal growth. This results in the smallest ice crystals observed in 1% (w/w) AFP solutions.

In our case, the cells were frozen slowly (using a gradient of -1°C/min) and therefore dehydrated rapidly enough to eliminate critical supercooling. In such dehydrated state, intracellular freezing is supressed. As cryoprotectants affect the volume of ice crystals, they influence the direct damage caused to cell membranes and therefore also the viability of the frozen/thawed cells. Small DMSO molecules enter intracellular space, effectively decrease ice crystal size and strongly improve cell viability after freezing/thawing (81% of DMSO-treated cells survived the freezing/thawing treatment). The protective effect of large ice-blocking AFP molecules was smaller compared to DMSO, as only 32% of AFP-treated cells survived the freezing/thawing treatment. The effects of trehalose treatment were observable only after 24 h of incubation: 58% of trehalose-treated cells survived freezing/thawing. Of all cryoprotectants under study, trehalose has the smallest impact on ice crystal size. Trehalose probably acts as a natural osmolyte (osmoprotectant), and also stabilizes phospholipid membranes and the tertiary structure of proteins (Corradini et al. 2013; Kent et al. 2014). The highest cell viability was observed when a mixture of DMSO+trehalose was applied: 86% of DMSO+trehalose-treated cells survived the freeze/thaw.

To summarize, we showed that DMSO and AFP have such impact on their solutions‘ freezing process that ice crystallinity size is considerably reduced. This contributes to parameters that can affect viability of cryopreserved frozen/thawed cells. DMSO is homogeneously distributed in solution (forms no clusters) and has a long-range effect on bulk water dynamics. DMSO molecules are able to enter both extra and intra cellular space, effectively change the condition for freezing and strongly improve frozen/thawed cells viability. AFP has an appreciable (although not large) cryoprotective effect despite not entering the cells due to its large molecular size. The best viability results were obtained when combination of DMSO (able to

strongly change the freezing process, even intracellularly) and trehalose (able to stabilize phospholipid membranes and the tertiary structure of proteins) were applied.

4.2 Mechanical properties of cryopreserved cells surfaces

The mechanical and elastic properties of cells are closely related to their functions. Monitoring the mechanical stiffness of living cells can, therefore, provide a novel way to monitor cell physiology, detect and diagnose diseases, and evaluate the effectiveness of drug treatments. We were the first to study cryopreserved cells' stiffness regeneration process using atomic force microscopy (AFM) nano-indentation method.

Firstly, surface stiffness of never frozen fibroblasts was studied by AFM upon the application of cryoprotectants. We found that higher concentrations of glycerol/DMSO decreased the fibroblast stiffness, with similar changes in the average stiffness values (i.e. cell surface softening) provoked by both cryoprotectants. However, DMSO caused lower surface adhesion of the cells than glycerol.

After that, AFM nano-indentation was used to map cellular reconstitution in real time after freeze/thaw cycle, and to differentiate the regeneration processes at different depths of the cell and even at different parts of the cell surface. Two AFM approaches were used to study stiffness of cryopreserved cells (non-irradiated and irradiated fibroblasts) after freezing/thawing: 1. a higher SP value (i.e., 1 nN, 100x100 μm^2 area) provided information about the inner parts of the cell, 2. a low SP value (i.e., 0.4 nN, 10x10 μm^2 area) allowed us to study cell stiffness closer to the membrane. The irradiated fibroblasts were used as a control group in which regeneration processes are disabled.

Increase of stiffness measured by low SP AFM, which was related to regeneration of the membrane and sub-membrane structures, begun 2.7 hours after cell plating. Applying a high SP value on 100x100 μm^2 area, we found that the

stiffness of the high sample parts decreased after thawing, reaching remarkably lower values than stiffness of the low and middle parts of the sample. Since the high part contained the cell nucleus, this observation most probably reflected changes in the nucleus state, in addition to states of the cell cytoskeleton and membrane. This was supported by the nuclear envelope shrinkage, recognized in ~80% of the frozen and thawed cells as measured by confocal microscopy. After 1.5 hours, the interaction of cell with the substrate was gradually built and cell stiffness and height significantly decreased. Six hours after plating, the reconstruction of the inner parts of the cell probably begun as cell height decreased and cells stiffness significantly increased. Change of frozen/thawed cells stiffness (measured by both high and low SP AFM) was much less pronounced in mitotically inactivated IR fibroblasts. This observation can be explained by only marginal regeneration of membrane, sub-membrane and inner parts of IR cells.

AFM nano-indentation allowed us to measure in both time and space the mechanical properties at different depths of cryopreserved cells (membrane, sub-membrane and inner parts) following a freeze/thaw cycle. Thus, the AFM was able to reveal changes in stiffness and height, unfolding in thawed cells after plating.

Using AFM, we also compared stiffness of DMSO- or PEG-treated cryopreserved cells. The used cryoprotectants were of two types: penetrating both cell membrane and nuclear membrane (DMSO) or not penetrating either membrane (PEG-1500). The median stiffness of PEG-treated frozen and thawed cells was lower compared to DMSO-treated cells. PEG-treated cells were more round and taller immediately after thawing, with homogeneous spatial distribution of stiffness.

On the contrary, DMSO treated cells had considerably higher viability after thawing than PEG treated cells and cryopreserved stiffness maps of thawed DMSO-treated cells were not homogeneous. Immediately after thawing, DMSO-treated cell nuclei are typically the softest part of the cells. The cytoskeleton is also clearly distinguishable in the modulus maps due to its comparatively higher stiffness. During 4 hours after thawing, the spatial variation of stiffness of the

DMSO-treated cells' surface gradually decreased. The median of the DMSO-treated cryopreserved cells stiffness is higher than PEG-treated cryopreserved cells.

To summarize, we showed that AFM can be used as an *ex vivo* technique for the investigation of cryopreserved cells' surface state and development. Our results offer a new perspective on the monitoring and characterization of frozen cells' recovery by measuring their elastic response to external mechanical stimuli. This may lead to a new, detailed and chemically non-invasive way of investigating the post-thaw development of cryopreserved cells which allows to distinguish between different cell parts. We demonstrated that AFM can be used as a non-invasive method to find cells that regenerate their mechanical properties with the proper dynamics after thawing. This can be important in the area of assisted reproduction (e.g. monitoring of oocyte regeneration after freezing/thawing).

4.3 Critical defects in nuclear structures of cryopreserved cells nuclei (envelope disruption, chromatin condensation, DNA breaks)

In this work, we correlated cell viability with frozen/thawed cells' DNA integrity defects (possibly leading to double strand breaks) and chromatin state as explored by high-resolution confocal fluorescence microscopy and flow cytometry. We are the first to identify novel critical types of chromatin damage, shedding new light on the mechanisms of freeze-thaw-induced chromatin damage, consequent cell survival, and cryoprotection.

DNA double strand breaks (DSBs) represent the most serious DNA lesions but their induction through the freeze-thaw process remains controversial. We have shown that freezing and thawing preferentially damages replicating (S-phase) cells by causing the collapse of their replication forks (which later possibly leads to the formation of DSBs), thereby making rapidly dividing cells more sensitive to cryodamage. S-phase cells aside, we found that the freeze-thaw process does not directly induce DSBs; instead, it alters cells' higher-order chromatin structure. The results of the present study, which was performed on normal human skin fibroblasts (NHDFs) and mammary carcinoma cells (MCF7s), significantly enhances our understanding of the freezing process and its impacts on normal and cancer

cells, which can contribute to the future rational design of cryofunctional materials and cryotherapy.

With regard to DNA double strand breaks, we identified 14% MCF7 and 9% NHDF of frozen/thawed cells that contained enhanced numbers of γH2AX/53BP1 foci. Importantly, these cells contained about 30 to 200 γH2AX/53BP1 foci/nucleus. We found that cells with >30 γH2AX/53BP1 foci per nucleus represent replicating (S-phase) cells with collapsed replication forks. Therefore, freezing these cells may potentially lead to DSB formation, causing genetic defects (Khurana and Oberdoerffer 2015). The patterns of γH2AX/53BP1 foci in frozen/thawed cell nuclei visually correspond to patterns of replication sites in S-phase cells (in terms of numbers and spatial distribution).

The proportion of frozen/thawed NHDF and MCF7 cells with >30 γH2AX/53BP1 foci/nucleus was analyzed for various cryoprotectant treatments. DMSO treatment did not have a significant effect on either the proportion of total S phase cells or the number of S-phase cells with >30 γH2AX/53BP1 foci/nucleus. In contrast, long (24 h) trehalose treatment inhibited cell division, i.e., decreased the total fraction of S-phase cells compared with that of untreated or DMSO-cryopreserved NHDF and MCF7 cell samples, even prior to freezing. To the same extent, trehalose also reduced the number of cells with >30 γH2AX/53BP1 foci/nucleus after freezing/thawing. This observation further confirms that cells with >30 γH2AX/53BP1 foci/nucleus were in S-phase and suggests that collapse of replication forks during freezing/thawing cannot be prevented by any of the cryoprotectants studied.

In addition, the reduced incidence of cells with >30 γH2AX/53BP1 foci/nucleus among normal NHDF fibroblasts after freeze/thaw likely reflects their lower replication activity relative to cancerous MCF7 cells. As freezing/thawing preferentially (more seriously) damages S-phase cells, rapidly dividing (tumor) cells are probably more sensitive to DNA cryodamage. To the best of our knowledge, this finding has not yet been reported.

Next we investigated changes in (epigenetic) chromatin structure as potentially another form of DNA damage in NHDF and MCF7 cells that had undergone a freeze/thaw cycle. Interestingly, we found that across all cryoprotective treatments, post-thaw levels of chromatin condensation correlated very well with cell viability. For cells with no added cryoprotectants (frozen in cultivation medium), freezing/thawing caused hypotonic chromatin structure alterations; the majority of chromatin became decondensed to a variable extent. In contrast, DMSO stimulated chromatin condensation already in never-frozen NHDF and MCF7 cells, in accordance with their similar viabilities after freezing/thawing. Therefore, we propose that condensed chromatin state reduces damage to chromatin structure in the early phase of freezing and prevents the loosening/dispersion of chromatin during the hypotonic shock presented by cell rehydration during thawing. The lower tendency of MCF7 cells to form condensed chromatin compared to NHDF fibroblasts may be explained by a different level of native chromatin condensation in untreated, never-frozen NHDF and MCF7 cells (Liu et al. 2015a). AFP and trehalose had only minor effects on chromatin condensation prior to freezing/thawing, because trehalose molecules do not penetrate into the nucleus and large AFP molecules protects the cells only from extracellular space; which correlated with less condensed chromatin state and lower cell survival after the freeze/thaw cycle. Our results thus suggest that chromatin condensation plays a role in protecting cells against damage during the freezing/thawing processes.

To directly test the importance of chromatin condensation on the viability of frozen/thawed cells, separately from any additional effects of cryoprotectants, we treated NHDF cells with hypertonic and hypotonic medium prior to freezing/thawing. The hypertonic treatment (condensed chromatin), but not the hypotonic treatment (decondensed chromatin), significantly reduced the adverse effects of freezing/thawing on NHDF cells.

We propose that the condensed chromatin state reduces damage to chromatin structure in the early phase of freezing, minimizes freeze-mediated nuclear envelope rupture and prevents the loosening/dispersion of chromatin

during the hypotonic shock presented by cell rehydration during thawing. Further chromatin condensation that occurs as a consequence of freezing *per se* is related to dehydration of the nucleus and chromatin, which leads to an increase in the intracellular concentration of ions. This condition in turn likely further stabilizes the condensed chromatin state. Since condensed chromatin is largely surrounded by neighboring chromatin molecules and chromatin-bound proteins, it is better physically protected from the destructive effects of phase transition (e.g. change in solvation shell followed by denaturation), and thus its integrity is preserved. Concerning the protective effects of chromatin condensation in cells, we therefore hypothesize that the dynamics of the dehydration of nuclei during freezing is important.

4.4 Influence of selected cryoprotectants on cryopreserved cells state

The cryoprotectants studied in this work differ significantly in their ability to permeate cell membrane and nuclear envelope, which in turn determines their osmotic properties and ability to interact with individual cell components. On the level of cell nucleus, we were particularly interested in the impact of cryoprotectants on the degree of chromatin condensation since we observed that cells with strongly condensed chromatin prior to freezing had the highest rate of survival after freezing.

The small DMSO molecules penetrate into cells and accumulate within the cytoplasm and the nucleus (Dong et al. 2010). The penetration of DMSO into nuclei may thus explain the considerable increase in chromatin condensation and nuclear envelope shrinkage observed in frozen/thawed DMSO-treated cells. Concerning the high survival rate of the DMSO-treated cells (81% and 86% for NHDF and MCF7 cells, respectively) during freeze/thaw processes, we propose that DMSO protects frozen/thawed cells at least in two ways. First, DMSO in the intracellular and extracellular space can significantly alter the ice crystallization process, leading to smaller ice crystals. Second, DMSO causes chromatin condensation (already during incubation, prior to freezing), probably stabilizing higher order chromatin structure

and making the DNA less prone to ice-mediated damage, which then supports DMSO-cryopreserved cells viability.

The lower tendency of MCF7 cells to form condensed chromatin compared to NHDF fibroblasts may be explained by a different level of native chromatin condensation in untreated, never-frozen NHDF and MCF7 cells.

AFP and trehalose had only small effects on chromatin condensation prior to freezing/thawing. This may be because neither the large AFP molecules nor trehalose molecules can penetrate into the nucleus, in contrast to DMSO. AFP acts as a cryoprotectant only in the extracellular space. But since trehalose does slowly enter the cytoplasm (shown by DESI-MS in this work), it can also protect cells from freezing/thawing by supporting the dehydration of the cell nucleus, and thus also promoting chromatin condensation in the initial phase of freezing.

The collapse of replication forks that we observed in frozen/thawed S-phase cells (both NHDF and MCF7) was not prevented by either DMSO or trehalose. An active replication fork is a highly complex and vulnerable structure which perhaps simply can't be protected from damage and subsequent collapse caused by slow freezing, regardless of the cryoprotectant used. Currently, the best strategy is to avoid freezing S-phase cells.

In addition to replication fork collapse, both replicating and non-replicating cells suffer from non-DSB chromatin damage (i.e., secondary chromatin fragmentation in cells with disintegrated or apoptotic nuclei) which can be efficiently reduced by DMSO and to a lesser extent by trehalose. Although the penetrating DMSO delivers the best cryoprotective effect in our experiments, post-thaw viability can also be positively influenced entirely from the extracellular space, as evidenced by the cryoprotectivity of the ApAFP752 protein. It may be by changing the osmotic pressure of the solution (we show that hypertonic freezing solution also increases post-thaw viability, see **Fig. 3.2.3.14**) which in effect also leads to nucleus dehydration and chromatin condensation. Also, extracellular cryoprotectants are able to help stabilize cell membranes (as is the case with

trehalose (Krasteva et al. 2001)) and change the crystallinity the cell suspension in solid phase (as suggest our results on ApAFP752 – **Fig. 3.1.3.1**).

Finally, we show that cryoprotectants affect the mechanical properties of cells and their post-thaw repair process in a cryoprotectant-dependent manner., and that AFM can be used to monitor these changes. Presence of DMSO or glycerol in the cultivation medium decreases cell stiffness proportionally to concentration of these cryoprotectants. As only DMSO seems to gradually weaken cell adhesion to substrate, the observed decrease in stiffness (similar for both cryoprotectants) is likely independent thereof and reflects actual changes in the membrane and submembrane cell region. After cell thawing and plating, AFM is able to follow the changes in cell stiffness related to cell reconstruction and cell cycle in a chemically noninvasive way. Compared to DMSO, cells frozen/thawed in PEG-1500 take twice as long to adhere, their stiffness is lower and more spatially homogeneous. DMSO-cryopreserved cells tend to have softer nuclear region (possibly related to the observed shrinkage and wrinkling of cell nuclei) while their cytoplasmic region is stiffer and contains more clearly distinguishable cytoskeletal features. The observed elastic heterogeneity of DMSO-cryopreserved cells is likely the result of DMSO's ability to permeate cell membrane and directly protect intracellular structures (unlike PEG-1500).

5 Summary & Outlook

In this work, we correlated the physico-chemical properties of selected cryoprotectants, their impact on the constitution of ice (physical point of view) and their effects on the condition and viability of frozen/thawed cells (biological point of view). We were the first to simultaneously evaluate the changes in DNA integrity, chromatin higher-order structure, nuclear envelope integrity and surface stiffness of cells frozen/thawed in solutions containing various cryoprotectants.

Firstly, as size of ice crystals is one of the parameters that play a role in the cryopreservation process, we focused on proper description of this phenomenon and correlated crystallinity of cryoprotectant solutions with their cryoprotective effectivity (post-thaw cell viability). To explain in detail the influence of antifreeze protein ApAFP752, DMSO and trehalose on the freezing process, molecular dynamics, Raman spectroscopy, X-Ray Diffraction (XRD) and Differential Scanning Calorimetry (DSC) were employed. We showed that the presence of DMSO, trehalose and ApAFP752 affects the phase transition so that the size of resulting ice crystallites is reduced. This effect in our case correlates with increased viability of cells cryopreserved with the respective cryoprotectants.

Secondly, we used Atomic Force Microscopy (AFM) in a novel way to map cryopreserved cell topography (height profile) and elastic properties over time after thawing. Thus, AFM allowed us to study cellular surface reconstitution in real time after a freezing/thawing, and to monitor the regeneration processes at different cell indentation depths of the cell and even at different parts of the cell surface (nuclei, edge). The differences in thawed-cell recovery after respective cryopreservation with DMSO (permeating) and PEG-1500 (non-permeating) could be clearly seen.

Thirdly, using fluorescence microscopy, we looked for evidence of nuclear alterations resulting from cryopreservation. We found that incubation with cryoprotectants and the process of cryopreservation have diverse effects on the higher-order chromatin structure (condensation) and nuclear envelope shrinkage. Interestingly, our results show that the post-thaw level of chromatin condensation of cells cryopreserved in the respective cryoprotectants is closely correlated with

their survival rate (post-thaw viability), with the highest level of both achieved with a mixture of DMSO and trehalose. We suggest that since condensed chromatin is largely surrounded by neighboring chromatin molecules and chromatin-bound proteins, it is better protected from the detrimental effects of a phase transition, and thus its integrity is better preserved.

Moreover, for the first time, we described a new type of chromatin damage associated with freezing/thawing. It is specific to S-phase cells and cannot be prevented by any of the cryoprotectants used in this study. The damage consists of extensive collapse of the replication forks, which may be potentially converted into double-strand breaks (DSBs) (Berti and Vindigni 2016; Jones and Petermann 2012; Techer et al. 2017). This type of damage is serious and likely lethal, but it cannot be ruled out that a fraction of these S-phase cells survives the replication fork collapse. Even in such case, however, complete genome reparation is unlikely (Burrell et al. 2013; Rasmussen et al. 2016; Sarni and Kerem 2017). Such cells therefore pose a danger of DNA defects propagating through the cell population. This scenario is especially worrying in the context of assisted reproduction.

Our experiments showed many stark differences in the properties and behaviour of the studied cryoprotectants (the main focus of our work was on DMSO, trehalose and AFP). These differences are in accord with the distinct mechanisms of action of these materials. We focused on comparing their impact on ice crystal size, level of chromatin condensation, post-thaw cell viability, and occurence of serious DNA injury (DSBs) in thawed cells.

DMSO spreads homogeneously through the aqueous solution due to its strong hydrogen bonding with water molecules, but its molecules have a different symmetry. Therefore, it strongly distorts the overall hydrogen bond network in aqueous solution. The high dipole moment of DMSO and high permittivity of water also enable a long-range effect of DMSO on water dynamics. These properties of DMSO then influence the freezing process and ultimately result in the formation of small ice crystals. This is related to the small size of crystals that our X-ray experiments have confirmed in the 10% DMSO solution. The DMSO-cryopreserved

cells had the highest values of chromatin condensation and post-thaw viability from all tested materials. The high chromatin condensation of DMSO-treated thawed cells is likely caused by direct interaction between chromatin and DMSO molecules. The possible causal link between post-thaw cell viability and chromatin condensation is supported e.g. by the fact that sperms whose chromatin is naturally condensed are also relatively resistant to cryoinjury (Balhorn 1982; Ward 2010). Furthermore, cryopreservation in a hypertonic medium increases both chromatin condensation and post-thaw viability (compared to standard medium).

ApAFP752 radically slows down the dynamics of water molecules in its proximity. That is consistent with AFP having an ice-binding surface. Despite its inability to permeate the cell membrane, ApAFP752 increased the level of chromatin condensation and post-thaw cell viability, but only to an extent which was the lowest of all the cryoprotectants under study.

The impact of trehalose on the cell condition (viability and chromatin condensation) strongly increases after a long preincubation time. That is in agreement with our finding that it takes trehalose a correspondingly long time to permeate into the cytoplasm. Viability and chromatin condensation of cells preincubated with trehalose for 24 hours and then frozen/thawed in a trehalose-containing medium was significantly higher than viability and chromatin condensation of AFP-treated thawed cells. Trehalose acts as a natural osmolyte (osmoprotectant), and stabilizes phospholipid membranes and tertiary structure of proteins (Corradini et al. 2013; Kent et al. 2014).

Despite practically not penetrating into cell nuclei, both trehalose and AFP increase chromatin condensation in thawed cells. We hypothesize that chromatin condensation is provoked by changes in nucleus hydration and ionic balance. Extranuclear cryoprotectants may act by changing the intracellular osmotic pressure, followed by nucleus dehydration. Osmotic pressure (concentration of solutes) during freezing in turn also depends on the dynamics of ice formation. Thus, effects of extracellular cryoprotectants are not limited to favorably changing

the shape of ice crystals or to protecting cell membrane – they can also indirectly protect the cell on the nucleus level.

Based on our results, we can propose the following cryoprotective strategies:

1) using cryoprotectants that reduce ice crystal size and decrease possibility of cell membranes damage.
2) using cryoprotectants that cause chromatin condensation in frozen/thawed cells, which strongly correlates with cryopreserved cells' viability. In principle, even nonpermeating cryoprotectants can have a chromatin-condensing effect.
3) excluding the replicating (S-phase) cells from the cell population to be frozen/thawed. During freezing/thawing, S-phase cells are damaged by the collapse of replication forks (which later possibly leads to the formation of DSBs).

In all, our results help advance our understanding of freezing/thawing damage of cells, with some of them potentially serving as a basis for improvement of cryoprotective protocols. In future, we will work towards better elucidation of the role of chromatin condensation in cryopreservation. We will also pursue a more detailed understanding of the replication forks collapse in S-phase cells, and explore ways to prevent it.

Furthermore, we will use our insights into cryopreservation effects and mechanisms of action as clues in the quest for developing new, more effective and less harmful cryoprotective materials. Specifically, a development of novel PEG-based and trehalose-based cryoprotectants is already under way.

6 References

ABAZARI, A., L. G. MEIMETIS, G. BUDIN, S. S. BALE, et al. Engineered Trehalose Permeable to Mammalian Cells. Plos One, Jun 26 2015, 10(6).

AKHTAR, T., D. E. PEGG AND J. FOREMAN The effect of cooling and warming rates on the survival of cryopreserved L-cells. Cryobiology, Oct 1979, 16(5), 424-429.

ARMITAGE, W. J. AND S. J. RICH Vitrification of organized tissues. Cryobiology, Oct 1990, 27(5), 483-491.

AUER, G. K., T. K. LEE, M. RAJENDRAM, S. CESAR, et al. Mechanical Genomics Identifies Diverse Modulators of Bacterial Cell Stiffness. Cell Systems, Jun 22 2016, 2(6), 402-411.

BALHORN, R. A model for the structure of chromatin in mammalian sperm. Journal of Cell Biology, May 1982, 93(2), 298-305.

BALL, R. L., P. BAJAJ AND K. A. WHITEHEAD Achieving long-term stability of lipid nanoparticles: examining the effect of pH, temperature, and lyophilization. Int J Nanomedicine, 2017, 12, 305-315.

BATES, P. A. AND M. J. E. STERNBERG Model building by comparison at CASP3: Using expert knowledge and computer automation. Proteins-Structure Function and Genetics, 1999, 47-54.

BAUST, J. G. AND J. M. BAUST *Advances in biopreservation*. Edtion ed. Boca Raton, FL: CRC/Taylor & Francis, 2007. 426 p. p. ISBN 0849327725

9780849327728.

BENTRIVEDI, A., N. KITABATAKE AND E. DOI Toxicity of Dimethyl-Sulfoxide as a Solvent in Bioassay System with Hela-Cells Evaluated Colorimetrically with 3-(4,5-Dimethyl Thiazol-2-Yl)-2,5-Diphenyl-Tetrazolium Bromide. Agricultural and Biological Chemistry, Nov 1990, 54(11), 2961-2966.

BERENDSEN, H. J. C., D. VANDERSPOEL AND R. VANDRUNEN Gromacs - a Message-Passing Parallel Molecular-Dynamics Implementation. Computer Physics Communications, Sep 1995, 91(1-3), 43-56.

BERNIAK, K., P. RYBAK, T. BERNAS, M. ZAREBSKI, et al. Relationship Between DNA Damage Response, Initiated by Camptothecin or Oxidative Stress, and DNA Replication, Analyzed by Quantitative 3D Image Analysis. Cytometry Part A, Oct 2013, 83(10), 913-924.

BERTI, M. AND A. VINDIGNI Replication stress: getting back on track. Nature Structural & Molecular Biology, Feb 2016, 23(2), 103-109.

BILODEAU, G. G. Regular Pyramid Punch Problem. Journal of Applied Mechanics-Transactions of the Asme, Sep 1992, 59(3), 519-523.

BISCHOFS, I. B. AND U. S. SCHWARZ Cell organization in soft media due to active mechanosensing. Proceedings of the National Academy of Sciences of the United States of America, Aug 5 2003, 100(16), 9274-9279.

BOOTHBY, T. C., H. TAPIA, A. H. BROZENA, S. PISZKIEWICZ, et al. Tardigrades Use Intrinsically Disordered Proteins to Survive Desiccation. Molecular Cell, Mar 16 2017, 65(6), 975-984 e975.

BROERS, J. L. V., E. A. G. PEETERS, H. J. H. KUIJPERS, J. ENDERT, et al. Decreased mechanical stiffness in LMNA-/- cells is caused by defective nucleo-cytoskeletal integrity: implications for the development of laminopathies. Human Molecular Genetics, Nov 1 2004, 13(21), 2567-2580.

BUNGE, R. G. AND J. K. SHERMAN Fertilizing capacity of frozen human spermatozoa. Nature, Oct 24 1953, 172(4382), 767-768.

BURRELL, R. A., S. E. MCCLELLAND, D. ENDESFELDER, P. GROTH, et al. Replication stress links structural and numerical cancer chromosomal instability. Nature, Feb 2013, 494(7438), 492-496.

CELIK, Y., L. A. GRAHAM, Y. F. MOK, M. BAR, et al. Superheating of ice crystals in antifreeze protein solutions. Proc Natl Acad Sci U S A, Mar 23 2010, 107(12), 5423-5428.
CLARKE, C. J., S. L. BUCKLEY AND N. LINDNER Ice structuring proteins - a new name for antifreeze proteins. Cryo Letters, Mar-Apr 2002, 23(2), 89-92.
CORIELL, L. L., A. E. GREENE AND R. K. SILVER Histological Development of Cell and Tissue Culture Freezing. Cryobiology, Sep-Oct 1964, 51, 72-79.
CORRADINI, D., E. G. STREKALOVA, H. E. STANLEY AND P. GALLO Microscopic mechanism of protein cryopreservation in an aqueous solution with trehalose. Scientific Reports, Feb 6 2013, 3.
COTICCHIO, G., M. A. BONU, R. SCIAJNO, E. SERENI, et al. Truths and myths of oocyte sensitivity to controlled rate freezing. Reprod Biomed Online, Jul 2007, 15(1), 24-30.
CROWE, L. M., R. MOURADIAN, J. H. CROWE, S. A. JACKSON, et al. Effects of carbohydrates on membrane stability at low water activities. Biochim Biophys Acta, Jan 11 1984, 769(1), 141-150.
DALEY, M. E. AND B. D. SYKES Characterization of threonine side chain dynamics in an antifreeze protein using natural abundance 13C NMR spectroscopy. J Biomol NMR, Jun 2004, 29(2), 139-150.
DAMJANOVIC, V. AND D. THOMAS The use of polyvinylpyrrolidone as a cryoprotectant in the freezing of human lymphocytes. Cryobiology, 1974/08/01/ 1974, 11(4), 312-316.
DARDEN, T., D. YORK AND L. PEDERSEN Particle Mesh Ewald - an N.Log(N) Method for Ewald Sums in Large Systems. Journal of Chemical Physics, Jun 15 1993, 98(12), 10089-10092.
DE MENORVAL, M. A., L. M. MIR, M. L. FERNANDEZ AND R. REIGADA Effects of Dimethyl Sulfoxide in Cholesterol-Containing Lipid Membranes: A Comparative Study of Experiments In Silico and with Cells. Plos One, Jul 25 2012, 7(7).
DE PAULA, T. S., R. P. BERTOLLA, D. M. SPAINE, M. A. CUNHA, et al. Effect of cryopreservation on sperm apoptotic deoxyribonucleic acid fragmentation in patients with oligozoospermia. Fertility and Sterility, Sep 2006, 86(3), 597-600.
DEPINA, A. S. AND G. M. LANGFORD Vesicle transport: the role of actin filaments and myosin motors. Microsc Res Tech, Oct 15 1999, 47(2), 93-106.
DEVRIES, A. L. AND D. E. WOHLSCHLAG Freezing Resistance in Some Antarctic Fishes. Science, 1969, 163(3871), 1073-+.
DIMITRIADIS, E. K., F. HORKAY, J. MARESCA, B. KACHAR, et al. Determination of elastic moduli of thin layers of soft material using the atomic force microscope. Biophys J, May 2002, 82(5), 2798-2810.
DOEBBLER, G. F., R. R. SAKAIDA, C. W. COWLEY AND A. P. RINFRET Cryogenic preservation of whole blood for transfusion in vitro study of a process using rapid freezing, thawing and protection by polyvinylpyrrolidone. Transfusion, Mar-Apr 1966, 6(2), 104-111.
DONG, J., J. MALSAM, J. C. BISCHOF, A. HUBEL, et al. Spatial distribution of the state of water in frozen mammalian cells. Biophys J, Oct 20 2010, 99(8), 2453-2459.
DURU, N. K., M. S. MORSHEDI, A. SCHUFFNER AND S. OEHNINGER Cryopreservation-thawing of fractionated human spermatozoa is associated with membrane phosphatidylserine externalization and not DNA fragmentation. Journal of Andrology, Jul-Aug 2001, 22(4), 646-651.
EASLEY, G. T., MAYER, D.T., AND BOGART, R. Influence of diluters, rate of cooling, and storage temperatures on survival of bull sperm. Am. J. Vet. Res., 1942, 3, 358–363.
ELLIOTT, G. D., S. P. WANG AND B. J. FULLER Cryoprotectants: A review of the actions and applications of cryoprotective solutes that modulate cell recovery from ultra-low temperatures. Cryobiology, Jun 2017, 76, 74-91.
ELSAESSER, M. S., K. WINKEL, E. MAYER AND T. LOERTING Reversibility and isotope effect of the calorimetric glass -> liquid transition of low-density amorphous ice. Physical Chemistry Chemical Physics, 2010, 12(3), 708-712.

EROGLU, A., M. J. RUSSO, R. BIEGANSKI, A. FOWLER, et al. Intracellular trehalose improves the survival of cryopreserved mammalian cells. Nat Biotechnol, Feb 2000, 18(2), 163-167.
FAHY, G. M. Simplified calculation of cell water content during freezing and thawing in nonideal solutions of cryoprotective agents and its possible application to the study of "solution effects" injury. Cryobiology, Oct 1981, 18(5), 473-482.
FAHY, G. M., B. WOWK, R. PAGOTAN, A. CHANG, et al. Physical and biological aspects of renal vitrification. Organogenesis, Jul 2009, 5(3), 167-175.
FALK, M., I. FALKOVÁ, E. PAGÁČOVÁ, O. KOPEČNÁ, et al. Critical defects in cryopreserved cell nuclei: DNA structure changes. Scientific Reports (submitted), 2018.
FALK, M., E. LUKASOVA AND S. KOZUBEK Chromatin structure influences the sensitivity of DNA to gamma-radiation. Biochimica Et Biophysica Acta-Molecular Cell Research, Dec 2008, 1783(12), 2398-2414.
FRANKS, F. *Water and aqueous solutions at subzero temperatures*. Edtion ed. New York: Plenum Press, 1982. xiii, 484 p. p. ISBN 0306407108.
FRASER, L., J. STRZEZEK AND W. KORDAN Effect of Freezing on Sperm Nuclear DNA. Reproduction in Domestic Animals, Sep 2011, 46, 14-17.
FUGGER, K., M. MISTRIK, K. J. NEELSEN, Q. YAO, et al. FBH1 Catalyzes Regression of Stalled Replication Forks. Cell Reports, Mar 17 2015, 10(10), 1749-1757.
FULLER, B. J., J. D. GOWER AND C. J. GREEN Free radical damage and organ preservation: fact or fiction? A review of the interrelationship between oxidative stress and physiological ion disbalance. Cryobiology, Oct 1988, 25(5), 377-393.
FULLER, B. J., N. LANE AND E. E. BENSON *Life in the frozen state*. Edtion ed. Boca Raton, Fla.: CRC Press, 2004. 672 p. p. ISBN 0415247004 (alk. paper).
FUNG, Y. C. B. ELASTICITY OF SOFT TISSUES IN SIMPLE ELONGATION. American Journal of Physiology, 1967, 213(6), 1532-&.
GALVAO, J., B. DAVIS, M. TILLEY, E. NORMANDO, et al. Unexpected low-dose toxicity of the universal solvent DMSO. Faseb Journal, Mar 2014, 28(3), 1317-1330.
GAO, D. AND J. K. CRITSER Mechanisms of cryoinjury in living cells. ILAR J, 2000, 41(4), 187-196.
GAVARA, N. A beginner's guide to atomic force microscopy probing for cell mechanics. Microsc Res Tech, Jan 2017, 80(1), 75-84.
GAVARA, N. AND R. S. CHADWICK Determination of the elastic moduli of thin samples and adherent cells using conical atomic force microscope tips. Nature Nanotechnology, Nov 2012, 7(11), 733-736.
GOLAN, M., Š. JELÍNKOVÁ, I. KRATOCHVÍLOVÁ, P. SKLÁDAL, et al. AFM monitoring the influence of selected cryoprotectants on regeneration of cryopreserved cells mechanical properties. Frontiers in Physiology (submitted), 2018a.
GOLAN, M., J. PŘIBYL, M. PEŠL, Š. JELÍNKOVÁ, et al. Cryopreserved cells regeneration monitored by atomic force microscopy and correlated with state of cytoskeleton and nuclear membrane. IEEE Transactions on Nanobioscience (accepted), 2018b, 1-8.
GONZALEZ-SANDOVAL, A. AND S. M. GASSER On TADs and LADs: Spatial Control Over Gene Expression. Trends Genet, Aug 2016, 32(8), 485-495.
GREEN, J. L. AND C. A. ANGELL Phase relations and vitrification in saccharide-water solutions and the trehalose anomaly. The Journal of Physical Chemistry, 1989/04/01 1989, 93(8), 2880-2882.
GRUENBAUM, Y., R. D. GOLDMAN, R. MEYUHAS, E. MILLS, et al. The nuclear lamina and its functions in the nucleus. Int Rev Cytol, 2003, 226, 1-62.
GUO, N., I. PUHLEV, D. R. BROWN, J. MANSBRIDGE, et al. Trehalose expression confers desiccation tolerance on human cells. Nat Biotechnol, Feb 2000, 18(2), 168-171.
GURTOVENKO, A. A. AND J. ANWAR Modulating the structure and properties of cell membranes: The molecular mechanism of action of dimethyl sulfoxide. Journal of Physical Chemistry B, Sep 6 2007, 111(35), 10453-10460.

HARLAND, C. W., Z. BOTYANSZKI, D. RABUKA, C. R. BERTOZZI, et al. Synthetic trehalose glycolipids confer desiccation resistance to supported lipid monolayers. Langmuir, May 5 2009, 25(9), 5193-5198.
HEDOUX, A., F. AFFOUARD, M. DESCAMPS, Y. GUINET, et al. Microscopic description of protein thermostabilization mechanisms with disaccharides from Raman spectroscopy investigations. Journal of Physics-Condensed Matter, May 23 2007, 19(20).
HEDOUX, A., L. PACCOU, S. ACHIR AND Y. GUINET Mechanism of protein stabilization by trehalose during freeze-drying analyzed by in situ micro-raman spectroscopy. Journal of Pharmaceutical Sciences, Aug 2013, 102(8), 2484-2494.
HEDOUX, A., J. F. WILLART, R. IONOV, F. AFFOUARD, et al. Analysis of sugar bioprotective mechanisms on the thermal denaturation of lysozyme from Raman scattering and differential scanning calorimetry investigations. Journal of Physical Chemistry B, Nov 16 2006, 110(45), 22886-22893.
HERMANOWICZ, P., M. SARNA, K. BURDA AND H. GABRYS AtomicJ: An open source software for analysis of force curves. Review of Scientific Instruments, Jun 2014, 85(6).
HOFER, M., M. FALK, D. KOMURKOVA, I. FALKOVA, et al. Two New Faces of Amifostine: Protector from DNA Damage in Normal Cells and Inhibitor of DNA Repair in Cancer Cells. J Med Chem, Apr 14 2016a, 59(7), 3003-3017.
HOFER, M., M. FALK, D. KOMURKOVA, I. FALKOVA, et al. Two New Faces of Amifostine: Protector from DNA Damage in Normal Cells and Inhibitor of DNA Repair in Cancer Cells. Journal of Medicinal Chemistry, Apr 2016b, 59(7), 3003-3017.
CHEN, C. Pregnancy after human oocyte cryopreservation. Lancet, Apr 19 1986, 1(8486), 884-886.
CHEN, T., J. P. ACKER, A. EROGLU, S. CHELEY, et al. Beneficial effect of intracellular trehalose on the membrane integrity of dried mammalian cells. Cryobiology, Sep 2001, 43(2), 168-181.
CHEN, T. N., A. FOWLER AND M. TONER Literature review: Supplemented phase diagram of the trehalose-water binary mixture. Cryobiology, May 2000, 40(3), 277-282.
CHENG, C. Y., J. S. SONG, J. PAS, L. H. H. MEIJER, et al. DMSO Induces Dehydration near Lipid Membrane Surfaces. Biophys J, Jul 21 2015, 109(2), 330-339.
CHIOU, Y. W., H. K. LIN, M. J. TANG, H. H. LIN, et al. The Influence of Physical and Physiological Cues on Atomic Force Microscopy-Based Cell Stiffness Assessment. Plos One, Oct 23 2013, 8(10).
JAIN, N. K. AND I. ROY Effect of trehalose on protein structure. Protein Science, Jan 2009, 18(1), 24-36.
JAIN, N. K. AND I. ROY Trehalose and protein stability. Curr Protoc Protein Sci, Feb 2010, Chapter 4, Unit 4 9.
JANMEY, P. A. AND R. T. MILLER Mechanisms of mechanical signaling in development and disease. Journal of Cell Science, Jan 2011, 124(1), 9-18.
JENA, S. AND A. AKSAN Effect of high DMSO concentration on albumin during freezing and vitrification. Rsc Advances, 2017, 7(69), 43611-43620.
JOHARI, G. P., A. HALLBRUCKER AND E. MAYER The Glass Liquid Transition of Hyperquenched Water. Nature, Dec 10 1987, 330(6148), 552-553.
JONES, R. M. AND E. PETERMANN Replication fork dynamics and the DNA damage response. Biochemical Journal, Apr 1 2012, 443, 13-26.
KARLSSON, J. O., E. G. CRAVALHO, I. H. BOREL RINKES, R. G. TOMPKINS, et al. Nucleation and growth of ice crystals inside cultured hepatocytes during freezing in the presence of dimethyl sulfoxide. Biophys J, Dec 1993a, 65(6), 2524-2536.
KARLSSON, J. O. M., E. G. CRAVALHO AND M. TONER Intracellular Ice Formation - Causes and Consequences. Cryo-Letters, Nov-Dec 1993b, 14(6), 323-336.
KASAI, M., K. NIWA AND A. IRITANI Survival of rat embryos after freezing. J Reprod Fertil, Sep 1982, 66(1), 367-370.

KELLEY-QUON, L. I., C. H. TSENG, C. JANZEN AND S. B. SHEW Congenital malformations associated with assisted reproductive technology: A California statewide analysis. Journal of Pediatric Surgery, Jun 2013, 48(6), 1218-1224.
KENT, B., T. HUNT, T. A. DARWISH, T. HAUSS, et al. Localization of trehalose in partially hydrated DOPC bilayers: insights into cryoprotective mechanisms. J R Soc Interface, Jun 6 2014, 11(95), 20140069.
KHURANA, S. AND P. OBERDOERFFER Replication Stress: A Lifetime of Epigenetic Change. Genes, Sep 2015, 6(3), 858-877.
KNIGHT, C. A. AND J. G. DUMAN Inhibition of recrystallization of ice by insect thermal hysteresis proteins: A possible cryoprotective role. Cryobiology, 1986/06/01/ 1986, 23(3), 256-262.
KOPEIKA, J., A. THORNHILL AND Y. KHALAF The effect of cryopreservation on the genome of gametes and embryos: principles of cryobiology and critical appraisal of the evidence. Human Reproduction Update, Mar-Apr 2015, 21(2), 209-227.
KORBER, C., S. ENGLICH AND G. RAU Intracellular ice formation: cryomicroscopical observation and calorimetric measurement. J Microsc, Feb 1991, 161(Pt 2), 313-325.
KOZUBEK, M., S. KOZUBEK, E. LUKASOVA, E. BARTOVA, et al. Combined confocal and wide-field high-resolution cytometry of fluorescent in situ hybridization-stained cells. Cytometry, Sep 1 2001, 45(1), 1-12.
KOZUBEK, M., P. MATULA, P. MATULA AND S. KOZUBEK Automated acquisition and processing of multidimensional image data in confocal in vivo microscopy. Microsc Res Tech, Jun 1 2004, 64(2), 164-175.
KRASTEVA, N., D. VOLLHARDT, G. BREZESINSKI AND H. MOHWALD Effect of sugars and dimethyl sulfoxide on the structure and phase behavior of DPPC monolayers. Langmuir, Feb 2001, 17(4), 1209-1214.
KRATOCHVILOVA, I., M. GOLAN, K. POMEISL, J. RICHTER, et al. Theoretical and experimental study of the antifreeze protein AFP752, trehalose and dimethyl sulfoxide cryoprotection mechanism: correlation with cryopreserved cell viability. Rsc Advances, 2017, 7(1), 352-360.
KRATOCHVÍLOVÁ, I., M. GOLAN, M. VALA, M. ŠPÉROVÁ, et al. Theoretical and Experimental Study of Charge Transfer through DNA: Impact of Mercury Mediated T-Hg-T Base Pair. The Journal of Physical Chemistry B, 2014/05/22 2014a, 118(20), 5374-5381.
KRATOCHVÍLOVÁ, I., J. ŠEBERA, P. ASHCHEULOV, M. GOLAN, et al. Magnetical and Optical Properties of Nanodiamonds Can Be Tuned by Particles Surface Chemistry: Theoretical and Experimental Study. The Journal of Physical Chemistry C, 2014/10/30 2014b, 118(43), 25245-25252.
KRIEGER, E. AND G. VRIEND YASARA View-molecular graphics for all devices-from smartphones to workstations. Bioinformatics, Oct 15 2014, 30(20), 2981-2982.
KRISHNAMOORTHY, A. N., C. HOLM AND J. SMIATEK Local Water Dynamics around Antifreeze Protein Residues in the Presence of Osmolytes: The Importance of Hydroxyl and Disaccharide Groups. Journal of Physical Chemistry B, Oct 9 2014, 118(40), 11613-11621.
LAMPUGNANI, M. G., M. PEDENOVI, A. NIEWIAROWSKI, B. CASALI, et al. Effects of dimethyl sulfoxide (DMSO) on microfilament organization, cellular adhesion, and growth of cultured mouse B16 melanoma cells. Exp Cell Res, Oct 1987, 172(2), 385-396.
LANGELIER, E., R. SUETTERLIN, C. D. HOEMANN, U. AEBI, et al. The chondrocyte cytoskeleton in mature articular cartilage: Structure and distribution of actin, tubulin, and vimentin filaments. Journal of Histochemistry & Cytochemistry, Oct 2000, 48(10), 1307-1320.
LIN, C. AND S. TSAI The effect of cryopreservation on DNA damage, gene expression and protein abundance in vertebrate. Italian Journal of Animal Science, 2012/01/01 2012, 11(1), e21.

LIN, L., P. M. KRAGH, S. PURUP, M. KUWAYAMA, et al. Osmotic stress induced by sodium chloride, sucrose or trehalose improves cryotolerance and developmental competence of porcine oocytes. Reprod Fertil Dev, 2009, 21(2), 338-344.
LINDORFF-LARSEN, K., S. PIANA, K. PALMO, P. MARAGAKIS, et al. Improved side-chain torsion potentials for the Amber ff99SB protein force field. Proteins-Structure Function and Bioinformatics, Jun 2010, 78(8), 1950-1958.
LIOU, Y. C., A. TOCILJ, P. L. DAVIES AND Z. C. JIA Mimicry of ice structure by surface hydroxyls and water of a beta-helix antifreeze protein. Nature, Jul 20 2000, 406(6793), 322-324.
LIU, J., E. J. WOODS, Y. AGCA, E. S. CRITSER, et al. Cryobiology of rat embryos II: A theoretical model for the development of interrupted slow freezing procedures. Biol Reprod, Nov 2000, 63(5), 1303-1312.
LIU, Q., R. K. SCHMIDT, B. TEO, P. A. KARPLUS, et al. Molecular dynamics studies of the hydration of alpha,alpha-trehalose. Journal of the American Chemical Society, Aug 20 1997, 119(33), 7851-7862.
LIU, X. S., J. B. LITTLE AND Z. M. YUAN Glycolytic metabolism influences global chromatin structure. Oncotarget, Feb 2015a, 6(6), 4214-4225.
LIU, Z. Y., H. L. LI, H. PANG, J. MA, et al. Enhancement effect of solutes of low molecular mass on the insect antifreeze protein ApAFP752 from Anatolica polita. Journal of Thermal Analysis and Calorimetry, Apr 2015b, 120(1), 307-315.
LOEBRICH, M., A. SHIBATA, A. BEUCHER, A. FISHER, et al. gamma H2AX foci analysis for monitoring DNA double-strand break repair Strengths, limitations and optimization. Cell Cycle, Feb 15 2010, 9(4), 662-669.
LOVELOCK, J. E. AND M. W. BISHOP Prevention of freezing damage to living cells by dimethyl sulphoxide. Nature, May 16 1959, 183(4672), 1394-1395.
LUO, Q., D. KUANG, B. ZHANG AND G. SONG Cell stiffness determined by atomic force microscopy and its correlation with cell motility. Biochim Biophys Acta, Sep 2016, 1860(9), 1953-1960.
LUYET, B. J. The vitrification of organic colloids and of protoplasm. Biodynamica, 1937, 1(29), 1-14.
LUYET, B. J. AND M. P. GEHENIO *Life and death at low temperatures*. Edtion ed. Normandy, Mo., : Biodynamica, 1940. 341 p. p.
LUZAR, A. AND D. CHANDLER Structure and Hydrogen-Bond Dynamics of Water-Dimethyl Sulfoxide Mixtures by Computer-Simulations. Journal of Chemical Physics, May 15 1993, 98(10), 8160-8173.
M. J. FRISCH, G. W. T., H. B. SCHLEGEL, G. E. SCUSERIA, M. A. ROBB, J. R. CHEESEMAN AND J. A. POPLE. GAUSSIAN 09 (Revision B.01). [2010.
MA, J., J. WANG, X. F. MAO AND Y. WANG DIFFERENTIAL EXPRESSION OF TWO ANTIFREEZE PROTEINS IN THE DESERT BEETLE Anatolica polita (COLEOPTERA: TENEBRIONDAE): SEASONAL VARIATION AND ENVIRONMENTAL EFFECTS. Cryoletters, Sep-Oct 2012, 33(5), 337-348.
MAO, X. F., Z. Y. LIU, H. L. LI, J. MA, et al. Calorimetric studies on an insect antifreeze protein ApAFP752 from Anatolica polita. Journal of Thermal Analysis and Calorimetry, Apr 2011a, 104(1), 343-349.
MAO, X. F., Z. Y. LIU, J. MA, H. PANG, et al. Characterization of a novel beta-helix antifreeze protein from the desert beetle Anatolica polita. Cryobiology, Apr 2011b, 62(2), 91-99.
MATSUMURA, K., J. Y. BAE AND S. H. HYON Polyampholytes as cryoprotective agents for mammalian cell cryopreservation. Cell Transplant, 2010, 19(6), 691-699.
MAUGIS, D. ADHESION OF SPHERES - THE JKR-DMT TRANSITION USING A DUGDALE MODEL. Journal of Colloid and Interface Science, Apr 1992, 150(1), 243-269.

MAYA-MENDOZA, A., J. M. MERCHUT-MAYA, J. BARTKOVA, J. BARTEK, et al. Immortalised breast epithelia survive prolonged DNA replication stress and return to cycle from a senescent-like state. Cell Death & Disease, Jul 2014, 5, 13.
MAZUR, P. Manifestations of injury in yeast cells exposed to subzero temperatures. I. Morphological changes in freeze-substituted and in "frozen-thawed" cells. J Bacteriol, Nov 1961a, 82, 662-672.
MAZUR, P. Manifestations of injury in yeast cells exposed to subzero temperatures. II. Changes in specific gravity and in the concentration and quantity of cell solids. J Bacteriol, Nov 1961b, 82, 673-684.
MAZUR, P. Kinetics of water loss from cells at subzero temperatures and the likelihood of intracellular freezing. J. Gen. Physiol., 1963, 47, 347–369.
MERCK. Manual to the Muse® Cell Analyser (Merck Millipore) and Muse® Cell Cycle Assay Kit (MCH100106). In.
MITROSSILIS, D., J. FOUCHARD, A. GUIROY, N. DESPRAT, et al. Single-cell response to stiffness exhibits muscle-like behavior. Proceedings of the National Academy of Sciences of the United States of America, Oct 27 2009, 106(43), 18243-18248.
MIYAMOTO, H. AND T. ISHIBASHI Survival of mouse embryos frozen-thawed slowly or rapidly in the presence of various cryoprotectants. J Exp Zool, Apr 1983, 226(1), 123-127.
MONZO, C., D. HAOUZI, K. ROMAN, S. ASSOU, et al. Slow freezing and vitrification differentially modify the gene expression profile of human metaphase II oocytes. Hum Reprod, Jul 2012, 27(7), 2160-2168.
MORGAN, J. T., V. K. RAGHUNATHAN, Y. R. CHANG, C. J. MURPHY, et al. The intrinsic stiffness of human trabecular meshwork cells increases with senescence. Oncotarget, Jun 20 2015, 6(17), 15362-15374.
MORRIS, G. J. AND E. ACTON Controlled ice nucleation in cryopreservation--a review. Cryobiology, Apr 2013, 66(2), 85-92.
NAGASE, H., N. OGAWA, T. ENDO, M. SHIRO, et al. Crystal structure of an anhydrous form of trehalose: Structure of water channels of trehalose polymorphism. Journal of Physical Chemistry B, Jul 31 2008, 112(30), 9105-9111.
NECAS, D. AND P. KLAPETEK Gwyddion: an open-source software for SPM data analysis. Central European Journal of Physics, Feb 2012, 10(1), 181-188.
NIKOLAEV, N. I., T. MULLER, D. J. WILLIAMS AND Y. LIU Changes in the stiffness of human mesenchymal stem cells with the progress of cell death as measured by atomic force microscopy. Journal of Biomechanics, Feb 7 2014, 47(3), 625-630.
OBRIEN, J. Stability of trehalose, sucrose and glucose to nonenzymatic browning in model systems. Journal of Food Science, Jul-Aug 1996, 61(4), 679-682.
OFEK, G., D. C. WILTZ AND K. A. ATHANASIOU Contribution of the cytoskeleton to the compressive properties and recovery behavior of single cells. Biophys J, Oct 07 2009, 97(7), 1873-1882.
OGDEN, R. W. LARGE DEFORMATION ISOTROPIC ELASTICITY - CORRELATION OF THEORY AND EXPERIMENT FOR COMPRESSIBLE RUBBERLIKE SOLIDS. Proceedings of the Royal Society of London Series a-Mathematical and Physical Sciences, 1972, 328(1575), 567-&.
OH, K. I., K. RAJESH, J. F. STANTON AND C. R. BAIZ Quantifying Hydrogen-Bond Populations in Dimethyl Sulfoxide/Water Mixtures. Angew Chem Int Ed Engl, Sep 11 2017, 56(38), 11375-11379.
OHTAKE, S., C. SCHEBOR AND J. J. DE PABLO Effects of trehalose on the phase behavior of DPPC-cholesterol unilamellar vesicles. Biochim Biophys Acta, Jan 2006, 1758(1), 65-73.
OLSON, C. K., K. M. KEPPLER-NOREUIL, P. A. ROMITTI, W. T. BUDELIER, et al. In vitro fertilization is associated with an increase in major birth defects. Fertil Steril, Nov 2005, 84(5), 1308-1315.
OLSSON, C., H. JANSSON AND J. SWENSON The Role of Trehalose for the Stabilization of Proteins. Journal of Physical Chemistry B, May 26 2016, 120(20), 4723-4731.

PAASCH, U., R. K. SHARMA, A. K. GUPTA, S. GRUNEWALD, et al. Cryopreservation and thawing is associated with varying extent of activation of apoptotic machinery in subsets of ejaculated human spermatozoal. Biology of Reproduction, Dec 2004, 71(6), 1828-1837.
PARKENING, T. A., Y. TSUNODA AND M. C. CHANG Effects of various low temperatures, cryoprotective agents and cooling rates on the survival, fertilizability and development of frozen-thawed mouse eggs. J Exp Zool, Sep 1976, 197(3), 369-374.
PAUL H. PHILLIPS, H. A. L. A Yolk-Buffer Pabulum for the Preservation of Bull Semen 1940, 23(5), 399–404.
PESEN, D. AND J. H. HOH Micromechanical architecture of the endothelial cell cortex. Biophys J, Jan 2005, 88(1), 670-679.
PRAVDYUK, A. I., Y. A. PETRENKO, B. J. FULLER AND A. Y. PETRENKO Cryopreservation of alginate encapsulated mesenchymal stromal cells. Cryobiology, Jun 2013, 66(3), 215-222.
PRIVALOV, P. L. Cold denaturation of proteins. Crit Rev Biochem Mol Biol, 1990, 25(4), 281-305.
RADOTIC, K., C. RODUIT, J. SIMONOVIC, P. HORNITSCHEK, et al. Atomic force microscopy stiffness tomography on living Arabidopsis thaliana cells reveals the mechanical properties of surface and deep cell-wall layers during growth. Biophys J, Aug 8 2012, 103(3), 386-394.
RAJAN, R. AND K. MATSUMURA Synthetic polymers for cellular cryopreservation: A new and versatile class of cryoprotectants. Frontiers in Bioengineering and Biotechnology.
RALL, W. F. AND C. POLGE Effect of warming rate on mouse embryos frozen and thawed in glycerol. J Reprod Fertil, Jan 1984, 70(1), 285-292.
RASMUSSEN, D. H., M. N. MACAULAY AND A. P. MACKENZIE Supercooling and nucleation of ice in single cells. Cryobiology, Aug 1975, 12(4), 328-339.
RASMUSSEN, R. D., M. K. GAJJAR, L. TUCKOVA, K. E. JENSEN, et al. BRCA1-regulated RRM2 expression protects glioblastoma cells from endogenous replication stress and promotes tumorigenicity. Nature Communications, Nov 2016, 7, 14.
RICO, F., P. ROCA-CUSACHS, N. GAVARA, R. FARRE, et al. Probing mechanical properties of living cells by atomic force microscopy with blunted pyramidal cantilever tips. Physical Review E, Aug 2005, 72(2).
SALBREUX, G., G. CHARRAS AND E. PALUCH Actin cortex mechanics and cellular morphogenesis. Trends Cell Biol, Oct 2012, 22(10), 536-545.
SAPIR, L. AND D. HARRIES Linking Trehalose Self-Association with Binary Aqueous Solution Equation of State. Journal of Physical Chemistry B, Feb 3 2011, 115(4), 624-634.
SARNI, D. AND B. KEREM Oncogene-Induced Replication Stress Drives Genome Instability and Tumorigenesis. International Journal of Molecular Sciences, Jul 2017, 18(7).
SEVCIK, J., M. FALK, P. KLEIBLOVA, F. LHOTA, et al. The BRCA1 alternative splicing variant Delta 14-15 with an in-frame deletion of part of the regulatory serine-containing domain (SCD) impairs the DNA repair capacity in MCF-7 cells. Cellular Signalling, May 2012, 24(5), 1023-1030.
SHARP, D. M., A. PICKEN, T. J. MORRIS, C. J. HEWITT, et al. Amphipathic polymer-mediated uptake of trehalose for dimethyl sulfoxide-free human cell cryopreservation. Cryobiology, Dec 2013, 67(3), 305-311.
SCHEBOR, C., L. BURIN, M. D. BUERA AND J. CHIRIFE Stability to hydrolysis and browning of trehalose, sucrose and raffinose in low-moisture systems in relation to their use as protectants of dry biomaterials. Food Science and Technology-Lebensmittel-Wissenschaft & Technologie, 1999, 32(8), 481-485.
SCHNEIDER, C. A., W. S. RASBAND AND K. W. ELICEIRI NIH Image to ImageJ: 25 years of image analysis. Nat Methods, Jul 2012, 9(7), 671-675.
SCHULTZ, L. B., N. H. CHEHAB, A. MALIKZAY AND T. D. HALAZONETIS p53 Binding protein 1 (53BP1) is an early participant in the cellular response to DNA double-strand breaks. Journal of Cell Biology, Dec 25 2000, 151(7), 1381-1390.

SIEME, H., H. OLDENHOF AND W. F. WOLKERS Sperm Membrane Behaviour during Cooling and Cryopreservation. Reprod Domest Anim, Sep 2015, 50 Suppl 3, 20-26.
SMIATEK, J., R. K. HARISHCHANDRA, H. J. GALLA AND A. HEUER Low concentrated hydroxyectoine solutions in presence of DPPC lipid bilayers: A computer simulation study. Biophysical Chemistry, Oct-Nov 2013, 180, 102-109.
SMITH, A. U. Prevention of haemolysis during freezing and thawing of red blood-cells. Lancet, Dec 30 1950, 2(6644), 910-911.
SNEDDON, I. N. The relation between load and penetration in the axisymmetric boussinesq problem for a punch of arbitrary profile. International Journal of Engineering Science, 1965/05/01/ 1965, 3(1), 47-57.
STOKICH, B., Q. OSGOOD, D. GRIMM, S. MOORTHY, et al. Cryopreservation of hepatocyte (HepG2) cell monolayers: Impact of trehalose. Cryobiology, Oct 2014, 69(2), 281-290.
TAKAHASHI, T., A. HIRSH, E. ERBE AND R. J. WILLIAMS Mechanism of cryoprotection by extracellular polymeric solutes. Biophys J, Sep 1988, 54(3), 509-518.
TAYLOR, M. J., H. L. BANK AND M. J. BENTON Selective destruction of leucocytes by freezing as a potential means of modulating tissue immunogenicity: membrane integrity of lymphocytes and macrophages. Cryobiology, Apr 1987, 24(2), 91-102.
TECHER, H., S. KOUNDRIOUKOFF, A. NICOLAS AND M. DEBATISSE The impact of replication stress on replication dynamics and DNA damage in vertebrate cells. Nature Reviews Genetics, Sep 2017, 18(9), 535-550.
TOJKANDER, S., G. GATEVA AND P. LAPPALAINEN Actin stress fibers--assembly, dynamics and biological roles. Journal of Cell Science, Apr 15 2012, 125(Pt 8), 1855-1864.
TONER, M., E. G. CRAVALHO AND M. KAREL Thermodynamics and Kinetics of Intracellular Ice Formation during Freezing of Biological Cells. Journal of Applied Physics, Feb 1 1990, 67(3), 1582-1593.
TOUHAMI, A., B. NYSTEN AND Y. F. DUFRENE Nanoscale mapping of the elasticity of microbial cells by atomic force microscopy. Langmuir, May 2003, 19(11), 4539-4543.
TROUNSON, A., A. PEURA AND C. KIRBY Ultrarapid freezing: a new low-cost and effective method of embryo cryopreservation. Fertil Steril, Nov 1987, 48(5), 843-850.
VAN DEN ABBEEL, E., J. VAN DER ELST AND A. C. VAN STEIRTEGHEM The effect of temperature at which slow cooling is terminated and of thawing rate on the survival of one-cell mouse embryos frozen in dimethyl sulfoxide or 1,2-propanediol solutions. Cryobiology, Oct 1994, 31(5), 423-433.
VARGAS-PINTO, R., H. GONG, A. VAHABIKASHI AND M. JOHNSON The Effect of the Endothelial Cell Cortex on Atomic Force Microscopy Measurements. Biophys J, Jul 16 2013, 105(2), 300-309.
VERDE, A. V. AND R. K. CAMPEN Disaccharide Topology Induces Slowdown in Local Water Dynamics. Journal of Physical Chemistry B, Jun 2011, 115(21), 7069-7084.
VILLARREAL, M. A., S. B. DIAZ, E. A. DISALVO AND G. G. MONTICH Molecular dynamics simulation study of the interaction of trehalose with lipid membranes. Langmuir, Aug 31 2004, 20(18), 7844-7851.
WALLACE, V. M., N. R. DHUMAL, F. M. ZEHENTBAUER, H. J. KIM, et al. Revisiting the Aqueous Solutions of Dimethyl Sulfoxide by Spectroscopy in the Mid- and Near-Infrared: Experiments and Car-Parrinello Simulations. Journal of Physical Chemistry B, Nov 19 2015, 119(46), 14780-14789.
WARD, W. S. Function of sperm chromatin structural elements in fertilization and development. Mol Hum Reprod, Jan 2010, 16(1), 30-36.
WELLS, J. R., A. SULLIVAN AND M. J. CLINE A technique for the separation and cryopreservation of myeloid stem cells from human bone marrow. Cryobiology, Jun 1979, 16(3), 201-210.
WESLEY-SMITH, J., C. WALTERS, N. W. PAMMENTER AND P. BERJAK Why is intracellular ice lethal? A microscopical study showing evidence of programmed cell death in cryo-exposed

embryonic axes of recalcitrant seeds of Acer saccharinum. Ann Bot, May 2015, 115(6), 991-1000.
WHITTINGHAM, D. G., P. MAZUR AND S. P. LEIBO Survival of Mouse Embryos Frozen to -196 Degrees and -269 Degrees C. Science, 1972, 178(4059), 411-+.
WIERZBICKI, A., P. DALAL, T. E. CHEATHAM, 3RD, J. E. KNICKELBEIN, et al. Antifreeze proteins at the ice/water interface: three calculated discriminating properties for orientation of type I proteins. Biophys J, Sep 1 2007, 93(5), 1442-1451.
WOLFRAM, I. "Mathematica," Wolfram Research, 2017.
WOLFRAM RESEARCH, I. Mathematica. [Champaign, Illinois: Wolfram Research, Inc., 2017.
WOLKERS, W. F., S. K. BALASUBRAMANIAN, E. L. ONGSTAD, H. C. ZEC, et al. Effects of freezing on membranes and proteins in LNCaP prostate tumor cells. Biochim Biophys Acta, Mar 2007, 1768(3), 728-736.
WOODS, E., S. THIRUMALA, S. BADHE-BUCHANAN, D. CLARKE, et al. Off the Shelf Cellular Therapeutics: Factors to Consider during Cryopreservation and Storage of Human Cells for Clinical Use. Cytotherapy, Jun 2016, 18(6), S46-S46.
WOWK, B. Thermodynamic aspects of vitrification. Cryobiology, Feb 2010, 60(1), 11-22.
XU, W. W., R. MEZENCEV, B. KIM, L. J. WANG, et al. Cell Stiffness Is a Biomarker of the Metastatic Potential of Ovarian Cancer Cells. Plos One, Oct 4 2012, 7(10).
YEH, Y. AND R. E. FEENEY Antifreeze Proteins: Structures and Mechanisms of Function. Chem Rev, Mar 28 1996, 96(2), 601-618.
YI, X. Y., M. X. LIU, Q. LUO, H. L. ZHUO, et al. Toxic effects of dimethyl sulfoxide on red blood cells, platelets, and vascular endothelial cells in vitro. Febs Open Bio, Apr 2017, 7(4), 485-494.
YINGJIE ZHU, A. B., BENJAMIN PARDO, ROMAIN FOREY, NORBERT DOJER, RAZIYEH YOUSEFI, JULES BERLIN, NDE KENGNE, BERNARD FONGANG, ABHISHEK MITRA, JI LI, MAGDALENA SKRZYPCZAK, ANDRZEJ KUDLICKI, PHILIPPE PASERO, KRZYSZTOF GINALSKI, MAGA ROWICKA. Integrated analysis of patterns of DNA breaks reveals break formation mechanisms and their population distribution during replication stress. In *bioRxiv.* 2017.
YUAN, C., J. Y. GAO, J. C. GUO, L. BAI, et al. Dimethyl Sulfoxide Damages Mitochondrial Integrity and Membrane Potential in Cultured Astrocytes. Plos One, Sep 19 2014, 9(9).
ZALIS, S., M. B. DOLEV AND I. BRASLAVSKY 141 Inhibition of ice recrystallization by antifreeze proteins. Cryobiology, 2013/12/01/ 2013, 67(3), 438.
ZEMLIANSKYKH, N. G. AND L. A. BABIJCHUK The changes in erythrocyte Ca2+-ATPase activity induced by PEG-1500 and low temperatures. Cell and Tissue Biology, March 01 2017, 11(2), 104-110.
ZHAO, H., P. RYBAK, J. DOBRUCKI, F. TRAGANOS, et al. Relationship of DNA damage signaling to DNA replication following treatment with DNA topoisomerase inhibitors camptothecin/topotecan, mitoxantrone, or etoposide. Cytometry Part A, Jan 2012, 81A(1), 45-51.

7 List of Abbreviations

7-AAD	7-Aminoactinomycin D
AFM	Atomic Force Microscopy
AFP	Antifreeze protein in general, or the specific type ApAFP752 (depending on context)
BSSE	Basis Set Superposition Error
CM	Confocal Microscopy
DART-MS	Direct Analysis in Real Time Mass Spectrometry
DESI	Desorption Electrospray Ionization
DFT	Density Functional Theory
DI	Deionized
DMEM	Dulbecco‘s Modified Eagle‘s Medium
DMSO	Dimethyl Sulfoxide
DNA	Deoxyribonucleic Acid
DSB	Double-Strand Break
DSC	Differential Scanning Calorimetry
EDTA	Ethylenediaminetetraacetic Acid
FBS	Fetal Bovine Serum
FC	Flow Cytometry
FCS	Fetal Calf Serum
FDC	Force-Distance Curve
FITC	Fluorescein Isothiocyanate
FM	Force Map
FPLC	Fast Protein Liquid Chromatography
F/T	freezing/thawing
FWHM	Full Width at Half Maximum
HLTA	Hierarchical Latent Tree Analysis
IBP	Ice-Binding Protein
IDP	Intrinsically Disordered Protein
IPTG	Isopropanol-1-thio-β-D-galactopyranoside
IR/non-IR	Irradiated/nonirradiated
IRI	Ice Recrystallization Inhibition, resp. Inhibitor
ISP	Ice-Structuring Protein
LC/MS	Liquid Chromatography–Mass Spectrometry
MD	Molecular Dynamics
MEF	Mouse/Murine Embryonic Fibroblast
NHDF	Normal Human Dermal Fibroblast
PBS	Phosphate-Buffered Saline
PCM	Polarizable Continuum Model
PCNA	Proliferating Cell Nuclear Antigen
PDB	Protein Data Bank
PEG	Polyethylene Glycol
PI	Propidium Iodide
RESP	Restrained ElectroStatic Potential
SDS-PAGE	Sodium Dodecyl Sulfate Polyacrylamide Gel Electrophoresis
SP	Setpoint
SPC/E	Extended Simple Point Charge Model
SSC	Saline-Sodium Citrate
THP/F	Thermal Hysteresis Protein/Factor
XRD	X-Ray Diffraction
YM	Young's Modulus

8 List of Publications

1) **Golan, M.**, Přibyl, J., Pešl, M., Jelínková, Š., Acimovic, I., Jaroš, J., Rotrekl, V., Falk, M., Šefc, L., Skládal, P., Kratochvílová, I. (2018). Cryopreserved cells regeneration monitored by atomic force microscopy and correlated with state of cytoskeleton and nuclear membrane. [1]. *IEEE Transactions on Nanobioscience (accepted)*, 1-8.
2) Kratochvilova, I., **Golan, M.**, Pomeisl, K., Richter, J., Sedlakova, S., Sebera, J., Micova, J., Falk, M., Falkova, I., Reha, D., Elliott, K. W., Varga, K., Follett, S. E., Simek, D. (2017). Theoretical and experimental study of the antifreeze protein AFP752, trehalose and dimethyl sulfoxide cryoprotection mechanism: correlation with cryopreserved cell viability. *Rsc Advances, 7*(1), 352-360.
3) Kratochvílová, I., **Golan, M.,** Vala, M., Špérová, M., Weiter, M., Páv, O., Šebera, Jakub, Rosenberg, Ivan, Sychrovský, Vladimír, Tanaka, Yoshiyuki, Bickelhaupt, F. M. (2014). Theoretical and Experimental Study of Charge Transfer through DNA: Impact of Mercury Mediated T-Hg-T Base Pair. *The Journal of Physical Chemistry B, 118*(20), 5374-5381. doi: 10.1021/jp501986a
4) Kratochvílová, I., Šebera, J., Ashcheulov, P., **Golan, M.,** Ledvina, M., Míčová, J., Mravec, Filip, Kovalenko, Alexander, Zverev, Dmitry, Yavkin, Boris, Orlinskii, Sergei, Záliš, Stanislav, Fišerová, Anna, Richter, Jan, Šefc, Luděk, Turánek, J. (2014). Magnetical and Optical Properties of Nanodiamonds Can Be Tuned by Particles Surface Chemistry: Theoretical and Experimental Study. *The Journal of Physical Chemistry C, 118*(43), 25245-25252. doi: 10.1021/jp507581c
5) **Golan, M.**, Jelínková, Š., Kratochvílová, I., Skládal, P., Pešl, M., Rotrekl, V., & Přibyl, J. (2018). AFM monitoring the influence of selected cryoprotectants on regeneration of cryopreserved cells mechanical properties. *Frontiers in Physiology (submitted)*.
6) Falk, M., Falková, I., Pagáčová, E., Kopečná, O., Bačíková, A., Šimek, D., **Golan, M.**, Kozubek, S., Pekarová, M., Follett, S. E., Klejdus, B., Elliott, K. W., Varga, K., Teplá, O., Kratochvílová, I. (2018). Critical defects in cryopreserved cell nuclei: DNA structure changes. *Scientific Reports (submitted)*.

Other contributions

1) Jakub Skocdopole, Lucrezia Aversa, **Martin Golan**, Antonin Schenk,Giacomo Baldi, Irena Kratochvilova, Ladislav Kalvoda, Petr Nozar; PREPARING OF THE CHAMELEON COATING BY THE ION JET DEPOSITION METHOD; Acta Polytechnica, Czech Technical University in Prague 9 (2017) 19-25.(**paper**)

2) **Martin Golan**, Silvia Sedláková, Júlia Mičová, Jakub Šebera, Irena Kratochvílová, Jan Richter, David Řeha, Martin Falk, Iva Falková, Alena Bačíková, Eva Pagáčová, Krisztina Varga; Freezing processes in cryoprotective solutions of Me2SO, trehalose and antifreeze protein ApAFP752 and their impact on chromatin condition of cryopreserved cells
Cryobiology 71 (2015) 561-561. (**Conference Abstract in a Journal**)

3) M. Falk, I. Falková, E. Pagáčová, A. Bačíková, **M. Golan**, D. Šimek, S. Ignácová, J. Mičová, J. Šebera, J. Richter, D. Řeha, S. Follett, K. Elliott, K. Varga, I. Kratochvílová; Viability of cryopreserved cells, state of their nuclei, and properties of cryoprotectants ; Cryobiology 73 (2016) 423-423. (**Conference Abstract in a Journal**)

4) **Martin Golan**, Irena Kratochvílová, Martin Vala, Martin Weiter, Ondřej Páv, Jakub Šebera, Vladimír Sychrovský
JOINT THEORETICAL AND EXPERIMENTAL STUDY OF CHARGE TRANSFER THROUGH DNA: IMPACT OF MERCURY BINDING TO MISMATCHED BASE PAIRS
58th Annual Meeting of the Biophysical Society
(**Abstract in a Book of Conference Abstracts**)

5) Martin Falk, Iva Falková, Eva Pagáčová, Olga Kopečná, Alena Bačíková, Daniel Šimek, **Martin Golan**, Shelby E. Follett, Bořivoj Klejdus, K. Wade Elliott, Krisztina Varga, Olga Teplá, and Irena Kratochvílová; Critical defects in cryopreserved cell nuclei: DNA structure changes;Material Structure in Chemistry, Biology, Physics and Technology, Eds. Czech and Slovak Crystallographic Association, vol. 25, (March 2018) 5-6, ISBN: 1211. (**Abstract in a Book of Conference Abstracts**)